Expected astrometric properties of binaries in (E)DR3

prepared by: L. Lindegren
affiliation : Lund Observatory
approved by:
reference: GAIA-C3-TN-LU-LL-136-01
issue: 1
revision: 2
date: 2022-05-31
status: Issued

Abstract

This TN describes the expected astrometric properties of binaries in EDR3 and DR3 based on simple models of the distribution of binary parameters and how binaries are treated in IPD and AGIS. The results may be useful for understanding how different kinds of binaries show up in statistics such as the RUWE, and how they may behave in acceleration solutions. Possible criteria for selecting good 7p and 9p solutions are given.

Document History

Issue	Revision	Date	Author	Comment
1	2	2022-05-31	LL	Appendix E added (from LL-125)
1	1	2022-02-24	LL	Corrections in Sect. 4.4 and Table 3, removed links to non-public areas
1	0	2022-01-29	LL	Issued after incorporating comments from BAS
D	5	2021-08-11	LL	Appendix C and D added, revision of main text
D	4	2021-07-30	LL	More plots on 9p solutions, expanded conclusions
D	3	2021-07-29	LL	Sects. 6 added
D	2	2021-07-29	LL	Sects. 4.3, 4.4, and Appendix B added
D	1	2021-07-22	LL	Appendix A added
D	0	2021-07-05	LL	Created and first draft

Acronyms

The following table has been generated from the on-line Gaia acronym list:

Acronym	Description
AF	Astrometric Field (in Astro)
AGIS	Astrometric Global Iterative Solution
AL	ALong scan (direction)
CCD	Charge-Coupled Device
DR3	Gaia Data Release 3
EDR3	Early Gaia Data Release 3
FoV	Field of View (also denoted FOV)
HR	Hertzsprung-Russell (diagram)
IPD	Image Parameter Determination
LSF	Line Spread Function
MC	Mass Centre
NSL	Nominal Scanning Law
PC	PhotoCentre
PSF	Point Spread Function
RA	Right Ascension
RMS	Root-Mean-Square
RSE	Robust Scatter Estimator (measure of distribution width in AGIS)
RUWE	Re-normalised UWE
TN	Technical Note
UWE	Unit-Weight Error
VIM	Variability-Induced Mover (DMSA, Hipparcos Catalogue)

Contents

1 Introduction

This TN evolved from simulations performed for a talk at the AAS Division for Dynamical Astronomy Meeting in May 2021, illustrating the expected impact of binaries on the standard five-parameter astrometric solution.[1] The methodology for those and the present simulations is somewhat similar to the one used in Lindegren (LL-125), except that orbital motion is taken into account and that also acceleration (7p) and jerk (9p) solutions are considered.

2 Models

2.1 True astrometric parameters

For simplicity we consider only three different apparent magnitudes, namely $G \simeq 12.5$, 15.0, and 17.5. Around each magnitude, about one million sources were extracted from *Gaia* EDR3, using the queries

```
SELECT * FROM gaiaedr3.gaia_source
WHERE phot_g_mean_mag > 12.4 AND phot_g_mean_mag < 12.6

SELECT * FROM gaiaedr3.gaia_source
WHERE phot_g_mean_mag > 14.9 AND phot_g_mean_mag < 15.1
AND random_index < 329640000

SELECT * FROM gaiaedr3.gaia_source
WHERE phot_g_mean_mag > 17.4 AND phot_g_mean_mag < 17.6
AND random_index < 63000000
```

In the following various statistics for the three samples are given respectively without brackets, in round brackets, and in square brackets, as illustrated by the following example: the approximate magnitude in the sample is $G = 12.5$ ($G = 15.0$) [$G = 17.5$]. Only sources with positive parallaxes are used, and the true parallax was calculated as the posterior mean value for a uniform parallax prior,[2]

$$\varpi_{\rm true} = \begin{cases} \dfrac{\mathtt{normpdf}(\varpi/\sigma_\varpi)}{1-\mathtt{normcdf}(\varpi/\sigma_\varpi)} \times \sigma_\varpi & \text{if } \varpi/\sigma_\varpi < 5, \\ \varpi & \text{otherwise.} \end{cases} \tag{1}$$

[1] See `https://portal.research.lu.se/files/114432339/Lindegren_AAS_DOD_May2021.pdf`, and in particular slides 15 and 16 of the presentation.

[2] This method is not recommended for general use. It would have been better to use, for example, the more realistic distance estimates by Bailer-Jones et al. (2021). However, in practice this choice has very little impact on the results, because all effects of the binarity scale with the (true) parallax and are very small for most sources where the prior matters.

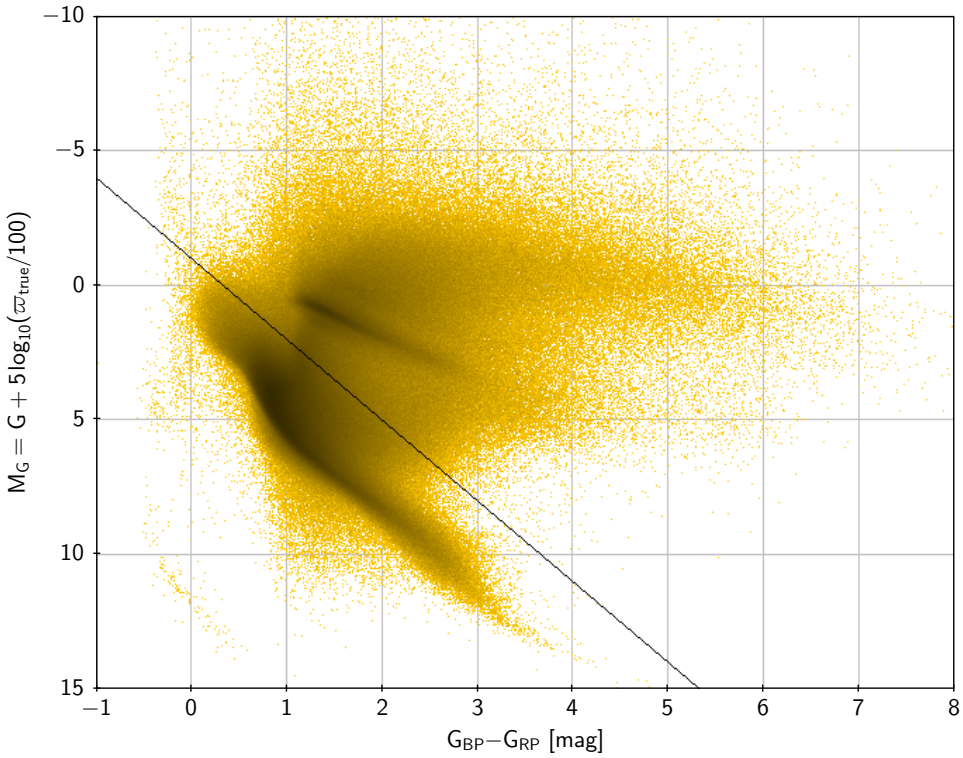

FIGURE 1: HR diagram constructed from the union of the three samples. The black line is the assumed separation between giants and non-giants.

Here, `normpdf` and `normcdf` are the probability density function and cumulative distribution function for the unit normal distribution $N(0,1)$.

For the other astrometric parameters (α, δ, $\mu_{\alpha*}$, μ_δ) the values in EDR3 are taken to be the true values. In fact, their precise values are irrelevant, as only the deviations from the assumed true values are analysed.

A substantial fraction of the sources are giants. The following criterion determines if a source is assumed to be a giant:

$$\varpi_{\rm true} < (100\ {\rm mas}) \times 10^{0.2[-1+3(G_{\rm BP}-G_{\rm RP})-G]} \tag{2}$$

In the HR diagram (Fig. 1) this corresponds to the black line separating the giants (above the line) from non-giants (below the line).

2.2 True binary parameters

For the subsequent analysis it is assumed that *all* sources in the three samples are binaries, or more precisely that they are the primary component in a binary system. This overestimates the number of binaries (and their overall effects on the astrometry) roughly by a factor two.

Based on Duquennoy & Mayor (1991), the true parameters of the binary are assumed to be

random variables with the following distributions:[3]

- The period P is lognormal,

$$\log_{10}(P/1 \text{ day}) \sim N(4.8, 2.3^2) \tag{3}$$

  (mean value 4.8, standard deviation 2.3). The median period is 172.75 yr.

- The eccentricity is

$$e = \begin{cases} 0 & \text{if } P \leq 11 \text{ days}, \\ N(0.31, 0.15^2) \text{ truncated to [0,1]} & \text{if } 11 < P \leq 1000 \text{ days}, \\ 0.95 \times \sqrt{U(0,1)} & \text{otherwise}, \end{cases} \tag{4}$$

  where $U(a,b)$ ($a < b$) is the uniform distribution in $[a,b]$. The square-root transformation for long periods gives a probability density $\propto e$, truncated at $e = 0.95$.

- The mass ratio $q = m_\mathrm{B}/m_\mathrm{A}$ is truncated lognormal,

$$q \sim N(0.23, 0.42^2) \text{ truncated to [0,1]} \tag{5}$$

- The spatial orientation of the orbit is isotropic,

$$\cos i \sim U(-1,1) \quad \text{(inclination)}, \tag{6}$$
$$\omega \sim U(0, 2\pi) \quad \text{(argument of periastron)}, \tag{7}$$
$$\Omega \sim U(0, 2\pi) \quad \text{(position angle of the node)}. \tag{8}$$

- The phase of the binary in its orbit is random, so the mean anomaly at the reference epoch is uniform,

$$M_0 \sim U(0, 2\pi) \tag{9}$$

The primary mass is taken to be one solar mass, $m_\mathrm{A} = 1\ M_\odot$. A more realistic assumption would have been possible, e.g. following Klüter et al. (2018), but in practice a constant value works just as well. The reason is that, on a logarithmic scale, the spread in stellar mass is much less than the spread in period, while the size of the orbit is only half as sensitive to the mass as it is to the period (see Eq. 10). The distribution of orbit sizes is therefore quite insensitive to the assumed primary mass distribution.

The semi-major axis a (in au) then follows from Kepler's third law,

$$a^3 = (m_\mathrm{A} + m_\mathrm{B})P^2\,. \tag{10}$$

Note that we always have $q \leq 1$, that is $m_\mathrm{B} \leq m_\mathrm{A}$.

[3]This classical study is now 30 years old, but the main distributions of relevance here (in P, e, q) have been essentially confirmed by later (post-HIPPARCOS) studies, such as Raghavan et al. (2010).

The flux ratio $f = I_B/I_A$ is assumed to be $f = q^4$, except when the primary is a giant, in which case $f = 0.01q^4$. The relatively rare cases where both components are giants are thus ignored. We also ignore the much more common cases where one of the components is a white dwarf. This will slightly underestimate the size of the photocentre orbits (by overestimating f), but only marginally so because f is usually small anyway.

Given the binary parameters and the time of observation, the angular offsets of the components (or photocentre) from the mass centre are computed using standard formulae (Appendix B).

Figure 2 shows the distributions of the simulated binaries in the $(P, \Delta G)$ plane, where P is the period and $\Delta G = -2.5 \log_{10} f$ the magnitude difference of the components. The distributions are essentially a combination of the log-normal distribution in P and a distribution in ΔG peaking at a few magnitudes and with a long exponential tail. The discontinuity at $\Delta G = 5$ mag comes from the binaries with a giant primary; it is less visible for the fainter binaries owing to the decreasing fraction of giants (Table 1). The distributions in Fig. 2 are used as background for various selections shown in subsequent diagrams (Figs. 14, 19, 20, 23–25).

2.3 Observation cadence and geometry

The reference scanning law for the time interval 2014.64032 (OBMT 1192 rev) to 2017.40415 (OBMT 5230 rev) was used to generate the time of transits and scan geometry (position angle and AL parallax factor). This time interval is the same as was used for the AGIS 3.2 solution, which was the basis for the EDR3 astrometry. Observations falling in any of the gaps listed in Table 1 of Lindegren et al. (2021) were not used. Additionally, in order to reproduce the actual number of astrometric observations in EDR3 (cf. Table 1), a random fraction of 6.2% of the observations were discarded.

To save time, the sequence of the times and geometry of the scans was precomputed for a set of 3072 points uniformly distributed on the celestial sphere (at healpix level 4), and the point closest to each source was used. Individual CCD observations in the AF were simulated, that is (normally) nine observations per FoV transit. The same time and geometry was used for all nine CCD observations in a transit. Thus, the observation bias produced by the binarity was constant in each FoV transit, but the random noise was different and independent.

The random noise per CCD observation was assumed to be Gaussian with standard deviation

$$\sigma_\eta = \max\left(0.135,\ \sqrt{0.085^2 + 0.055x + 0.0017x^2}\right) \text{ mas}, \tag{11}$$

where $x = 10^{0.4(G-15)}$. In Fig. 3 this function is plotted together with the formal uncertainties from the IPD and the RSE of the residuals in the primary AGIS 3.2 solution. Equation (11) is a good fit to the RSE for $G \gtrsim 13$ but could be an underestimation for brighter sources.

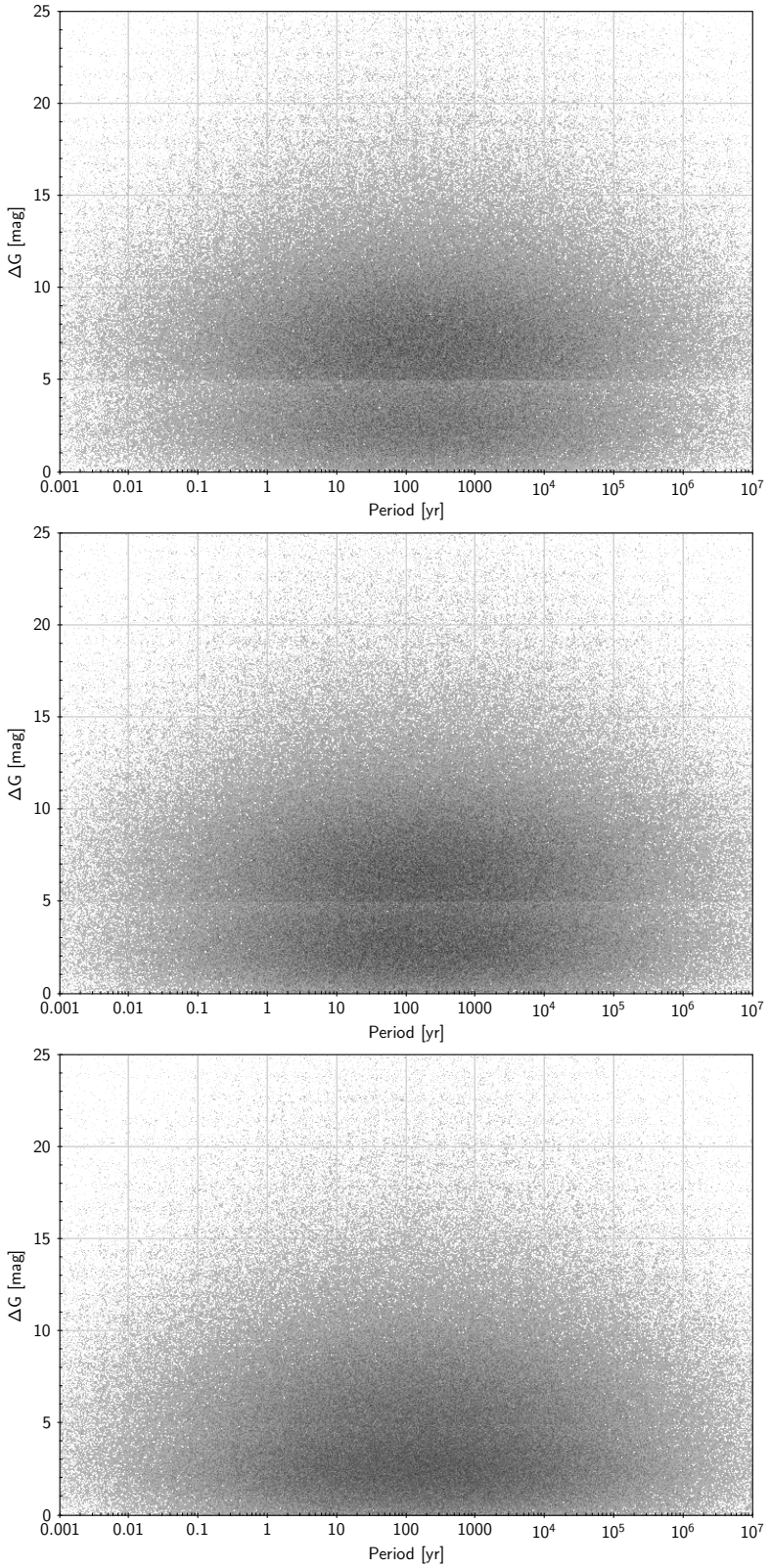

FIGURE 2: Distribution in the $(P, \Delta G)$ plane of the simulated binaries. The panels are for $G = 12.5$ (top), 15.0 (middle), and 17.5 (bottom).

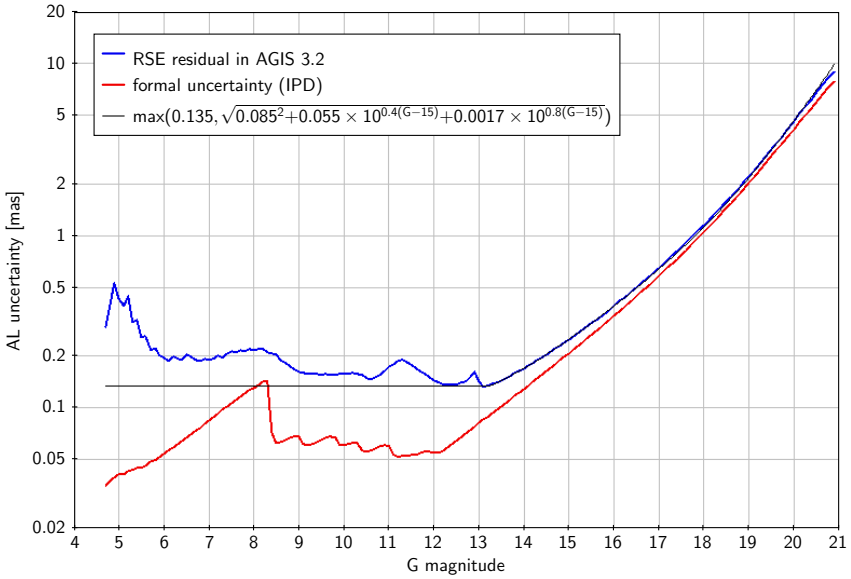

FIGURE 3: Uncertainty of AL observations per CCD. The black curve is the assumed relation in Eq. (11).

2.4 Observation bias from binarity

Let ϱ and θ be the angular separation and position angle of a binary at the time of observation. Furthermore, let q and f be the mass ratio and flux ratio of the binary (both in the range [0,1]) and ψ the position angle of the scan. The AL observation bias $\delta\eta$ is the expected difference between the actually measured AL position (as obtained in IPD) and the AL position of the mass centre of the binary. This bias is primarily a function of the projected AL separation $\Delta\eta = \varrho\cos(\psi-\theta)$, the flux ratio f (or magnitude difference $\Delta G = -2.5\log_{10} f$), and the mass ratio q. The bias calculation is based on the simple model introduced in Appendix A of Lindegren (LL-125), here for convenience reproduced as Appendix E. It distinguishes three regimes depending on the projected separation relative to the 'resolution unit' of the instrument, $u = 90$ mas:

$$\delta\eta = \begin{cases} \left(\dfrac{f}{1+f} - \dfrac{q}{1+q}\right)\Delta\eta & \text{if } |\Delta\eta/u| \le 0.1, \\ uB(f,\Delta\eta/u) - \dfrac{q}{1+q}\,\Delta\eta & \text{if } 0.1 < |\Delta\eta/u| \le 3-f, \\ -\dfrac{q}{1+q}\,\Delta\eta & \text{if } 3-f < |\Delta\eta/u|. \end{cases} \tag{12}$$

Here $B(f,p)$ is the dimensionless bias function defined in Appendix E (cf. Fig. 4).

In Eq. (12) the first case corresponds to astrometric binaries that are accurately observed by their photocentre; the second case are partially resolved system, for which the observed position is no longer exactly the photocentre but displaced towards the primary;[4] the third case corresponds to binaries that are sufficiently resolved AL that the IPD essentially gives the position of the

[4]The first case is the limiting form of the second case when $|\Delta\eta/u| \to 0$, but is better for numerical accuracy.

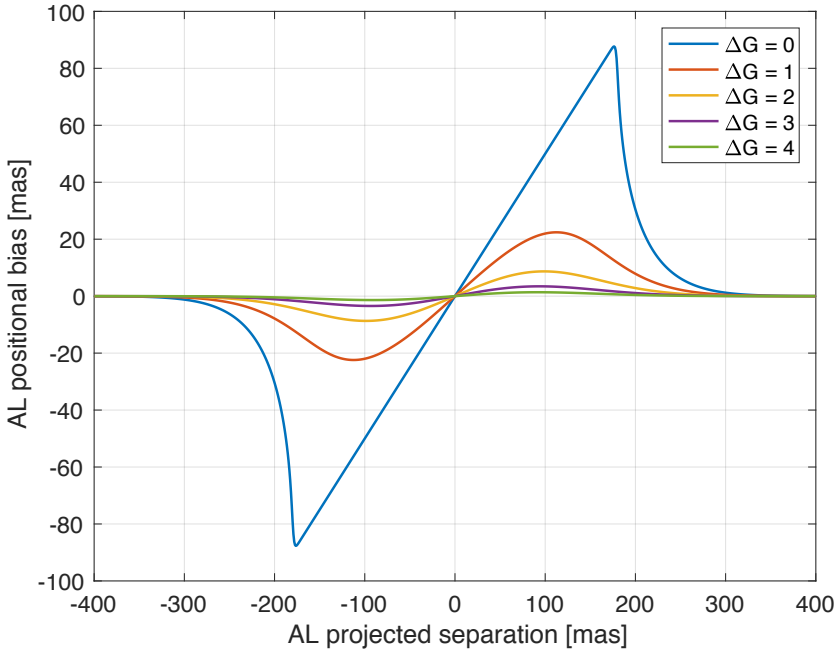

FIGURE 4: The scaled bias function $uB(f, \Delta\eta/u)$ used in the simulations, shown as a function of $\Delta\eta$ and ΔG. $u = 90$ mas is the standard width of the Gaussian LSF and $f = 10^{-0.4\Delta G}$ is the flux ratio. See Appendix E for details.

primary. The limit $3 - f$ is very approximate and depends on implementation details of the IPD. It means that an equal-magnitude binary is resolved if the projected separation exceeds 180 mas or 3 AL pixels.

Additional quantification of resolution issues are given in Appendix D.

2.5 Observation equations

For each binary in the simulated samples, six different solutions were made, namely five-, seven-, and nine-parameters solutions with and without observational noise. For brevity the noisy solutions are referred to as 5p, 7p, and 9p, and the noiseless as 5p0, 7p0, and 9p0. We use the variable $p = 5, 7, 9$ to designate the number of (active) parameters in the solution.

The observation equations for the noiseless solutions 5p0, 7p0, and 9p0 are of the form

$$\Delta\alpha_* \sin\psi + \Delta\delta\cos\psi + \Delta\varpi P_{\rm AL} + \Delta\mu_{\alpha*}\tau\sin\psi + \Delta\mu_\delta\tau\cos\psi + \dot{\mu}_{\alpha*}\frac{\tau^2}{2}\sin\psi + \dot{\mu}_\delta\frac{\tau^2}{2}\cos\psi + \ddot{\mu}_{\alpha*}\frac{\tau^3}{6}\sin\psi + \ddot{\mu}_\delta\frac{\tau^3}{6}\cos\psi = \delta\eta\,, \quad (13)$$

where $\tau = t - t_{\rm ref}$ (t is the time of observation in years and $t_{\rm ref} = 2016.0$), ψ is the scan angle, $P_{\rm AL}$ the AL parallax factor, and $\delta\eta$ the AL bias according to Eq. (12). Depending on the type of

solution, only the first p terms are included. The system of n equations, where n is the number of CCD observations, is solved by unweighted least-squares, without removal of outliers. The resulting values of $\Delta\alpha_*$, $\Delta\delta$, $\Delta\varpi$, $\Delta\mu_{\alpha*}$, and $\Delta\mu_\delta$ are the expected biases in the five astrometric parameters, due to the binarity, while $\dot{\mu}_{\alpha*}$ and $\dot{\mu}_\delta$ are the best-fitting acceleration terms. Other important statistics from these solutions are the RMS residuals of the fits, which we denote RMS_p. They are expressed as angles (in μas) and can be interpreted as the RMS modelling errors of the 5p, 7p, or 9p solution with respect to the (true) binary model. For a single star, or a very tight binary, they are all essentially zero. For a long-period astrometric binary we expect $\mathrm{RMS}_5 > 0$ and $\mathrm{RMS}_p \simeq 0$ for $p = 7$ or p.

For the noisy solutions the observation equations are of the form

$$\Delta\alpha_* \sin\psi + \Delta\delta\cos\psi + \Delta\varpi P_{\mathrm{AL}} + \Delta\mu_{\alpha*}\tau\sin\psi + \Delta\mu_\delta\tau\cos\psi + \dot{\mu}_{\alpha*}\frac{\tau^2}{2}\sin\psi + \dot{\mu}_\delta\frac{\tau^2}{2}\cos\psi + \ddot{\mu}_{\alpha*}\frac{\tau^3}{6}\sin\psi + \ddot{\mu}_\delta\frac{\tau^3}{6}\cos\psi = \delta\eta + \nu\,, \quad (14)$$

where $\nu \sim N(0, \sigma_\eta^2)$ is the Gaussian noise per CCD observation of standard deviation σ_η according to Eq. (11). The n observation equations are solved by weighted least-squares, without removal of outliers. The weight of each equation is set to σ_η^{-2}. Important statistics for these solutions are the chi-squares, denoted $\chi^2_{5\mathrm{p}}$, $\chi^2_{7\mathrm{p}}$, and $\chi^2_{9\mathrm{p}}$, and the unit weight errors

$$\mathrm{UWE}_5 = \sqrt{\frac{\chi^2_{5\mathrm{p}}}{n-5}}\,, \quad \mathrm{UWE}_7 = \sqrt{\frac{\chi^2_{7\mathrm{p}}}{n-7}}\,, \quad \mathrm{UWE}_9 = \sqrt{\frac{\chi^2_{9\mathrm{p}}}{n-9}}\,. \quad (15)$$

UWE_5 is the statistic closest corresponding to the RUWE in EDR3. For the noisy solutions, formal uncertainties of the astrometric updates are also computed from the inverse of the weighted normal matrix, without any additional scaling based on the UWE. The formal uncertainties are slightly different depending on p owing to the correlations between the acceleration/jerk parameters and the other astrometric parameters, in particular α and δ.

Table 1 gives some key statistics of the simulated binary samples in comparison with EDR3 (see Sect. 2.6 for further discussion). Table 2 lists all the quantities saved for each binary. The rest of this TN is a statistical analysis based on these quantities and comparison data from EDR3.

TABLE 1: Statistics of some key properties of the simulated samples in this study. Values in brackets are the corresponding statistics in EDR3.

Quantity	$G \simeq 12.5$	$G \simeq 15.0$	$G \simeq 17.5$
Number of binaries	827 743	1 003 939	928 672
Fraction with a giant as primary	0.43	0.32	0.15
Mean number of transits	42.5 (43.9)	42.0 (43.4)	42.1 (42.7)
Mean number of CCD observations in AF	382 (378)	378 (376)	379 (375)
Mean UWE_5 (RUWE)	2.66 (1.62)	1.81 (1.27)	1.21 (1.09)
Median $\sigma_{\alpha*}$ [μas]	11.3 (11.5)	21.9 (21.9)	74.1 (74.9)
Median σ_{δ} [μas]	10.6 (10.3)	20.1 (19.1)	67.8 (66.2)
Median σ_{ϖ} [μas]	15.4 (14.3)	29.3 (27.5)	98.6 (94.8)
Median $\sigma_{\mu\alpha*}$ [μas yr^{-1}]	15.0 (14.8)	28.8 (28.3)	97.6 (97.9)
Median $\sigma_{\mu\delta}$ [μas yr^{-1}]	13.6 (13.0)	25.5 (24.5)	86.1 (85.2)

TABLE 2: Quantities calculated for the simulated binaries.

Name	Description [unit]
sourceId	source identifier in EDR3
G	magnitude
isGiant	1 for giant otherwise 0
ra	RA [deg]
dec	Dec [deg]
dir	index of position used for scanning
nTr	number of FoV transits
nObs	number of CCD observations
plx	true parallax [mas]
pmra	proper motion in RA [mas/yr]
pmdec	proper motion in Dec [mas/yr]
mA	mass of primary [Msun]
mB	mass of secondary [Msun]
P	period [yr]
aAu	semi-major axis [au]
aMas	semi-major axis [mas] = aAu*plx
e	eccentricity
incl	inclination [rad]
om	ω [rad]
Omega	Ω [rad]
M0	mean anomaly at 2016.0
f	flux ratio
dMag0	magnitude difference ΔG
daSep0	angular separation in RA [mas]
ddSep0	angular separation in Dec [mas]
dPmaPc0	proper motion in RA of PC wrt MC at 2016.0 [mas/yr]
dPmdPc0	proper motion in Dec of PC wrt MC at 2016.0 [mas/yr]
accaPc0	acceleration in RA of PC wrt MC at 2016.0 [mas/yr2]
accdPc0	acceleration in Dec of PC wrt MC at 2016.0 [mas/yr2]
jrkaPc0	jerk in RA of PC wrt MC at 2016.0 [mas/yr3]
jrkdPc0	jerk in Dec of PC wrt MC at 2016.0 [mas/yr3]
accaPr0	acceleration in RA of primary wrt MC at 2016.0 [mas/yr2]
accdPr0	acceleration in Dec of primary wrt MC at 2016.0 [mas/yr2]
jrkaPr0	jerk in RA of primary wrt MC at 2016.0 [mas/yr3]
jrkdPr0	jerk in Dec of primary wrt MC at 2016.0 [mas/yr3]
M2min0	$m^0_{\rm B,min}$ [Msun]
fracDp	fraction of transits with double peak detection
u0	mean location $\hat{\gamma}$ [–]
uRms	location dispersion σ_O [mas]
stdCcd	observation noise per CCD [mas]
rmsRes_5	RMS_5 [mas]
dA_5	5p0 bias in RA at 2016.0 [mas]
dD_5	5p0 bias in Dec at 2016.0 [mas]
dPlx_5	5p0 bias in parallax [mas]
dPma_5	5p0 bias in pmra [mas/yr]
dPmd_5	5p0 bias in pmdec [mas/yr]
eA_5	5p0 improvement factor in RA
eD_5	5p0 improvement factor in Dec
ePlx_5	5p0 improvement factor in parallax
ePma_5	5p0 improvement factor in pmra
ePmd_5	5p0 improvement factor in pmdec
rmsResN_5	UWE_5
dAN_5	5p bias in RA at 2016.0 [mas]
dDN_5	5p bias in Dec at 2016.0 [mas]
dPlxN_5	5p biasn in parallax [mas]
dPmaN_5	5p bias in pmra [mas/yr]
dPmdN_5	5p bias in pmdec [mas/yr]
eAN_5	5p uncertainty in RA [mas]
eDN_5	5p uncertainty in Dec [mas]
ePlxN_5	5p uncertainty in parallax [mas]
ePmaN_5	5p uncertainty in pmra [mas/yr]
ePmdN_5	5p uncertainty in pmdec [mas/yr]
chi2_5	$\chi^2_{5\mathrm{p}}$
rmsRes_7	RMS_7
dA_7	7p0 bias in RA at 2016.0 [mas]
dD_7	7p0 bias in Dec at 2016.0 [mas]
dPlx_7	7p0 bias in parallax [mas]
dPma_7	7p0 bias in pmra [mas/yr]
dPmd_7	7p0 bias in pmdec [mas/yr]
accA_7	7p0 acceleration in RA [mas/yr2]
accD_7	7p0 acceleration in Dec [mas/yr2]
eA_7	7p0 improvement factor in RA
eD_7	7p0 improvement factor in Dec
ePlx_7	7p0 improvement factor in parallax
ePma_7	7p0 improvement factor in pmra

Name	Description [unit]
ePmd_7	7p0 improvement factor in pmdec
eaccA_7	7p0 improvement factor in acc. in RA
eaccD_7	7p0 improvement factor in acc. in Dec
rhoAccAD_7	7p0 correlation coeff. between acc. in RA and Dec
muDot	7p0 total acceleration [mas/yr2]
sigmaMuDot	7p0 uncertainty of total acceleration [mas/yr2]
M2min	7p0 $m_{\rm B,min}$ using noiseless data [Msun]
rmsResN_7	UWE_7
dAN_7	7p bias in RA at 2016.0 [mas]
dDN_7	7p bias in Dec at 2016.0 [mas]
dPlxN_7	7p bias in parallax [mas]
dPmaN_7	7p bias in pmra [mas/yr]
dPmdN_7	7p bias in pmdec [mas/yr]
accAN_7	7p acceleration in RA [mas/yr2]
accDN_7	7p acceleration in Dec [mas/yr2]
eAN_7	7p uncertainty in RA
eDN_7	7p uncertainty in Dec
ePlxN_7	7p uncertainty in parallax
ePmaN_7	7p uncertainty in pmra
ePmdN_7	7p uncertaintyin pmdec
eaccAN_7	7p uncertainty in acc. in RA
eaccDN_7	7p uncertainty in acc. in Dec
rhoAccADN_7	7p correlation coeff. between acc. in RA and Dec
muDotN	7p total acceleration [mas/yr2]
sigmaMuDotN	7p uncertainty of total acceleration [mas/yr2]
M2minN	7p $m_{\rm B,min}$ using noisy data [Msun]
F75	F_{75}
chi2_7	$\chi^2_{7\mathrm{p}}$
rmsRes_9	RMS_9
dA_9	9p0 bias in RA at 2016.0 [mas]
dD_9	9p0 bias in Dec at 2016.0 [mas]
dPlx_9	9p0 bias in parallax [mas]
dPma_9	9p0 bias in pmra [mas/yr]
dPmd_9	9p0 bias in pmdec [mas/yr]
accA_9	9p0 acceleration in RA [mas/yr2]
accD_9	9p0 acceleration in Dec [mas/yr2]
jrkA_9	9p0 jerk in RA [mas/yr3]
jrkD_9	9p0 jerk in Dec [mas/yr3]
eA_9	9p0 improvement factor in RA
eD_9	9p0 improvement factor in Dec
ePlx_9	9p0 improvement factor in parallax
ePma_9	9p0 improvement factor in pmra
ePmd_9	9p0 improvement factor in pmdec
eaccA_9	9p0 improvement factor in acc. in RA
eaccD_9	9p0 improvement factor in acc. in Dec
ejrkA_9	9p0 improvement factor in jerk in RA
ejrkD_9	9p0 improvement factor in jerk in Dec
rhoJrkAD	9p0 correlation coeff. between jerk in RA and Dec
muDotDot	9p0 total jerk [mas/yr3]
sigmaMuDotDot	9p0 uncertainty of total jerk [mas/yr3]
rmsResN_9	UWE_9
dAN_9	9p bias in RA at 2016.0 [mas]
dDN_9	9p bias in Dec at 2016.0 [mas]
dPlxN_9	9p bias in parallax [mas]
dPmaN_9	9p bias in pmra [mas/yr]
dPmdN_9	9p bias in pmdec [mas/yr]
accAN_9	9p acceleration in RA [mas/yr2]
accDN_9	9p acceleration in Dec [mas/yr2]
jrkAN_9	9p jerk in RA [mas/yr3]
jrkDN_9	9p jerk in Dec [mas/yr3]
eAN_9	9p uncertainty in RA
eDN_9	9p uncertainty in Dec
ePlxN_9	9p uncertainty in parallax
ePmaN_9	9p uncertainty in pmra
ePmdN_9	9p uncertaintyin pmdec
eaccAN_9	9p uncertainty in acc. in RA
eaccDN_9	9p uncertainty in acc. in Dec
ejrkAN_9	9p uncertainty in jerk in RA
ejrkDN_9	9p uncertainty in jerk in Dec
rhoJrkADN_9	9p correlation coeff. between jerk in RA and Dec
muDotDotN	9p total jerk [mas/yr3]
sigmaMuDotDotN	9p uncertainty of total jerk [mas/yr3]
F97	F_{97}
F95	F_{95}
chi2_9	$\chi^2_{9\mathrm{p}}$

2.6 Model comparison with EDR3

The model described above should be able to reproduce some basic statistics in *Gaia* EDR3, in particular those that do not depend on the binary model. As shown in Table 1 the mean number of transits and CCD observations are well reproduced, as they should be, given that the random fraction of lost observations (Sect. 2.3) was adjusted to obtain agreement in the mean number of observations. Also the median formal uncertainties of all five astrometric parameters are well reproduced at all magnitudes, suggesting that Eq. (11) is a good approximation. The mean formal uncertainties are however severely underestimated by the simulations, especially for the bright stars. This is caused by the tail of low-precision solutions that are present in EDR3, but not in the simulations (Fig. 5). These low-precision solutions in EDR3 typically have high RUWE (rather than few observations), so the higher formal uncertainties in EDR3 is due to the excess source noise being included in the error calculation, effectively inflating the uncertainties roughly by a factor equal to the RUWE. Indeed, if the formal uncertainties in the simulations are inflated by the factor UWE_5, their distributions become more similar to EDR3 (Fig. 6) and even more conservative, partly because the simulations include too many binaries (see below).

Another statistic in Table 1 not well reproduced by the simulations is the RUWE in EDR3 in comparison with the simulated UWE_5: the mean UWE_5 is significantly higher than the mean RUWE. Partly this is explained by our assumption that all sources in the samples are primaries in binary systems, whereas in reality this is only the case for about half the sources. However, the distributions of RUWE and UWE_5 are also markedly different (Fig. 7). The simulations have an excess of large values of UWE_5 and too few moderate values (between 1.3 and 2). This could indicate a serious deficiency of the model. (It is also possible that the distribution of RUWE in EDR3 is wider than expected because of unmodelled calibration errors and/or problems with the renormalisation process for the RUWE.) Pending further refinements this model should nevertheless be useful to obtain realistic order-of-magnitude estimates of various binary statistics relevant for the astrometric performance of the 5p and 7p solutions in EDR3. When interpreting the absolute frequencies of different kinds of binaries it should be remembered that the simulations probably overestimate their numbers by a factor of about two.

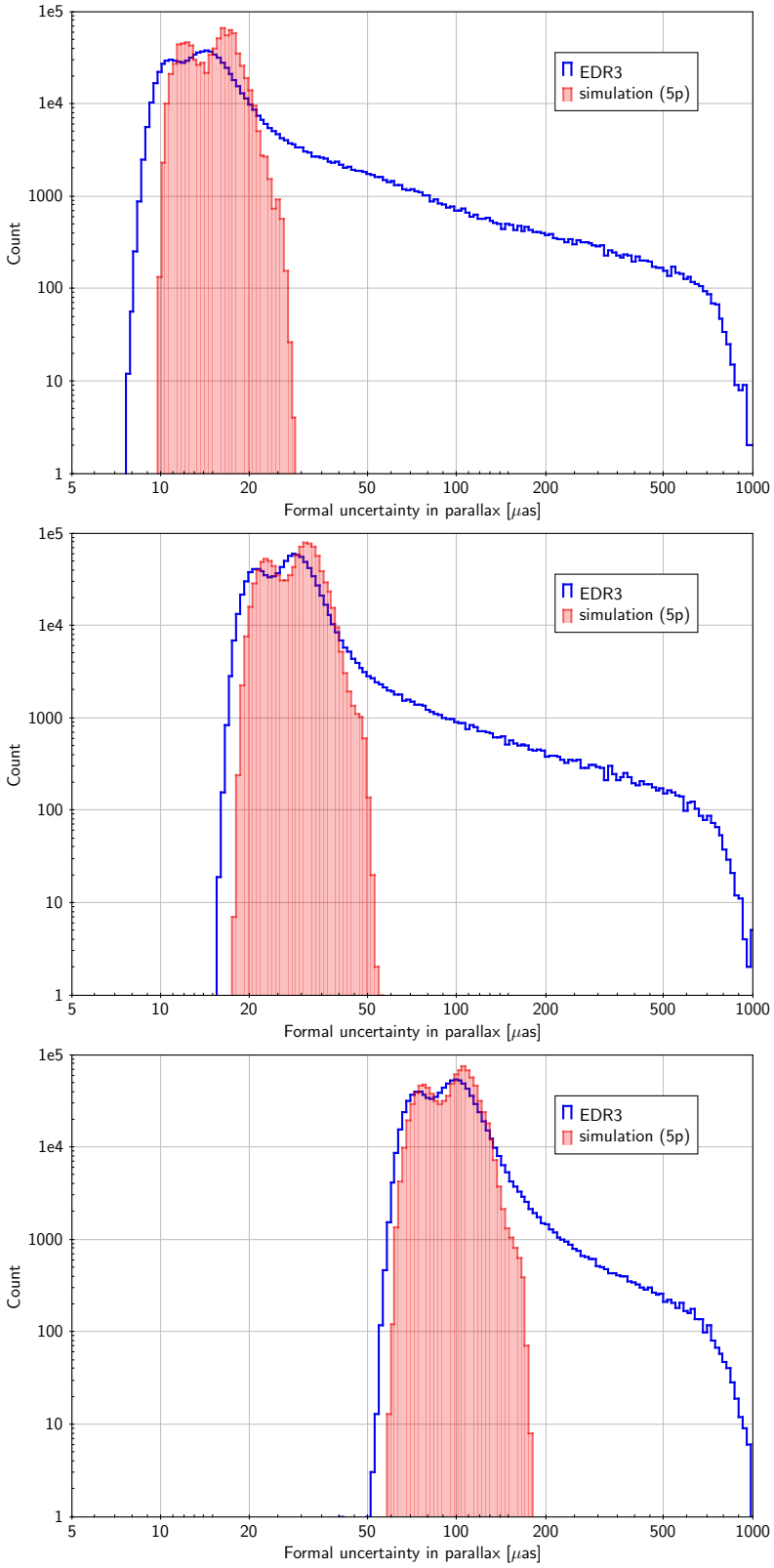

FIGURE 5: Distribution of formal parallax uncertainty in EDR3 (blue) and 5p simulation (red) for $G = 12.5$ (top), 15.0 (middle), and 17.5 (bottom).

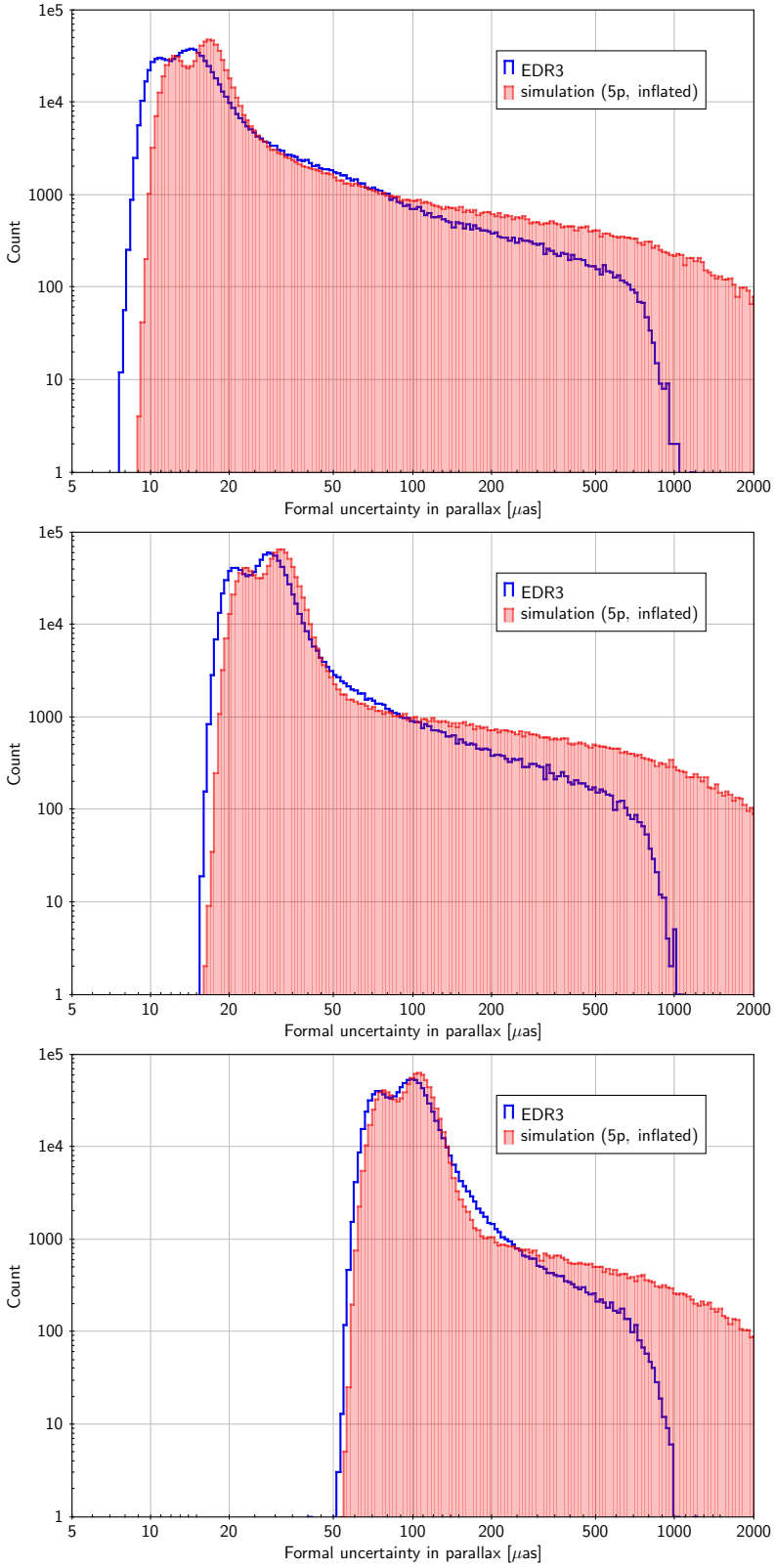

FIGURE 6: Distribution of formal parallax uncertainty in EDR3 (blue) and 5p simulation (red), inflated by UWE_5, for $G = 12.5$ (top), 15.0 (middle), and 17.5 (bottom).

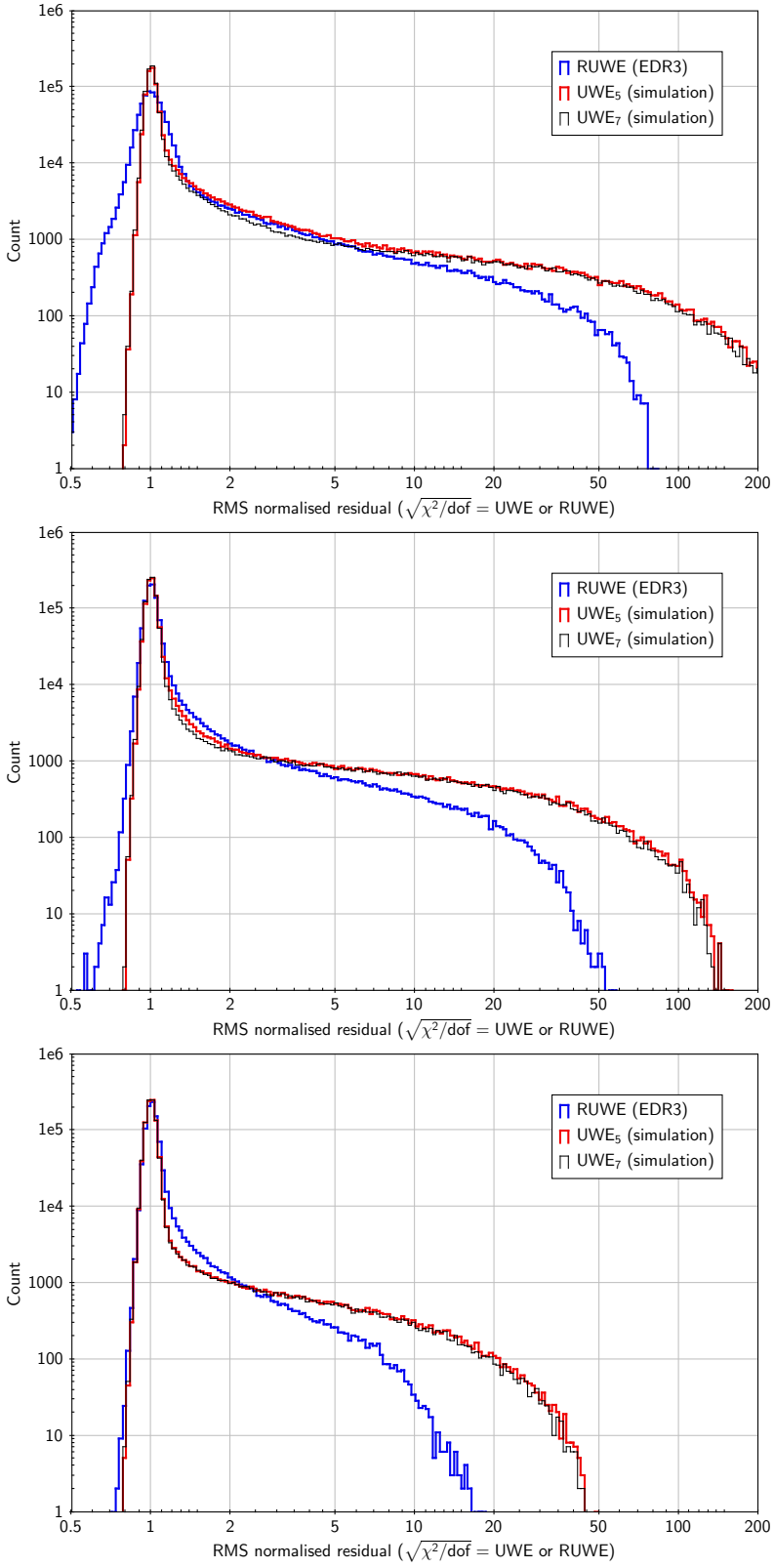

FIGURE 7: Distribution of RUWE in EDR3 (blue) and the simulated UWE_5 (red) and UWE_7 (thin black) for $G = 12.5$ (top), 15.0 (middle), and 17.5 (bottom).

3 Expected effects of binarity in five-parameter solutions

3.1 Noise-free data (5p0)

Figure 8 shows RMS_5, the modelling error (noisefree RMS residual) when the five-parameter model is fitted to the observations, versus P. The main features in the plots can easily be understood:

- For very short periods ($P \lesssim 0.01$ yr) the modelling error is generally negligible (few μas) because the orbits are tight so the photocentric wobble is small.
- The typical modelling error reaches a peak when the period is about equal to the length of the observations, about 2.75 yr. For such periods the photocentre wobble has its maximum size while none of it can yet be absorbed by the astrometric model. The exception is that parallax could absorb some of the wobble if the period is close to 1 yr, which gives a (very small) depression in the mean modelling error at $P \simeq 1$ yr.
- For $P > 2.75$ yr part of the orbital wobble can be absorbed by the proper motion components in the five-parameter model, which causes the declining trend with increasing P up to several decades.
- For $P \gtrsim 100$ yr the plots become more complex. Most of the points continue the declining trend, but a smaller fraction of them form a cloud with much higher modelling errors. At least for $G = 12.5$ there seem to be two such clouds. These features are more readily understood with aid of Figure 9, which are coloured not according to the density of points at each position in the diagram, but according to the binary separation of the sky, the magnitude difference, and the fraction of giants in the simulated sample. (These plots are only shown for $G = 15$, but the interpretation is very similar for the other two samples.) The typical angular separation in the clouds is about 30 to 1000 mas, which means that they are in the non-linear regime of the bias function B where the photocentre is not always a good approximation (depending on the scan angle). The middle panel in Fig. 9 shows that the modelling error is a strong function of the magnitude difference, and the bottom panel shows that the two clouds are actually produced by the main-sequence/giant dichotomy.
- For orbital periods longer than 10^4 to 10^5 yr the components are sufficiently well separated on the sky ($\gtrsim 1$ arcsec) that the observations of the primary are usually undisturbed and the curvature of its orbital motion over the observation interval is so small that it does not produce any significant modelling error. As a consequence, the declining trend with P continues for most of the binaries. The two parallel sequences visible in all the diagrams for $P \gtrsim 1000$ yr correspond to the main-sequence and giant primaries.

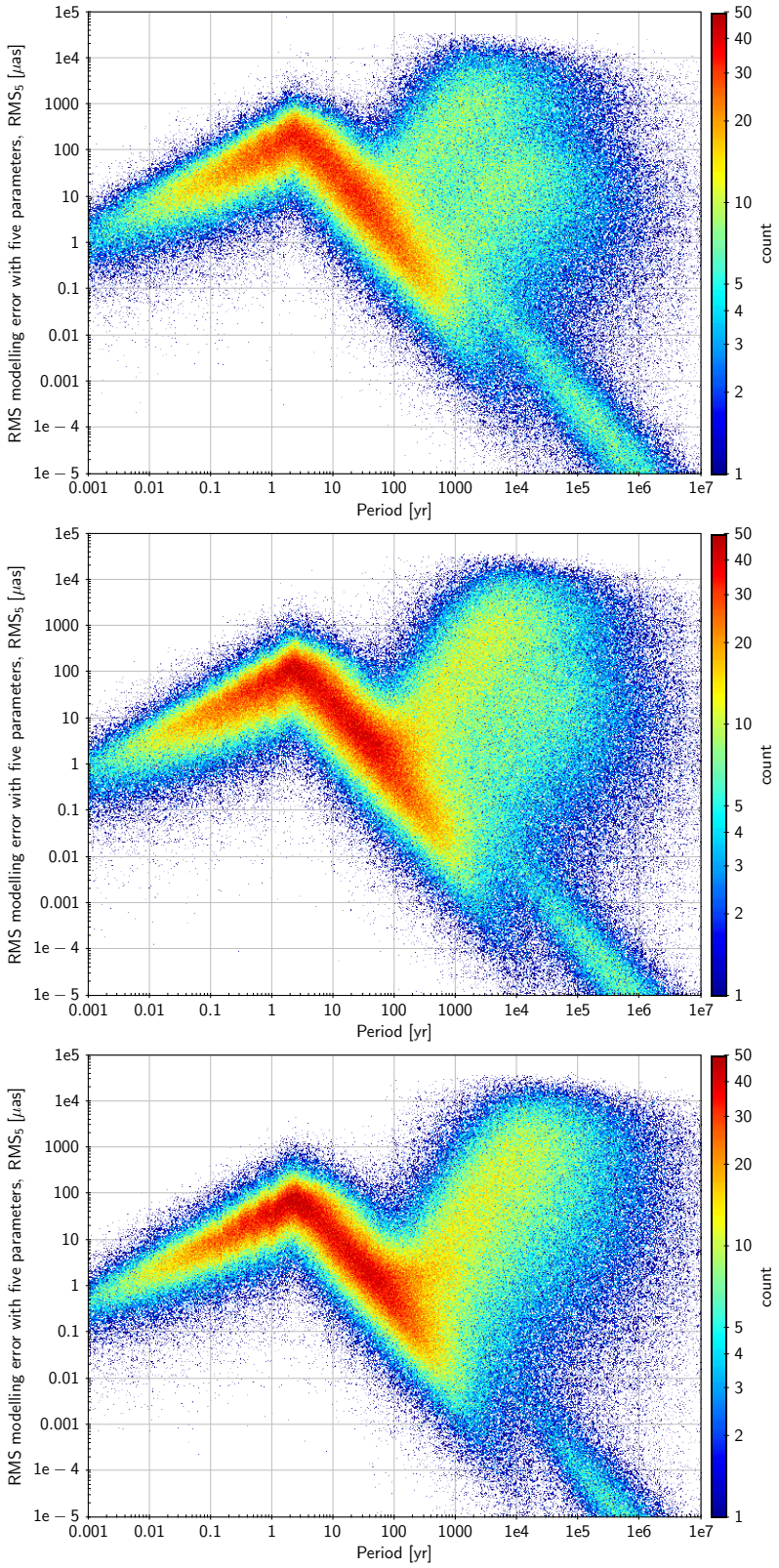

FIGURE 8: Modelling error in the noisefree five-parameter solutions (5p0) versus orbital period for $G = 12.5$ (top), 15.0 (middle), and 17.5 (bottom).

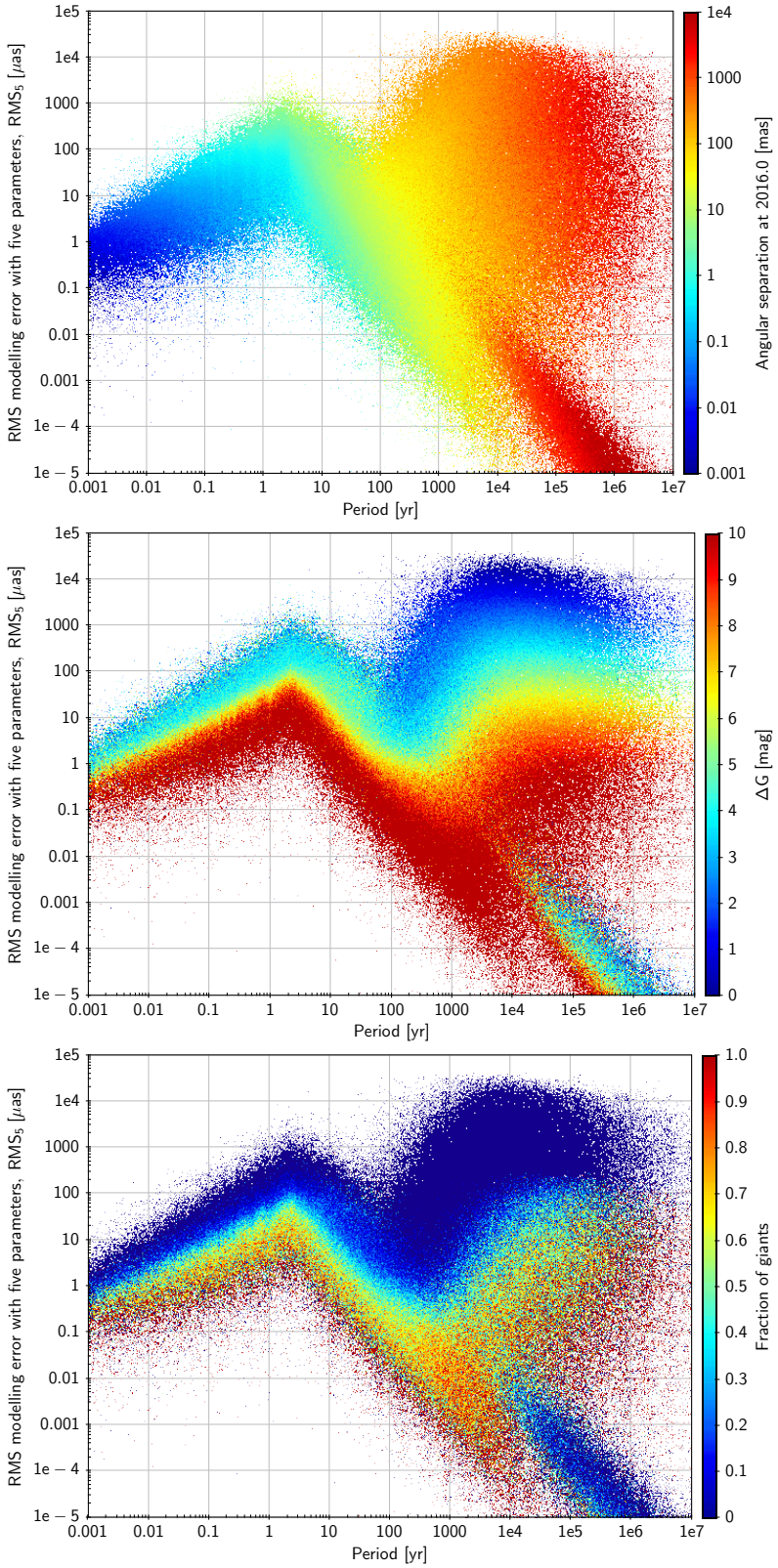

FIGURE 9: Modelling error in the noisefree five-parameter solutions (5p0) versus orbital period for $G = 15.0$. The plots are colour coded by the mean angular separation (top), the mean magnitude difference (middle), and the fraction of giants (bottom) at each point in the diagram.

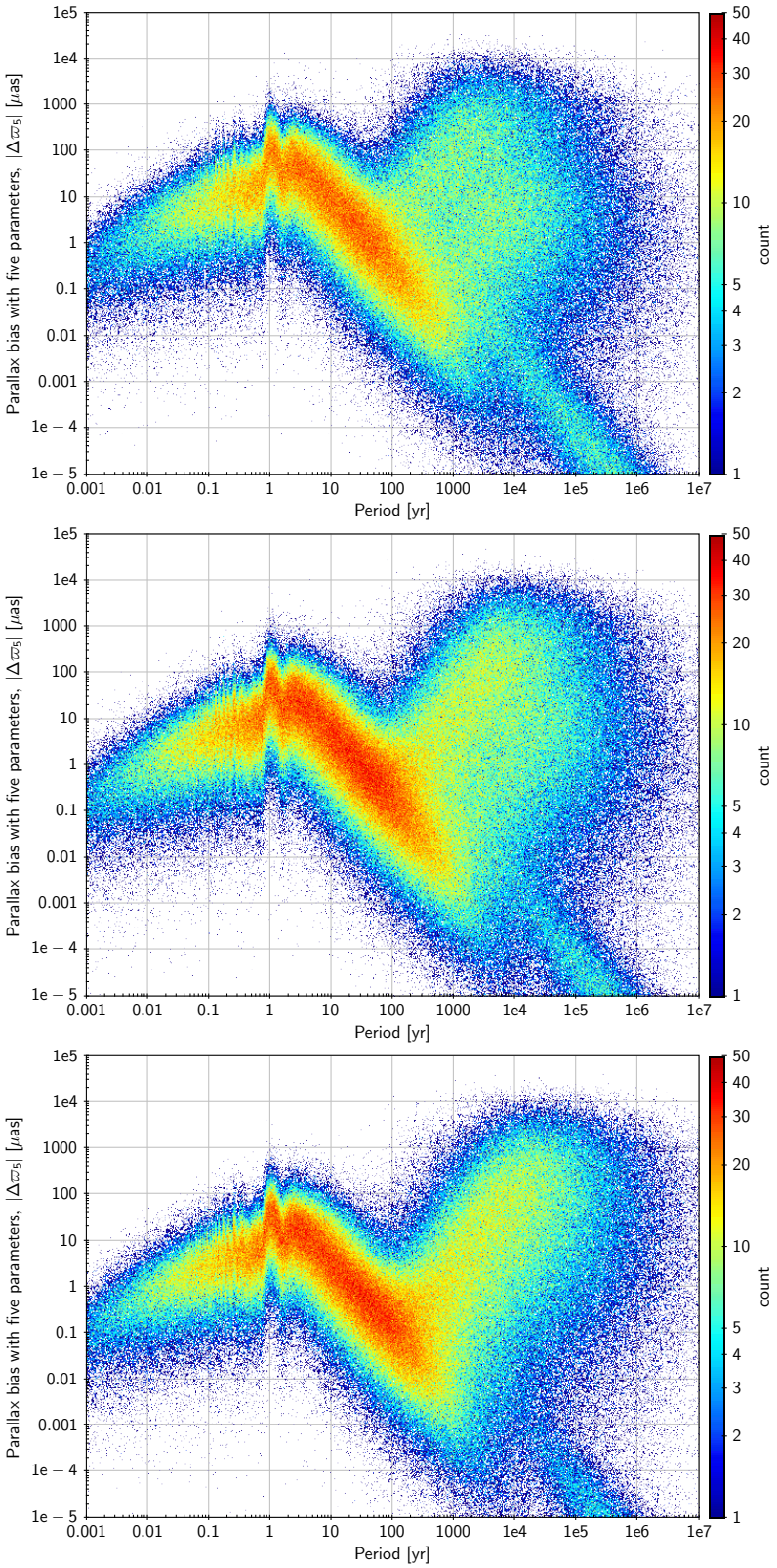

FIGURE 10: Absolute value of the parallax bias versus orbital period for $G = 12.5$ (top), 15.0 (middle), and 17.5 (bottom).

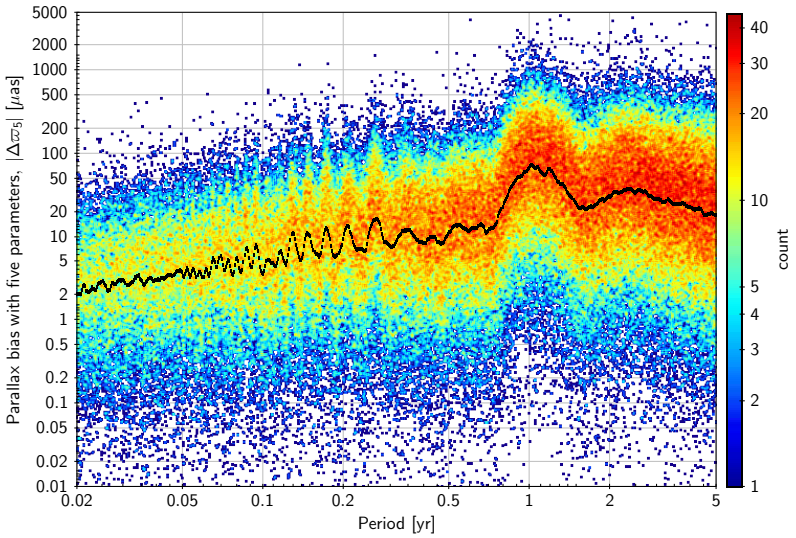

FIGURE 11: Absolute value of the parallax bias versus orbital period for $G = 12.5$. The black curve is the median absolute bias versus period.

Figure 10 shows the bias in parallax caused by the orbital solution when the five-parameter model is fitted. On the whole, these plots are very similar to the RMS modelling errors: the median parallax bias is about 20% of the RMS modelling error. Around $P \sim 1$ yr there are a number of features produced by the parallax solution absorbing part of the modelling error; a zoom-in on the relevant period interval is shown in Fig. 11. As estimated from this plot, the main peaks appear to be centred on the frequencies $1/P \simeq 0.43$, 1.00, 3.77, 4.88, 5.85, 6.8, 7.8, 10.7, 11.6, ... yr^{-1}. Apart from the first peak (which is perhaps rather the break between the regimes with a rising and declining overall trend), they are centred approximately on $1/P = mK \pm n$, where $K = 5.8$ is the precession frequency of the NSL and m and n are small integers. These are also the frequencies where false positives tend to appear in orbital solutions.

Corresponding plots for the bias in proper motion are shown in Fig. 12. The overall structure is similar, except that the declining trend for long periods has a much gentler slope ($|\Delta\mu| \propto P^{-1/3}$, whereas $|\Delta\varpi| \propto P^{-3/2}$ because even a long-period binary can bias the measured proper motion relative to that of the mass centre. Also, there are now minima approximately at $P = 2/n$ yr for $n = 1, 2, 3, \ldots$ (Fig. 13). This is probably related to another feature of the scanning law, namely that scanning patterns tend to be repeated annually (or semi-annually). Thus, if the binary completes an integer number of orbits in 1 or 2 years, the orbital motion might not affect the proper motion solution very much.

For the subsequent analysis it is also useful to have a subset of *effectively single stars*.[5] This can be defined by requiring a very small modelling error, for example $\mathrm{RMS}_5 < 1$ μas. In the three simulated binary samples the fraction of objects satisfying this criterion is 30.0% (32.2%) [31.9%] (Table 3). Figure 14 shows their distributions in the $(P, \Delta G)$ plane.

[5] A sample of truly single stars could of course easily be generated for example by setting $m_\mathrm{B} = 0$ in the binary model. However, it is more interesting to know what kind of actual binaries are astrometrically undetectable, which can be studied by means of the effectively single stars.

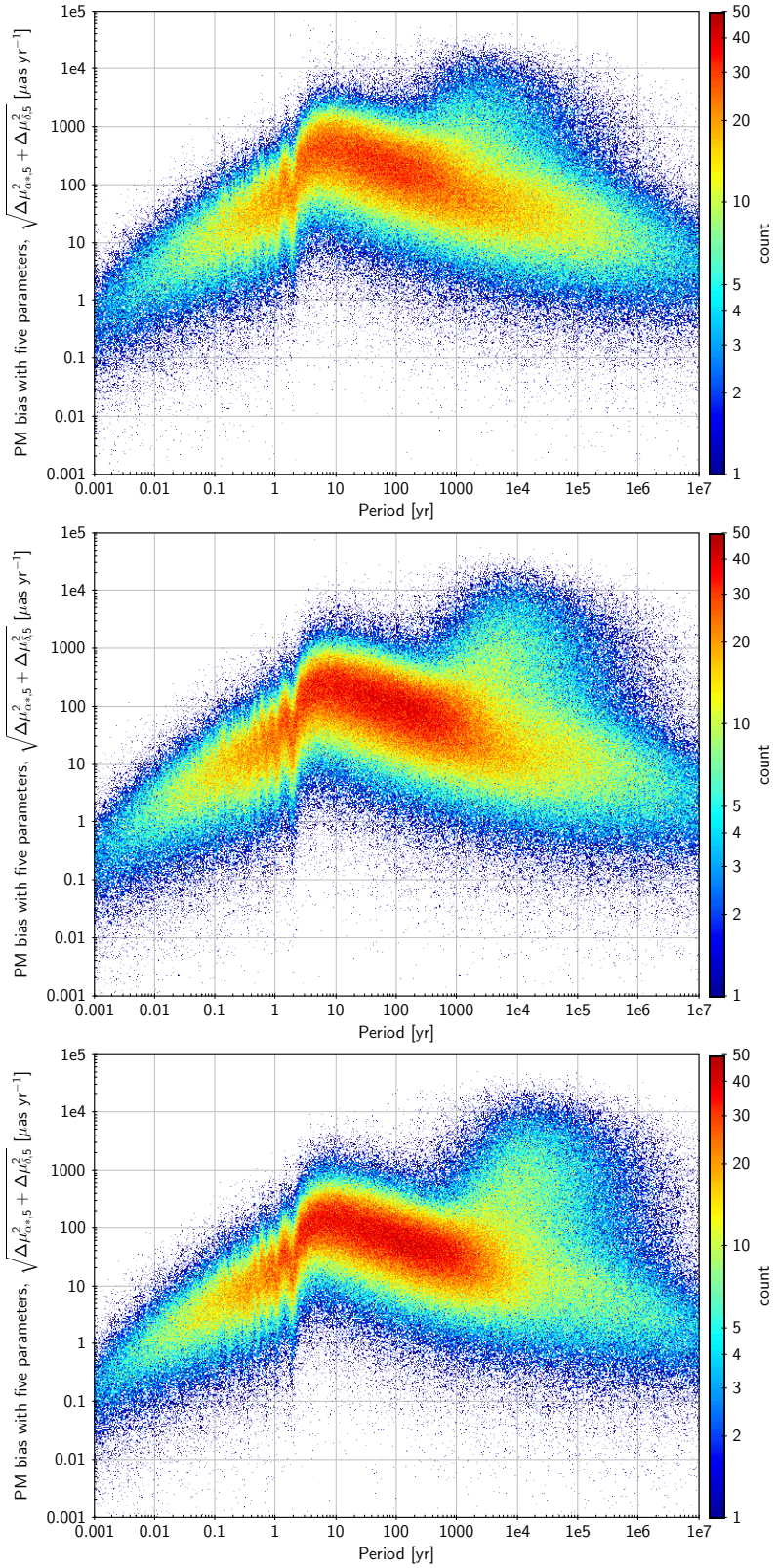

FIGURE 12: Total proper motion bias versus orbital period for $G = 12.5$ (top), 15.0 (middle), and 17.5 (bottom).

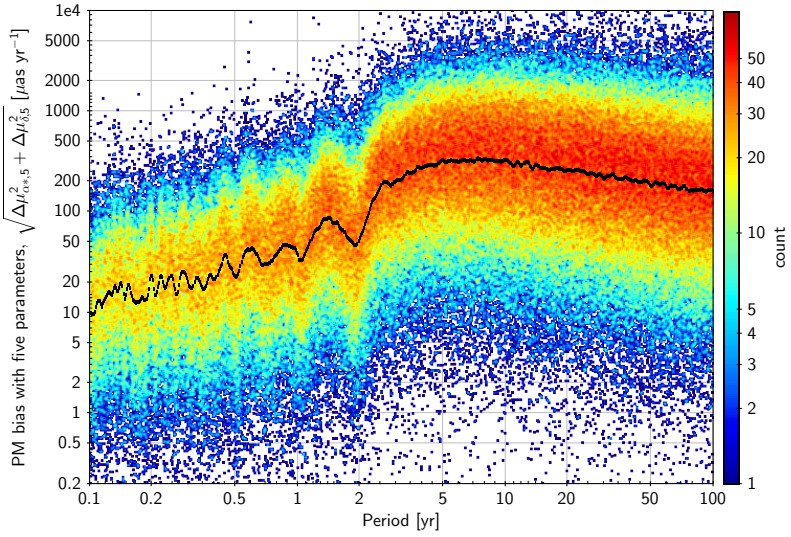

FIGURE 13: Same as Fig. 11 but for the proper motion bias.

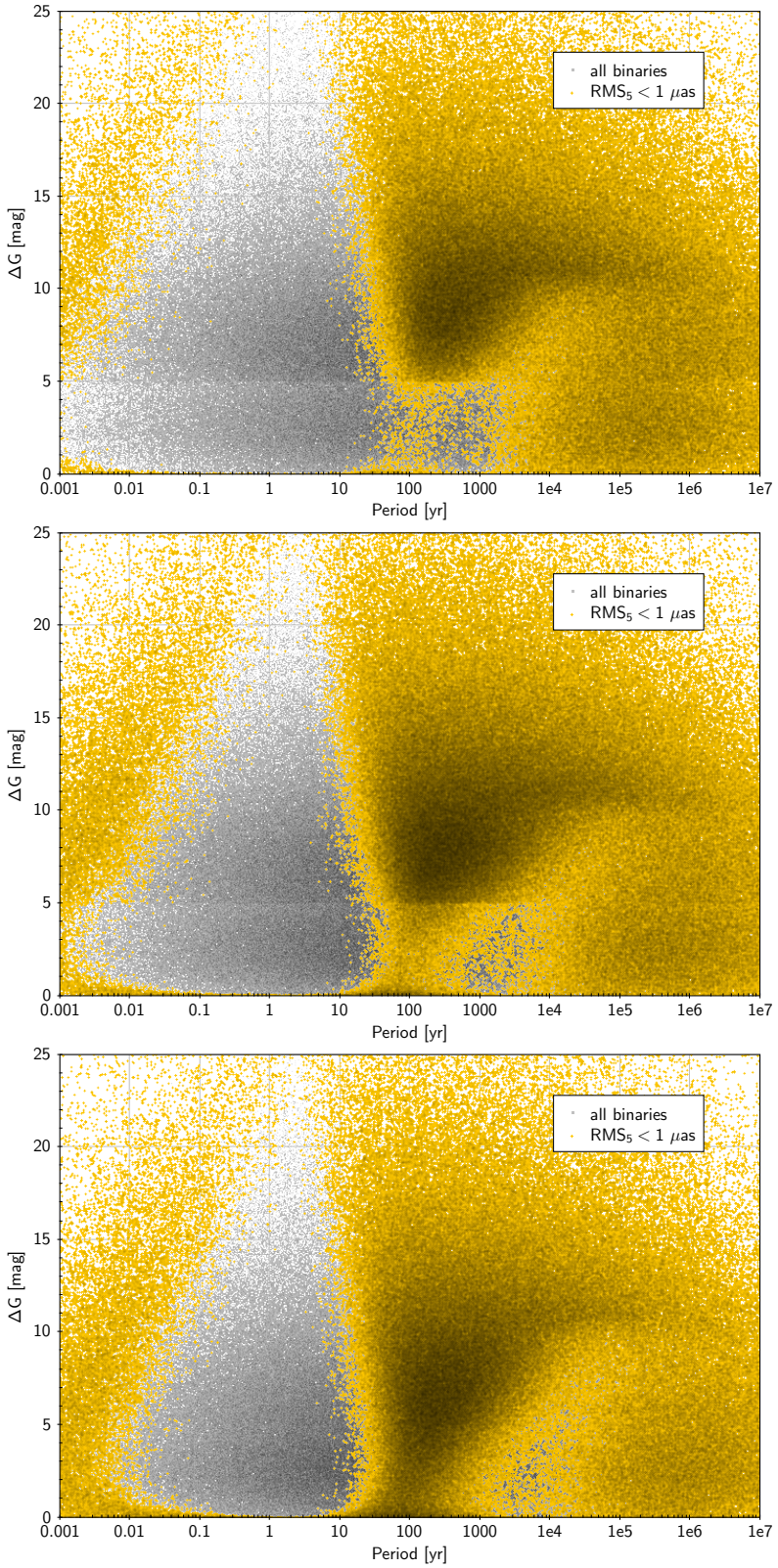

FIGURE 14: Distribution in the $(P, \Delta G)$ plane of all binaries (grey; cf. Fig. 2) and the effectively single stars, that is binaries that have negligible modelling error in the five-parameter solutions (orange). The panels are for $G = 12.5$ (top), 15.0 (middle), and 17.5 (bottom).

3.2 Noisy data (5p)

Recall that UWE_5 is the simulated equivalent of RUWE and therefore a main indicator of binarity. Figure 15 shows this statistic plotted versus period for the three samples of simulated binaries. A zoom on the most interesting interval of UWE is in Fig. 16.

Figure 17 shows the distribution of UWE_5 for the subset of effectively single stars defined in Sect. 3.1. As can be seen there is almost zero probability that an effectively single source in the simulations obtain a unit weight error exceeding 1.2. Conversely, it can be concluded that any source with $\mathrm{UWE}_5 > 1.2$ is *manifestly non-singular*. For the real data, the threshold in RUWE must in practice be set a bit higher than 1.2 (and dependent on at least G) to accommodate various imperfections in the renormalisation process and the stronger variation in the number of transits per source compared with the simulations. In the simulations the fraction of sources with $\mathrm{UWE}_5 > 1.2$ is 22.2% (12.1%) [6.7%], while in EDR3 the fraction with RUWE > 1.2 is 20.2% (11.3%) [7.3%]. Taken at face value, the similarity of these percentages could be interpreted as the fraction of binaries in EDR3 being $\sim$100%, but this of course neglects the broader distribution of RUWE. In order to bring down the percentages of EDR3 sources with RUWE $> x$ to become (for example) a factor two smaller than the percentages of simulated binaries with $\mathrm{UWE}_5 > 1.2$, one would require a threshold of $x \simeq 1.82$ (1.74) [1.55]. Looking at the blue curves in Fig. 7 this may be too conservative, and a more realistic threshold could be $x \simeq 1.5$ (1.4) [1.3]. The fraction of EDR3 sources with RUWE above this threshold is 12.7% (7.9%) [5.6%].

Thus we expect that out of the sources in EDR3, some 5–13% (mainly depending on G) EDR3 are manifestly non-single, as indicated by the standard five-parameter astrometric solutions. From Figs. 15–16 it can be seen that these will mainly have periods either in the range $\simeq 0.1$–10 yr (astrometric binaries) or between 100 and 1 million years (partially or fully resolved binaries). This is also seen in Fig. 18, showing the period distributions of the binaries with $\mathrm{UWE}_5 > 1.2$, and in Fig. 19, showing the joint distributions in period and magnitude difference. In the bright sample there is roughly an equal number of astrometric and resolved binaries, but among the fainter sources the proportion of astrometric binaries becomes progressively smaller.

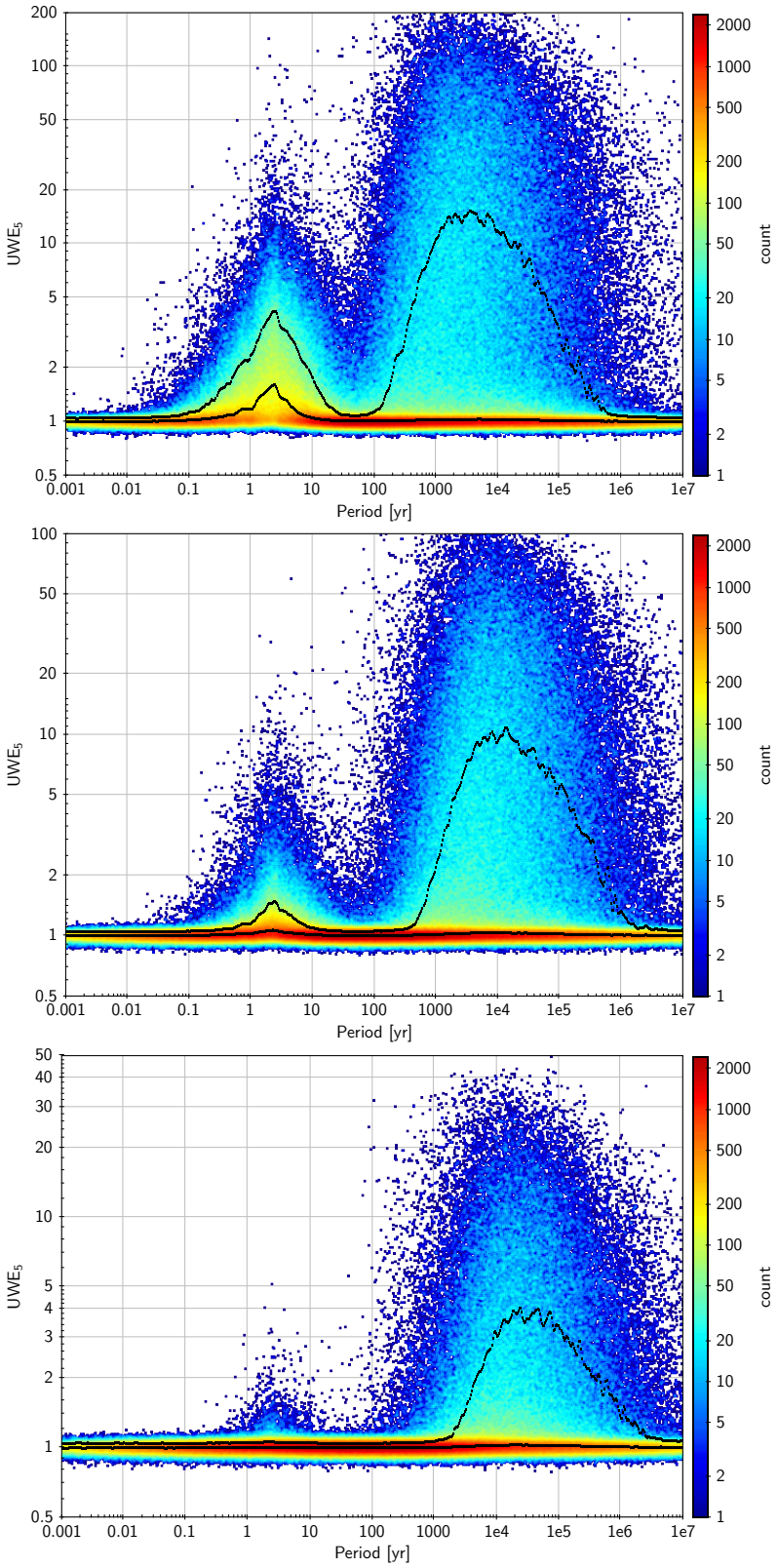

FIGURE 15: UWE in the five-parameter solution versus orbital period for $G = 12.5$ (top), 15.0 (middle), and 17.5 (bottom). The black curves are the 50th and 90th percentiles.

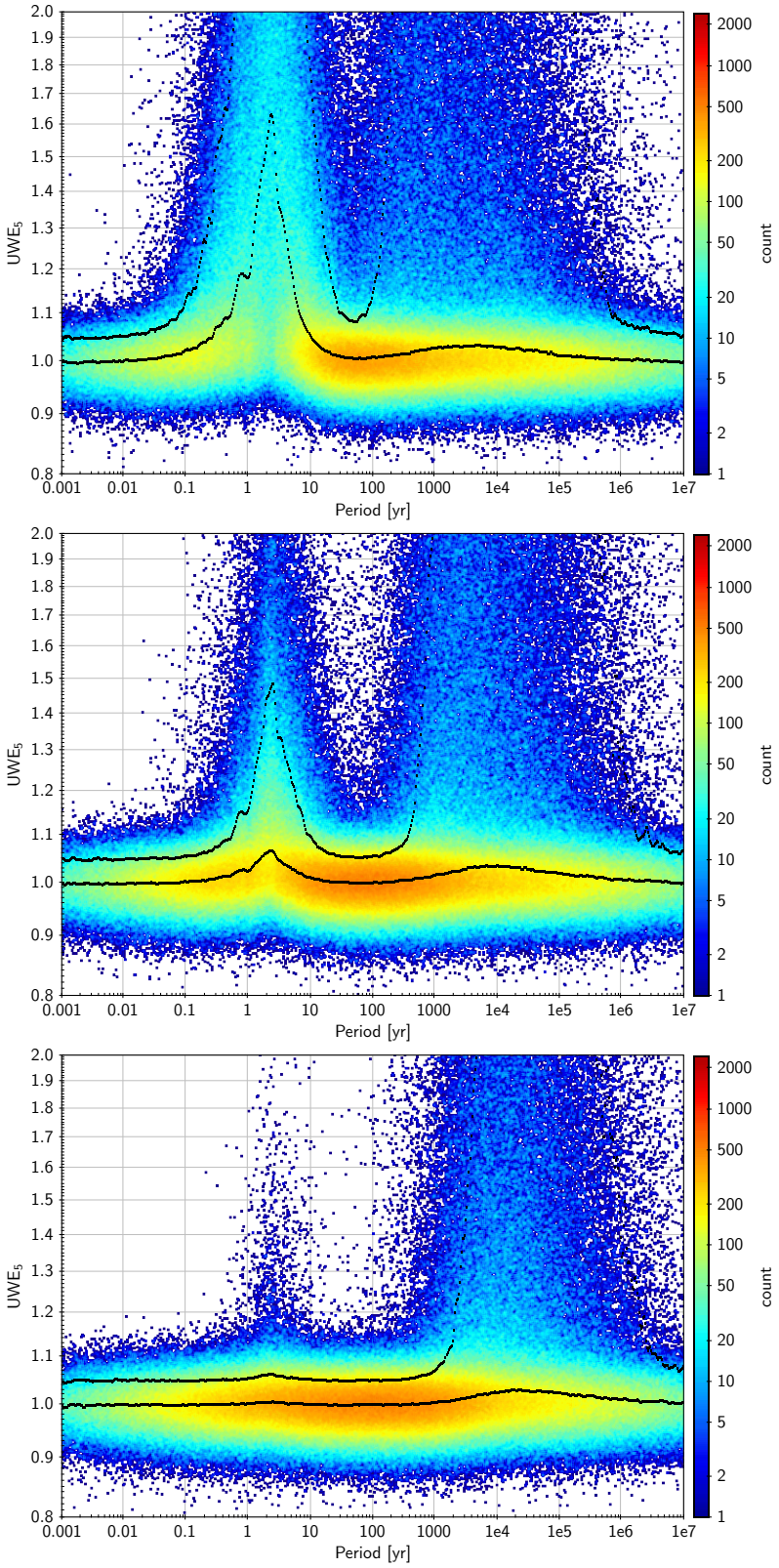

FIGURE 16: UWE in the five-parameter solution versus orbital period for $G = 12.5$ (top), 15.0 (middle), and 17.5 (bottom). The black curves are the 50th and 90th percentiles.

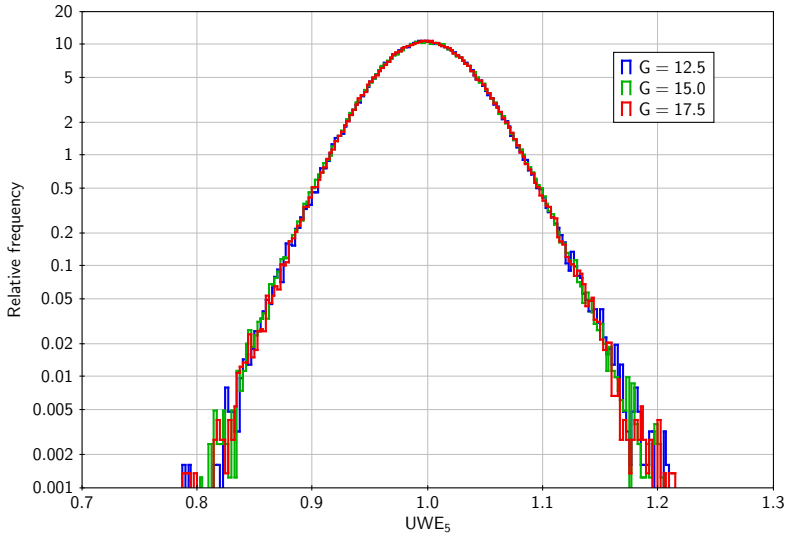

FIGURE 17: Histograms of UWE in the five-parameter solution for the simulated sub-samples of effectively single stars.

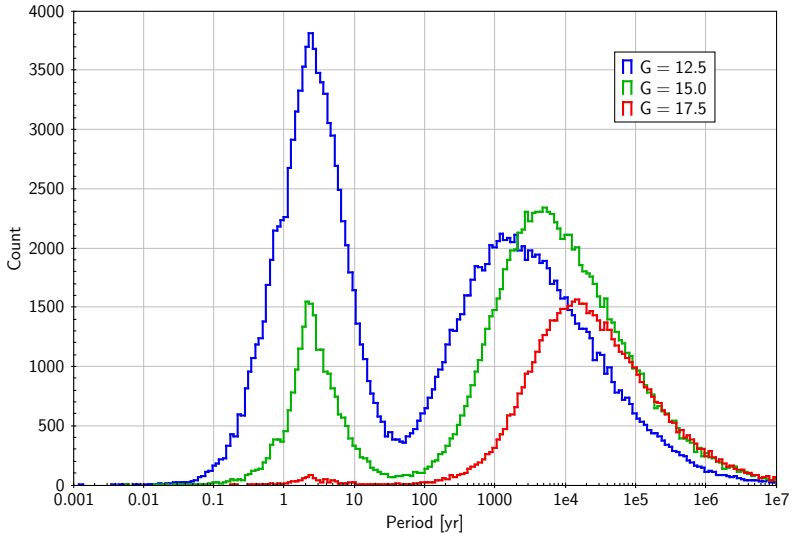

FIGURE 18: Period histograms for the 'manifestly non-single binaries' ($UWE_5 > 1.2$).

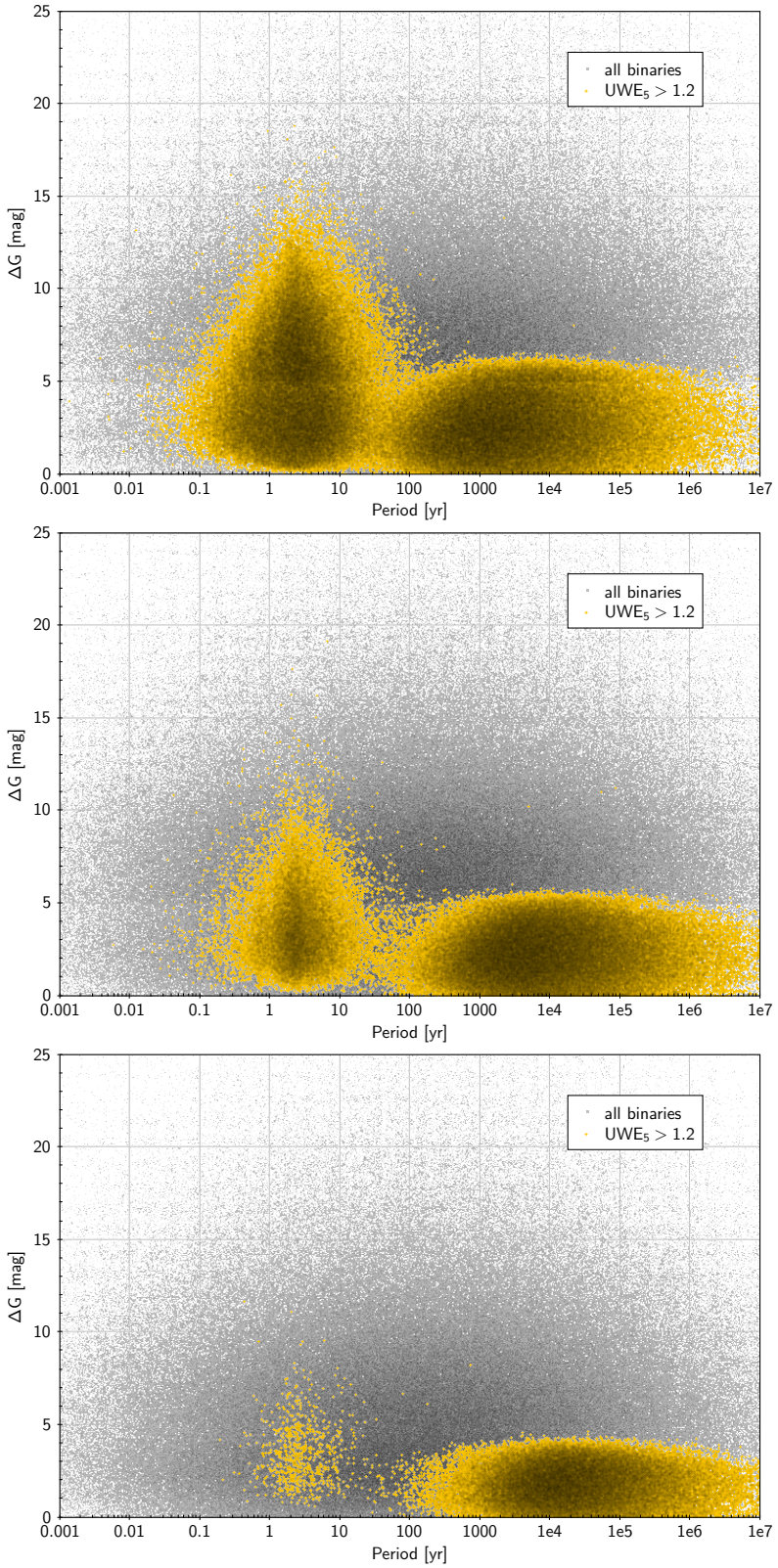

FIGURE 19: Distribution in the $(P, \Delta G)$ plane of all binaries (grey; cf. Fig. 2) and those with $\mathrm{UWE}_5 > 1.2$ (orange) for $G = 12.5$ (top), 15.0 (middle), and 17.5 (bottom).

4 Expected effects of binarity in seven-parameter solutions

4.1 Noise-free data (7p0)

Figure 20 shows the distribution in the $(P, \Delta G)$ plane of binaries that are not effectively single ($\mathrm{RMS}_5 > 1$ μas) but for which the seven-parameter solution provides an accurate model ($\mathrm{RMS}_7 < 1$ μas). As might be expected, most of them have periods in the range from about 5 to 500 yr and are thus typically unresolved; there are also some with much longer periods but large ΔG, so that the curved motion of the primary is observed undisturbed by the light from the secondary.

Although the limit used in this example (1 μas) is very strict and cannot be used in real selections (contrary to the UWE, the RMS modelling error is not known for noisy data), Fig. 20 gives some indication of where the 'true' acceleration solutions should be in the $(P, \Delta G)$ plane. This is even more clear when comparing with the manifestly non-single stars in Fig. 19. The latter contain many binaries with periods below $\simeq 5$ yr, and many more long-period binaries with $\Delta G \lesssim 5$ mag; for both these kinds of binaries the acceleration solution is not expected to bring any real improvement to the astrometry. Ideally, most of these cases should be filtered out in the real 7p solutions by application of suitable cuts based on the (noisy) 5p and 7p statistics. This is the main topic for the analysis below.

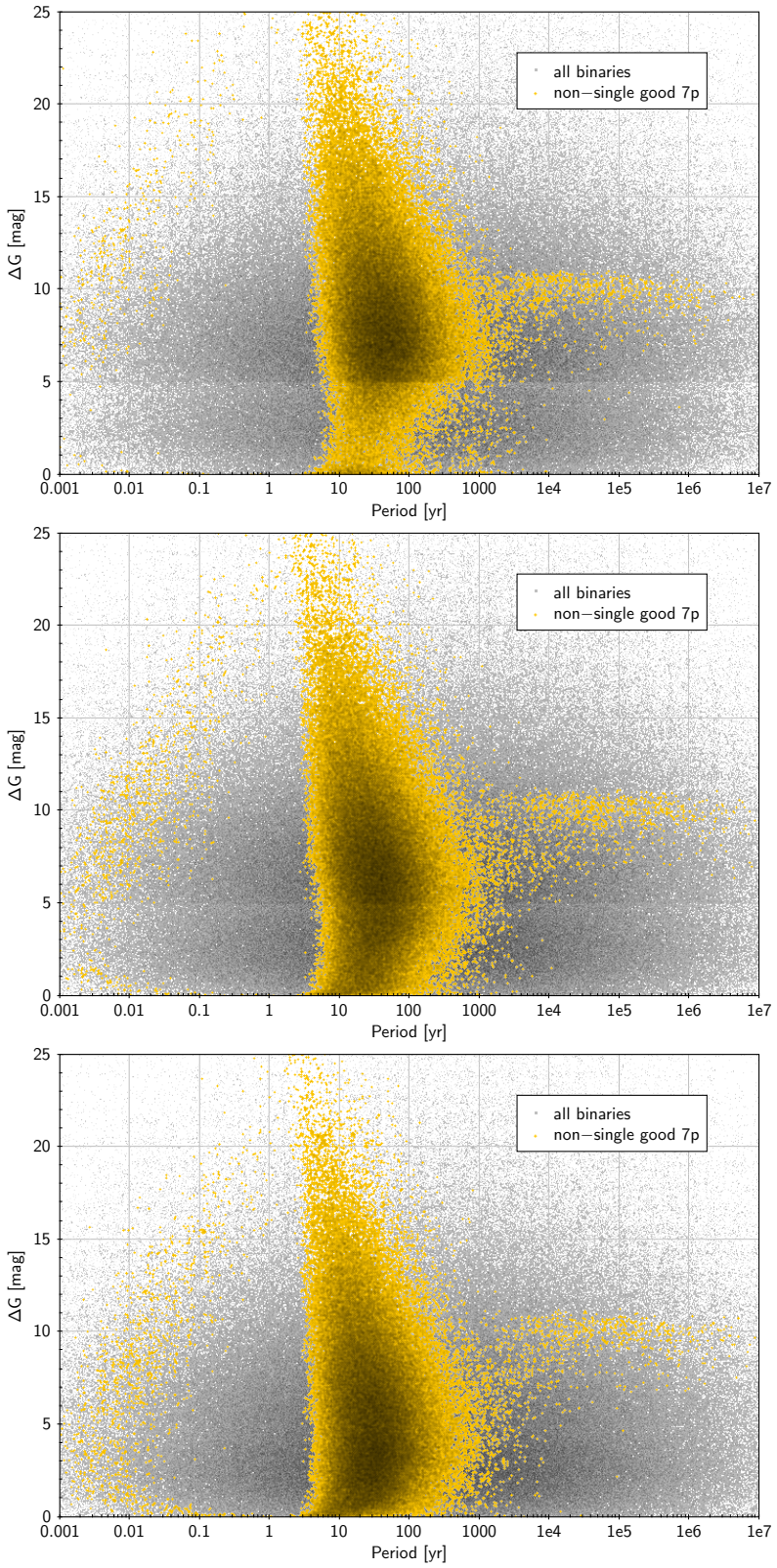

FIGURE 20: Distribution in the $(P, \Delta G)$ plane of all binaries (grey; cf. Fig. 2) and those with $\mathrm{RMS}_5 > 1$ μas and $\mathrm{RMS}_7 < 1$ μas (orange) for $G = 12.5$ (top), 15.0 (middle), and 17.5 (bottom).

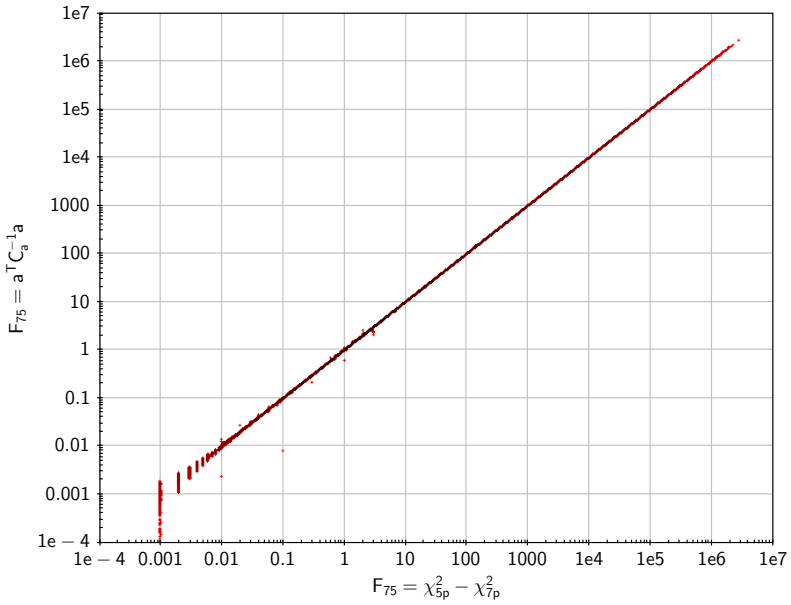

FIGURE 21: Comparison between F_{75} computed according to Eqs. (16) and (17) for the binaries with $G \simeq 15.0$ mag.

4.2 Noisy data (7p)

From a purely statistical point of view, the main statistic for deciding between the five- and seven-parameter solution is the reduction in chi-square from the 5p to the 7p solution, mathematically equal to the squared normalised acceleration terms in the 7p solution,

$$F_{75} = \chi^2_{5p} - \chi^2_{7p} \tag{16}$$

$$= \frac{1}{1-\rho^2}\left[\left(\frac{\dot{\mu}_{\alpha*}}{\sigma_{\dot{\mu}\alpha*}}\right)^2 + \left(\frac{\dot{\mu}_{\delta}}{\sigma_{\dot{\mu}\delta}}\right)^2 - 2\rho\left(\frac{\dot{\mu}_{\alpha*}}{\sigma_{\dot{\mu}\alpha*}}\right)\left(\frac{\dot{\mu}_{\delta}}{\sigma_{\dot{\mu}\delta}}\right)\right] . \tag{17}$$

Here ρ is the correlation coefficient between $\dot{\mu}_{\alpha*}$ and $\dot{\mu}_{\delta}$ in the 7p solution. The equivalence between the two expressions for F_{75} is not immediately obvious but is illustrated in Fig. 21. The small numerical differences between the two expressions visible in the figure are mainly caused by rounding errors in the saved χ^2 values.

For sources without acceleration terms (i.e. single stars) we expect F_{75} to follow the chi-squared distribution with two degrees of freedom, that is

$$\Pr\left[F_{75} > x \mid \text{no acceleration}\right] = \exp(-x/2) . \tag{18}$$

This is accurately confirmed by the distributions of F_{75} in the simulated data sets for effectively single stars (red curves in Fig. 22). For the full set of binaries (blue curves) there is of course an excess of sources with much larger F_{75}.

If the criterion $F_{75} > x$ is used to select sources with a significant acceleration, then $\exp(-x/2)$ is the probability of a false positive, i.e. of claiming that a truly non-accelerated source is accelerated. Since the criterion may be applied to a very large number sources, we want this

probability to be quite small, perhaps of the order of 10^{-4}, which requires $x \simeq 20$. The fraction of simulated binaries having $F_{75} > 20$ is 24.8% (14.1%) [6.0%].

Figure 23 shows the distributions in the $(P, \Delta G]$ plane of the sources with significant acceleration terms ($F_{75} > 20$). Comparing with the expected distribution of 'true' astrometric binaries in Fig. 20 shows that the selection includes many short-period astrometric binaries ($P \lesssim 2$ yr) and even more resolved systems ($P \gtrsim 100$ yr and $\Delta G \lesssim 5$ mag) for which the improved fit to the 7p model is probably fortuitous and unphysical.

To improve the selection one must apply additional filters based on the absolute quality of the 7p solutions (not just in comparison with 5p), or other criteria such as the detection of multiple peaks. Figure 24 shows the distributions when the criterion $\mathrm{UWE}_7 < 1.2$ is added: this removes most, but not all, of the fortuitous acceleration solutions.[6] The fraction of simulated binaries passing this selection is 9.2% (5.2%) [1.0%]. To estimate the number of spurious detections in these samples we use the criterion derived in Appendix C. From this we find that about 16% (36%) [57%] of the selected systems are false positives (Table 3).

One might consider using a somewhat harsher filter like $\mathrm{UWE}_7 < 1.1$ (Fig. 25), reducing the fraction of accepted binaries to 7.3% (4.2%) [0.6%]. Of these, 4% (10%) [38%] are false positives by the criterion in Appendix C. Thus, using a stricter upper limit on UWE_7 does indeed lead to a cleaner sample of acceleration solutions.

[6] In practice, the limit on UWE_7 needs to be adjusted based on the empirical distribution of this quantity for *bona fide* single stars, similar to what was done for the calculation of RUWE, and probably depending on both the magnitude and the colour of the source.

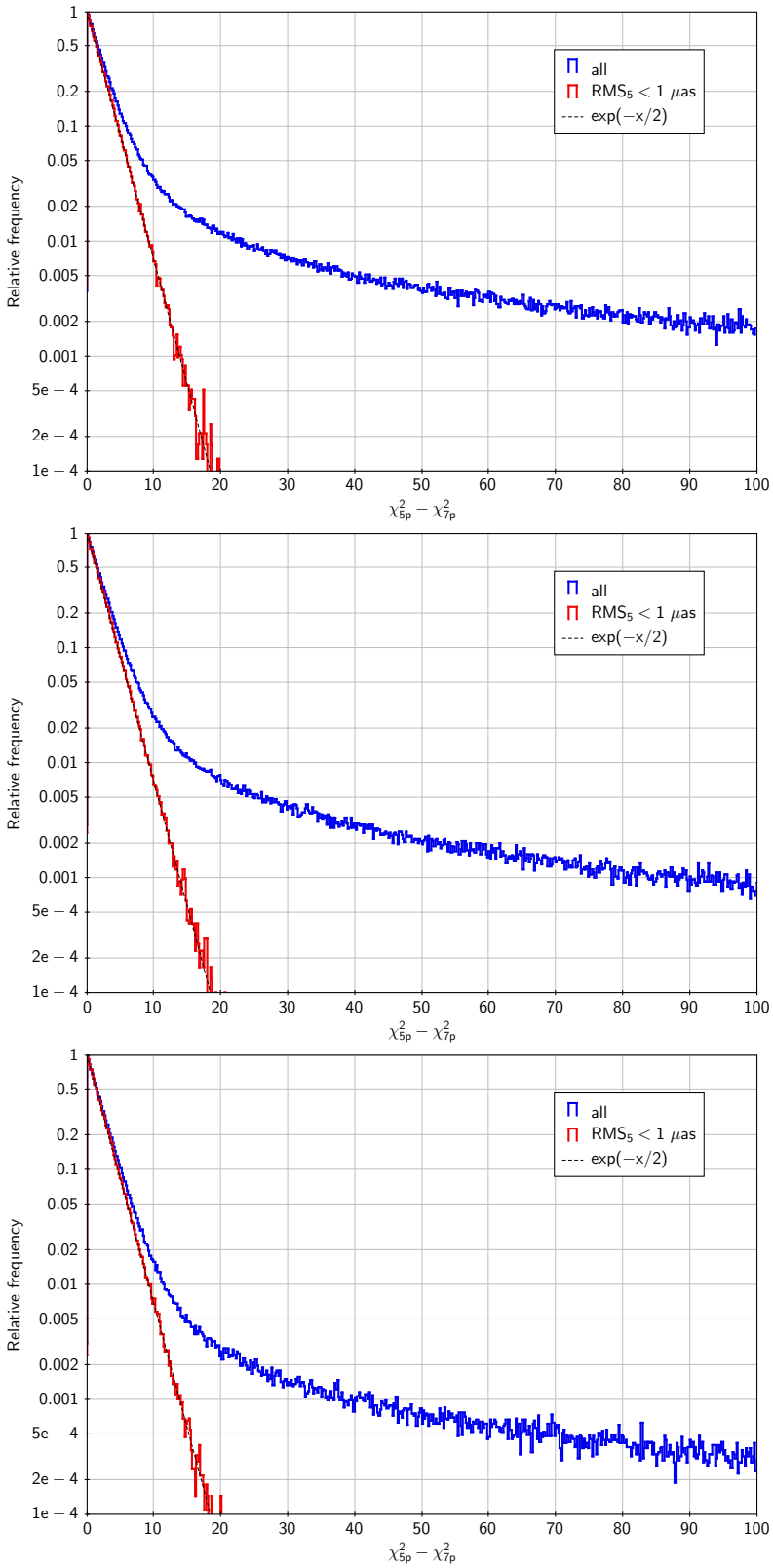

FIGURE 22: Distribution of $F_{75} = \chi^2_{5p} - \chi^2_{7p}$ for the effectively single stars (red) and all the binaries (blue) for $G = 12.5$ (top), 15.0 (middle), and 17.5 (bottom). All histograms are normalised to 1 in the first (highest) bin.

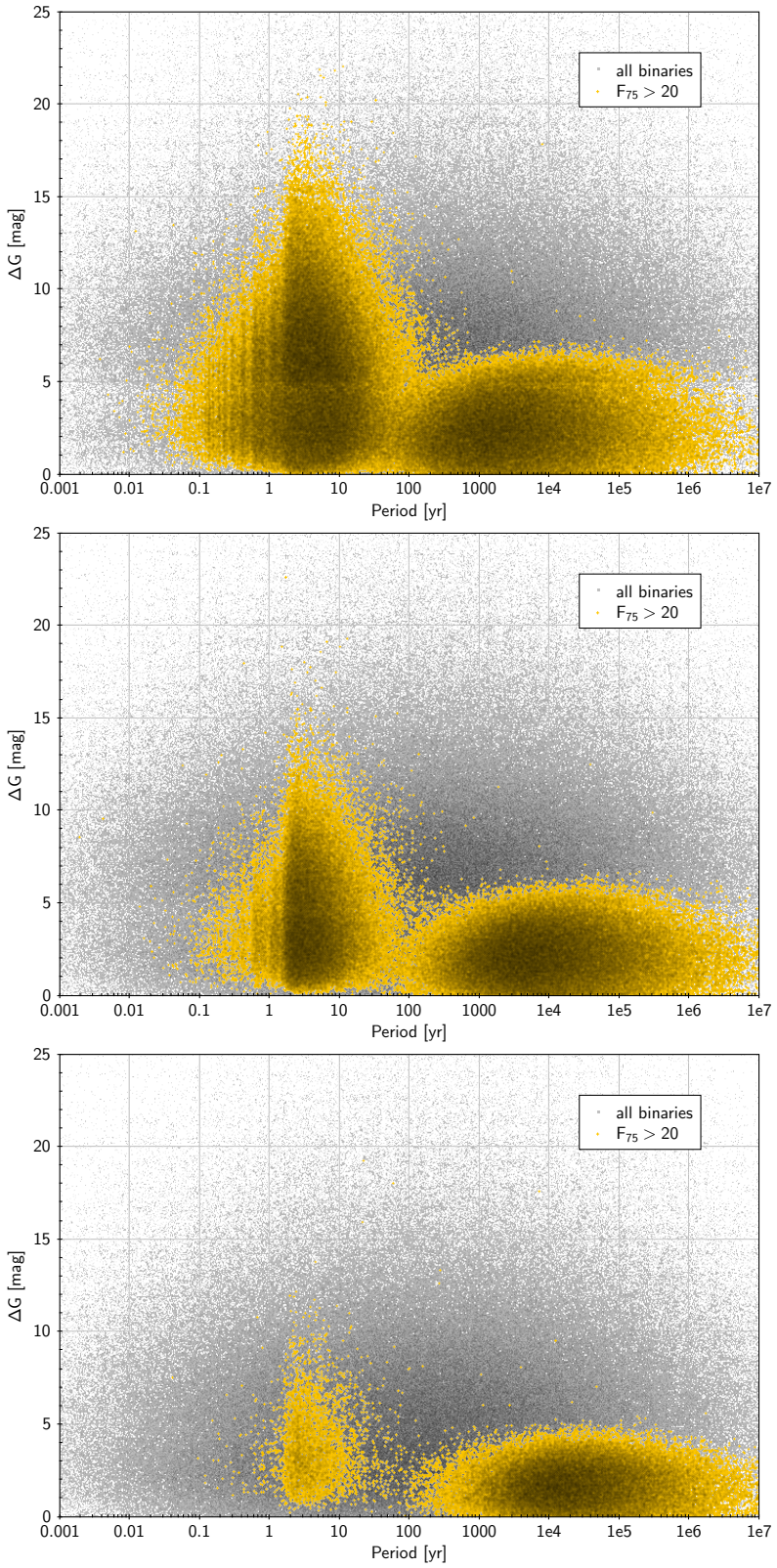

FIGURE 23: Distribution in the $(P, \Delta G)$ plane of all binaries (grey; cf. Fig. 2) and those with significant acceleration terms ($F_{75} > 20$; orange) for $G = 12.5$ (top), 15.0 (middle), and 17.5 (bottom).

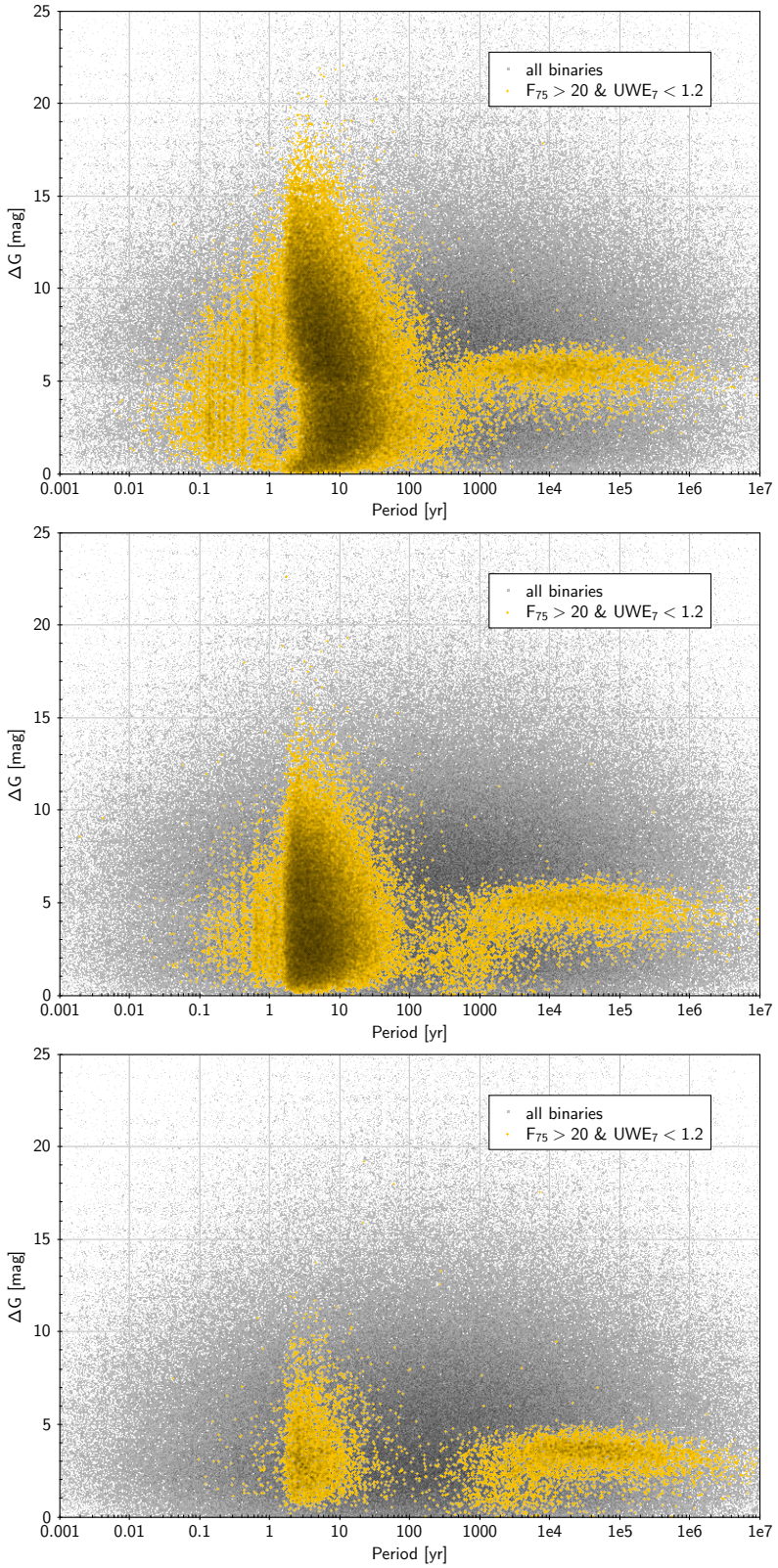

FIGURE 24: Distribution in the $(P, \Delta G)$ plane of all binaries (grey; cf. Fig. 2) and those with significant and good acceleration solutions ($F_{75} > 20$ and $\mathrm{UWE}_7 < 1.2$; orange) for $G = 12.5$ (top), 15.0 (middle), and 17.5 (bottom).

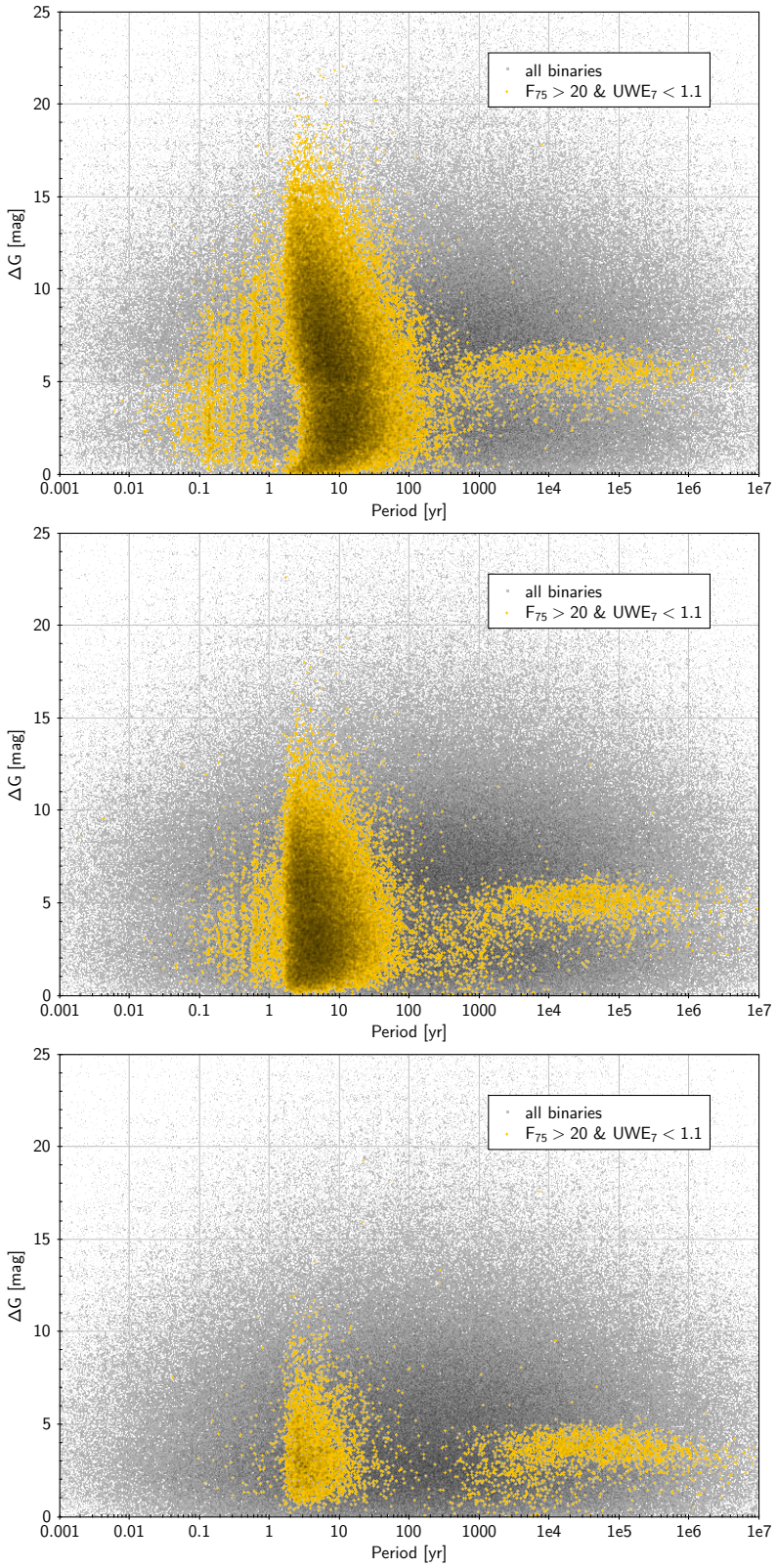

FIGURE 25: Distribution in the $(P, \Delta G)$ plane of all binaries (grey; cf. Fig. 2) and those with significant and good acceleration solutions ($F_{75} > 20$ and $\mathrm{UWE}_7 < 1.1$; orange) for $G = 12.5$ (top), 15.0 (middle), and 17.5 (bottom). Compared with Fig. 24 the selection on UWE_7 is here stricter, resulting in a smaller and probably cleaner sample.

4.3 Comparing the observed and true accelerations

The efficiency of the filters discussed in the preceding section can also be tested by comparing the observed acceleration values in the 7p solutions with the 'true' values computed analytically from the orbital parameters as described in Appendix B. These 'true' accelerations are instantaneous values for the photocentre at the reference epoch ($t_{\rm ref} = 2016.0$); for periods shorter than a few years they are fairly irrelevant to the observations (and can attain very large values), but for longer periods they should ideally agree with the observed values to within the statistical uncertainties, at least for systems that are either unresolved or have a large flux ratio.

The top diagram of Fig. 26 shows the distribution of the 'true' acceleration versus period for the simulated sample of $G = 15.0$ binaries. (The slight discontinuity in the distribution at $P \simeq 3$ yr is caused by the change in eccentricity distribution for $P = 1000$ days, see Eq. 4.) There is a very strong correlation between period and acceleration, approximately given by $|\dot{\mu}| = cP^{-4/3}$ with $c = 4.6$ (2.5) [1.7] mas yr$^{-2/3}$, albeit with a large scatter of about 0.6 dex (standard deviation) about the mean relation. This relation, shown by the dashed line, is also given in some of the subsequent plots to facilitate comparison.

The middle and bottom panels in Fig. 26 show the observed acceleration $|\dot{\mu}| = \sqrt{\dot{\mu}_{\alpha*}^2 + \dot{\mu}_{\delta}^2}$ for the noise-free (7p0) and noie (7p) solutions. Comparing the three panels it is very clear that only a relatively narrow range of periods will produce meaningful 7p solutions: for $P \lesssim 2$ yr the period is too short to be fitted by the 7p model; for $P \gtrsim 100$ yr the true acceleration is normally too small to be detected but many of these systems will obtain spurious accelerations produced by resolution effects (Appendix D).

The top and middle panels of Fig. 27 show the effect of selecting solutions with significant acceleration terms ($F_{75} > 20$). This removes most of the systems with $P < 2$ yr or $P > 100$ yr, as well as many intermediate-period binaries with true accelerations that are too small in relation to the observation noise. However, it still leaves a substantial number of spurious accelerations among the long-period systems. Adding the criterion UWE$_7 < 1.2$ results in a much cleaner sample (bottom panel), although it still contains some 7% (10%) [54%] systems with $P > 100$ yr, most of which are probably spurious.

Figure 28 is a direct comparison of the observed and true accelerations in right ascension for the good significant subsample of the 7p solutions. (The corresponding plots in declination are not shown, as they are qualitatively extremely similar.) Except for periods shorter than about 2 yr (shown as orange dots), there is in general a good positive correlation between the true and observed values; however, along the line at zero abscissa one can also see some spurious observed accelerations, most clearly for $G = 17.5$. These are the long-period false positives mentioned above.

A useful measure of the dissimilarity between the observed acceleration ($\dot{\boldsymbol{\mu}}_7$) and the true acceleration of the photocentre ($\dot{\boldsymbol{\mu}}^0_{\rm PC}$) is the squared Mahalanobis distance,

$$D_7 = (\dot{\boldsymbol{\mu}}_7 - \dot{\boldsymbol{\mu}}^0_{PC})' \, \boldsymbol{C}^{-1}_{\dot{\boldsymbol{\mu}}} (\dot{\boldsymbol{\mu}}_7 - \dot{\boldsymbol{\mu}}^0_{PC}) \,, \tag{19}$$

which takes into account the deviations in both RA and Dec. For binaries where the seven-parameter model is an accurate representation of the photocentre orbit during the observation interval, D_7 should follow the chi-squared distribution with two degrees of freedom, on a logarithmic axis giving a maximum at $\ln 2 \simeq 0.693$ and a median of $\ln 4 \simeq 1.386$. The actual distribution of D_7 versus period for the $G = 12.5$ sample (top panel of Fig. 29) shows that this is approximately true for $P \gtrsim 10$ yr, as expected, but not for periods much shorter than a few years where the 7p model is not a good representation of the orbit. For much longer periods ($P \gtrsim 100$ yr) there is however a tail of large D_7 values, indicating that the photocentre is not consistently observed. This is confirmed by the location dispersion $\sigma_{\rm O}$ (Eq. 62) plotted in the middle panel. As explained in Appendix D, a large $\sigma_{\rm O}$ means that there is no well-defined point in the binary (such as the photocentre or primary) that is consistently observed.

The bottom panel of Fig. 29) shows the same statistics as in the middle panel, but only for the binaries with significant acceleration, $F_{75} > 20$. Here most of the long-period binaries with D_7 of order unity (for which the estimated acceleration is consistent with the true acceleration) have been filtered out, because their accelerations are too small to be detected; of the long-period systems the ones retained usually have spurious accelerations caused by the location dispersion.

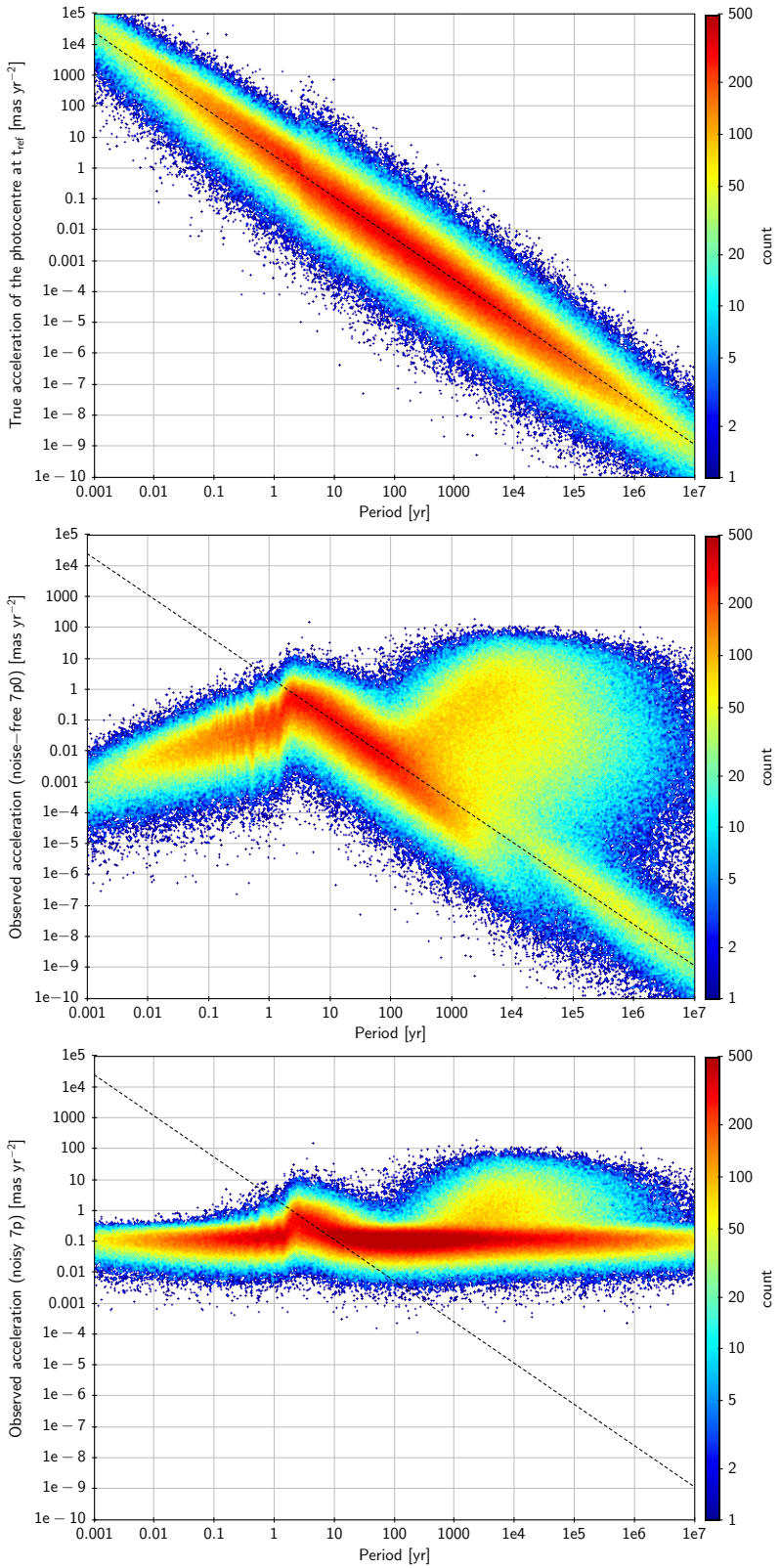

FIGURE 26: Total acceleration $|\dot{\mu}|$ versus period for the binaries with $G = 15.0$. *Top:* true acceleration of the photocentre at the reference epoch. *Middle:* observed acceleration in noise-free case (7p0). *Bottom:* observed acceleration in the noisy case (7p). The dashed line, showing the relation $|\dot{\mu}| = 2.5P^{-4/3}$, was added to guide the eye.

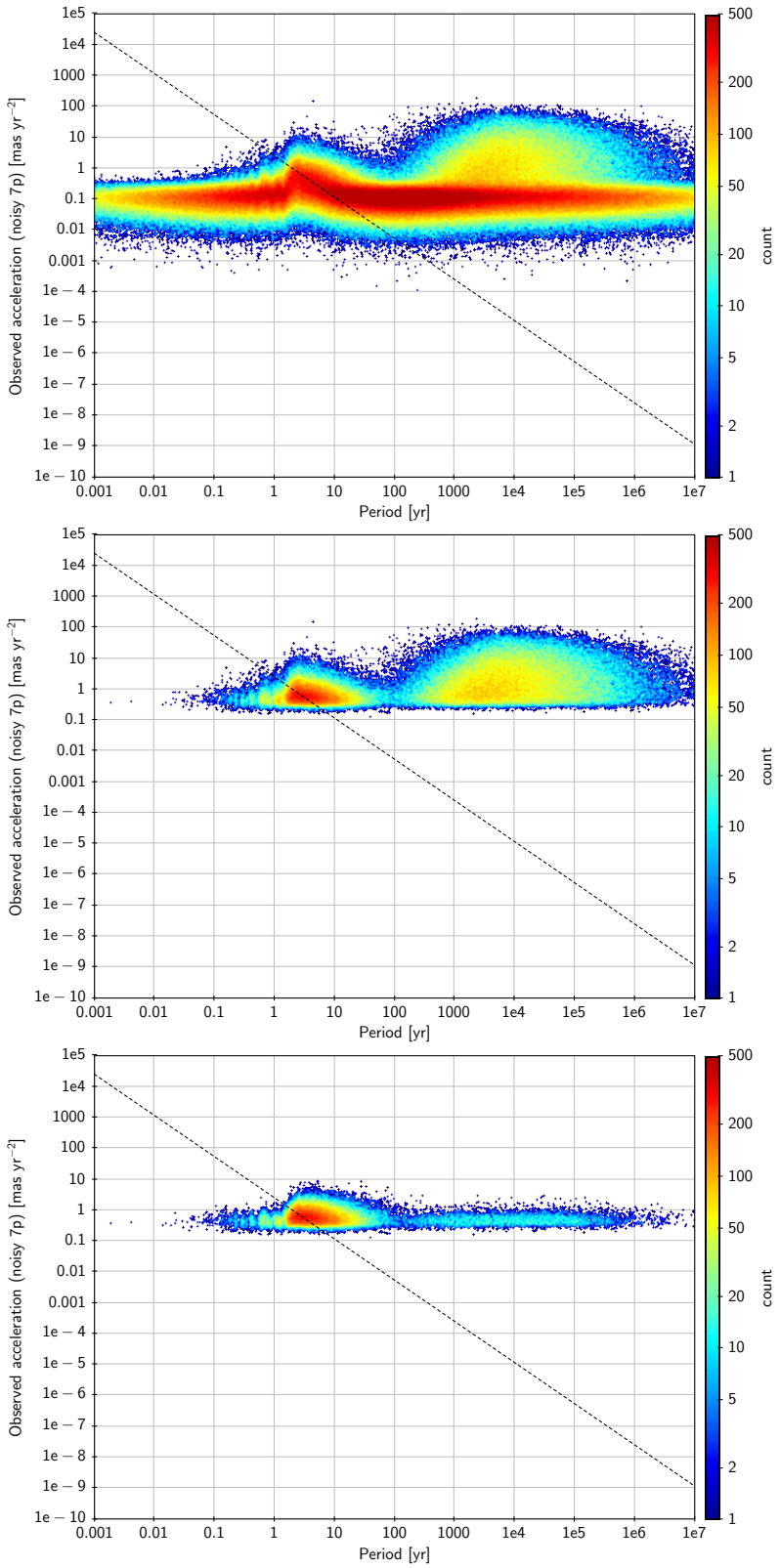

FIGURE 27: Total observed acceleration $|\dot{\mu}|$ versus period for the 7p solutions of binaries with $G = 15.0$. *Top:* all binaries (this is the same as the bottom panel in Fig. 26). *Middle:* the subsample with significant solutions, $F_{75} > 20$. *Bottom:* the subsample with good significant solutions, $F_{75} > 20$ & $\mathrm{UWE}_7 < 1.2$. The dashed line is the same as in Fig. 26.

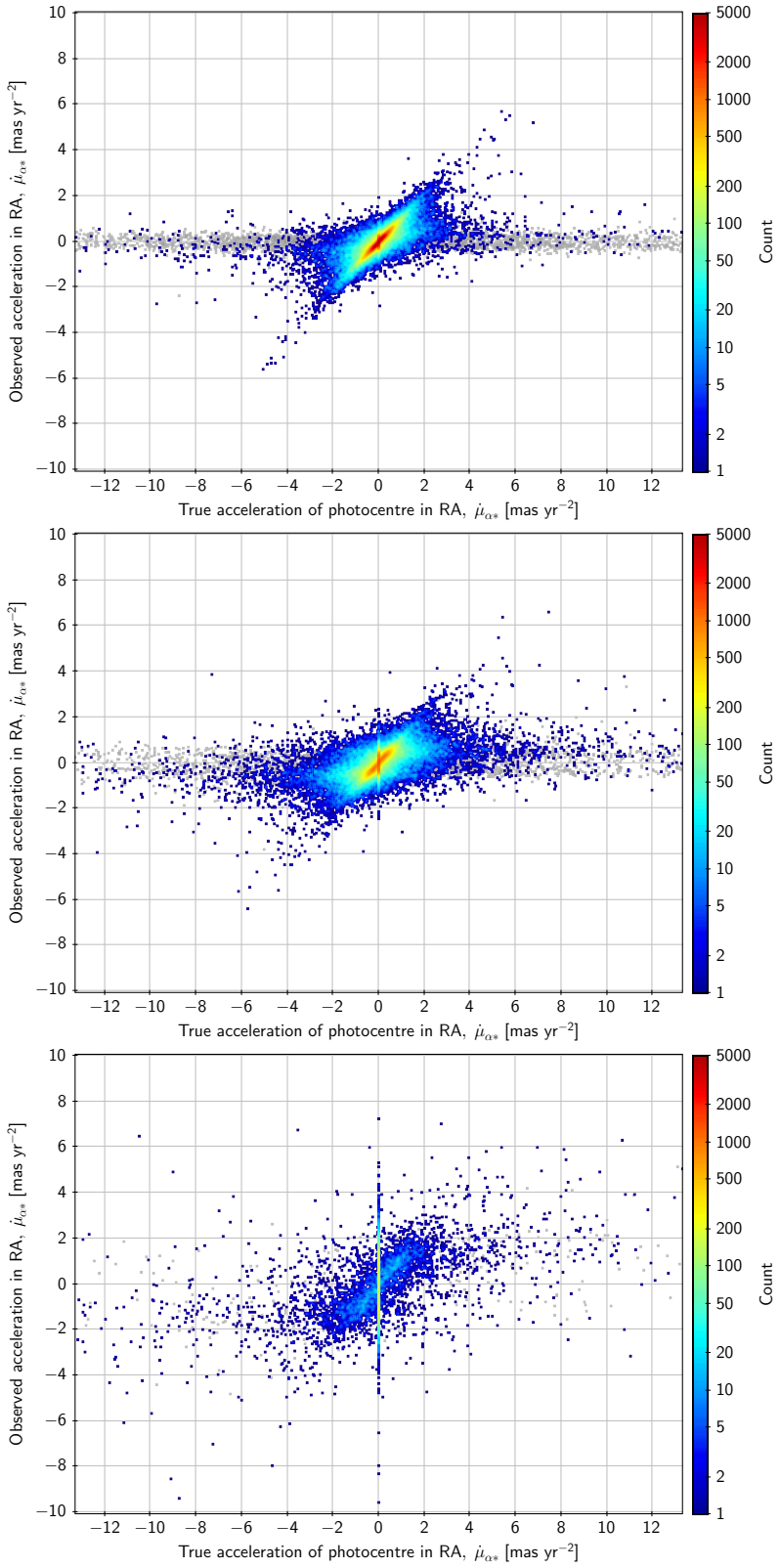

FIGURE 28: Observed versus true acceleration for the samples with good significant 7p solutions ($F_{75} > 20$ & $\mathrm{UWE}_7 < 1.2$) at $G = 12.5$ (top), 15.0 (middle), and 17.5 (bottom). The grey dots have $P < 2$ yr.

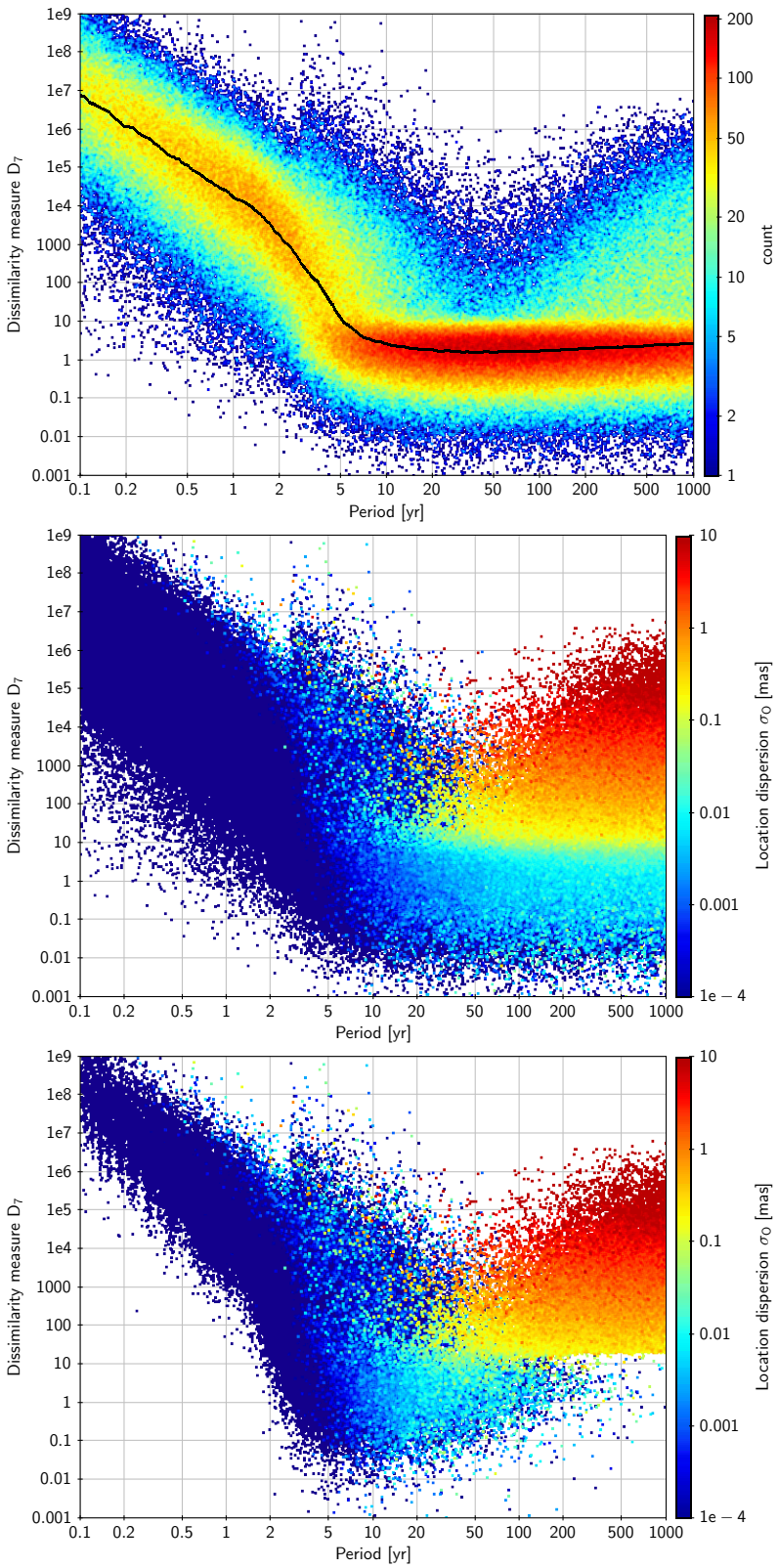

FIGURE 29: Dissimilarity measure D_7 between the acceleration according to the 7p solution and the true acceleration of the photocentre at the reference epoch, for the $G = 12.5$ sample. *Top:* density of all binaries. *Middle:* same as is the top panel but colour-coded by the location dispersion. *Bottom:* same as the middle panel, but for binaries with $F_{75} > 20$.

4.4 Using the minimum secondary mass as a reality check

Bastian (in the unpublished TN BAS-044) gives formulae for estimating the minimum mass of the perturbing (secondary) component based on the measured acceleration and parallax, an assumed mass for the perturbed (primary) component, and an assumed minimum orbital period.

In BAS-044 the minimum secondary mass is denoted $M_{2,\mathrm{min}}$, but for consistency with other notations in this TN it is here called $m_{\mathrm{B,min}}$. Using Eq. (24) in BAS-044 we calculate $m_{\mathrm{B,min}}$ for the simulated binaries using the estimated acceleration and parallax in the 7p solution (that is, including observation noise on both quantities), $m_{\mathrm{A}} = 1\ M_{\odot}$ (always true for the simulations), and $P_{\mathrm{min}} = 5.7$ yr (following the suggestion in BAS-044).[7]

Figure 30 shows the distribution of $m_{\mathrm{B,min}}$ (`M2minN` in Table 2) for the full set of binaries (blue histograms), sources with significant acceleration terms ($F_{75} > 20$; blue-green histograms), and good 7p solutions ($F_{75} > 20$ & $\mathrm{UWE}_7 < 1.2$; red histograms), together with the distributions of true secondary masses in the good 7p solutions (shaded histograms). It is seen that the condition $\mathrm{UWE}_7 < 1.2$ drastically reduces the number of solutions with high $m_{B,\mathrm{min}}$, at least for the the brighter sources.

Clearly a criterion such as $m_{\mathrm{B,min}} < 0.33\ M_{\odot}$ (as suggested in BAS-044) removes a number of unphysical solutions, but does it reduce the fraction of false positives? To answer this, it is necessary to define what is meant by a false positive. This question is considered in Appendix C and D, where Eq. (63) is proposed as a reasonable criterion. Relevant statistics are summarised in Table 3. With the selection $F_{75} > 20$ & $m_{\mathrm{B,min}} < 0.33\ M_{\odot}$ the fraction of false positives is found to be 55.3% (62.3%) [94.9%]. This can be compared with the fraction of false positives when using the criterion $F_{75} > 20$ & $\mathrm{UWE}_7 < 1.2$, which is 15.3% (15.6%) [56.9%]. The comparison is not really fair, as the criterion using $m_{\mathrm{B,min}}$ gives a significantly higher number of accepted solutions at all magnitudes. However, if the $m_{\mathrm{B,min}}$ criterion is applied on top of the UWE_7 criterion, the fraction becomes 19.3% (22.9%) [44.9%], which is an improvement, compared with not using $m_{\mathrm{B,min}}$, only for the faintest magnitude. Thus, we may conclude that the use of $m_{\mathrm{B,min}}$ is less effective to sort out false positives than the UWE_7 criterion.

[7] Table 2 also lists the theoretical quantity M2min0 $= m^0_{\mathrm{B,min}}$. This is the minimum secondary mass calculated in the same way as $M_{2,\mathrm{min}}$, but using the true projected acceleration of the primary at the reference epoch, $|\dot{\mu}^0_{\mathrm{A}}|$ (see Appendix B), the actual parallax, $m_{\mathrm{A}} = 1\ M_{\odot}$, and the actual period P. This value is of course only available for the simulations and was used to test certain approximations involved in the calculation of the observed $m_{\mathrm{B,min}}$. It is not further discussed here.

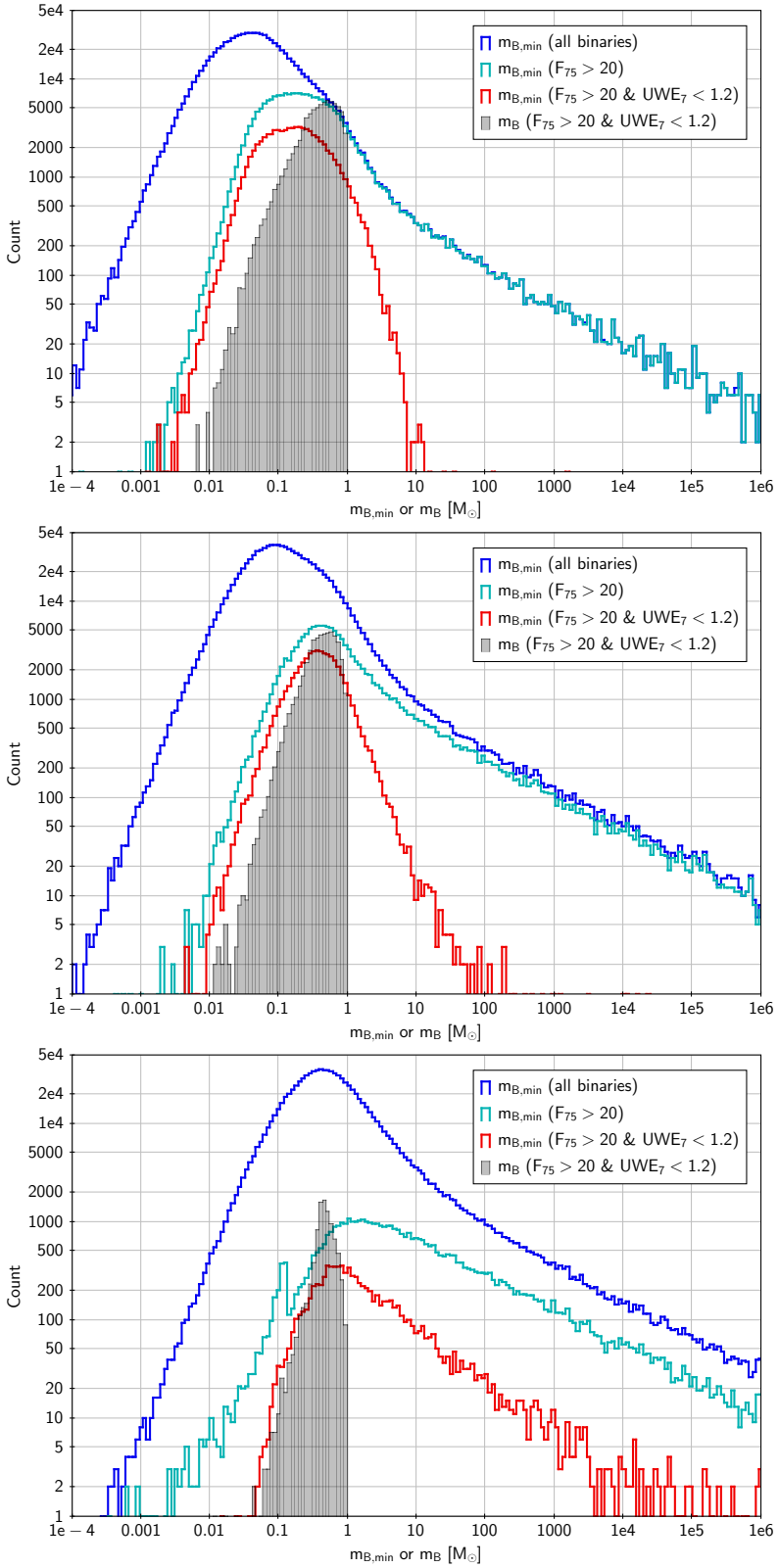

FIGURE 30: Distribution of the estimated minimum secondary mass ($m_{\mathrm{B,min}}$) and actual secondary mass (m_{B}) for $G = 12.5$ (top), 15.0 (middle), and 17.5 (bottom).

5 Parallax errors in 5p and 7p solutions

We do not observe any bias in the parallaxes obtained in the 5p or 7p solutions, but the individual errors are often much greater than the formal uncertainties. Figure 31 shows the median absolute parallax error versus period for the subsets of effectively single stars, and for the 5p and 7p solutions of the sources with significant acceleration. The median absolute errors for sources with significant accelerations are up to 10–20 times larger than for the effectively single stars, but this factor is a strong function of the period: there is a local maximum at $P \simeq 1$ yr, a broad minimum at 5–50 yr, and high values for periods exceeding 100–1000 yr. Considering only the good significant accelerations (Fig. 32) the behaviour is much more benign for the long-period binaries. Only for intermediate periods (2–200 yr) is there a clear, and sometimes strong, improvement of parallaxes in the 7p solutions compared with 5p.

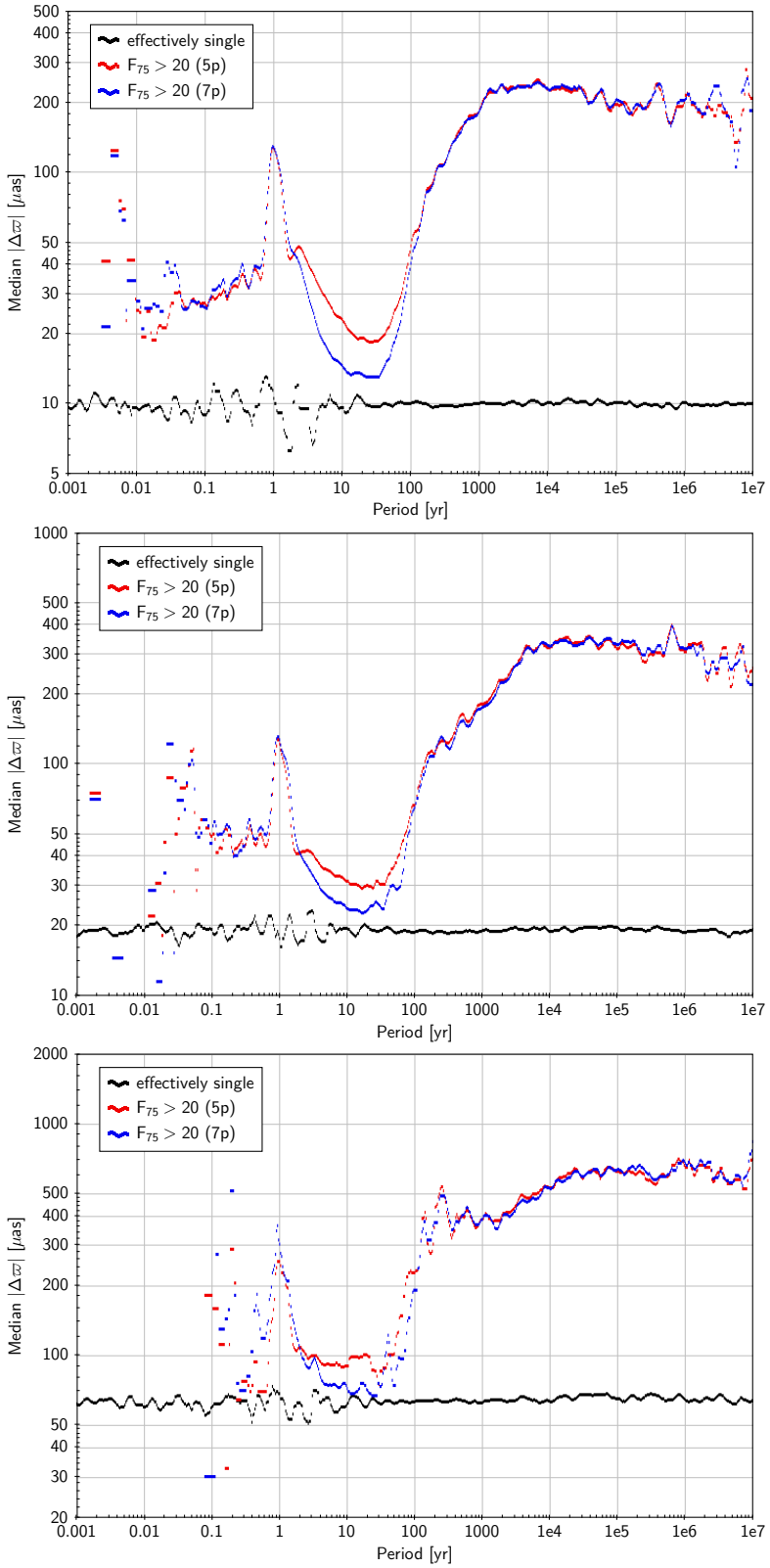

FIGURE 31: Median absolute parallax error for effectively single stars (black) and for the 5p (red) and 7p (blue) solutions of sources with significant acceleration ($F_{75} > 20$), for $G = 12.5$ (top), 15.0 (middle), and 17.5 (bottom).

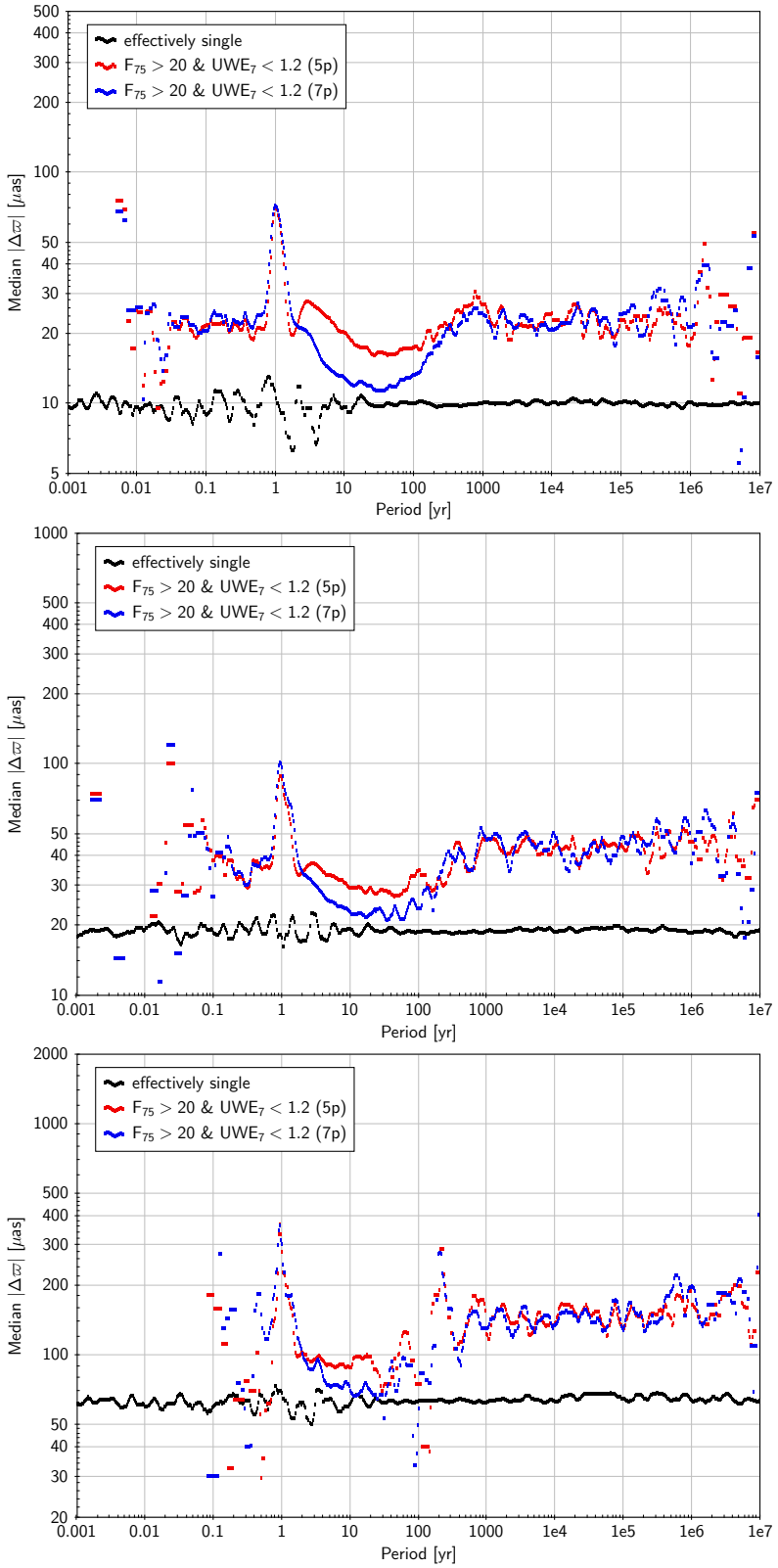

FIGURE 32: Median absolute parallax error for effectively single stars (black) and for the 5p (red) and 7p (blue) solutions of sources with significant and good acceleration ($F_{75} > 20$ and $\mathrm{UWE}_7 < 1.2$), for $G = 12.5$ (top), 15.0 (middle), and 17.5 (bottom).

6 Nine-parameter solutions

The simulations make it easy to simulate also nine-parameter solutions, both noise-free (9p0) and noisy (9p). The models are straightforward extensions of Eqs. (13) and (14), obtained by adding terms proportional to $\tau^3/6$. The resulting jerk terms are denoted $\ddot{\mu}_{\alpha*}$ and $\ddot{\mu}_\delta$. Statistics are analogously defined, for example

$$\mathrm{UWE}_9 = \sqrt{\frac{\chi^2_{9\mathrm{p}}}{n-9}} \tag{20}$$

and

$$F_{97} = \chi^2_{7\mathrm{p}} - \chi^2_{9\mathrm{p}} \tag{21}$$

$$= \frac{1}{1-\rho^2}\left[\left(\frac{\ddot{\mu}_{\alpha*}}{\sigma_{\ddot{\mu}\alpha*}}\right)^2 + \left(\frac{\ddot{\mu}_\delta}{\sigma_{\ddot{\mu}\delta}}\right)^2 - 2\rho\left(\frac{\ddot{\mu}_{\alpha*}}{\sigma_{\ddot{\mu}\alpha*}}\right)\left(\frac{\ddot{\mu}_\delta}{\sigma_{\ddot{\mu}\delta}}\right)\right], \tag{22}$$

where ρ now is the correlation coefficient between $\ddot{\mu}_{\alpha*}$ and $\ddot{\mu}_\delta$ in the 9p solution. Like F_{75}, F_{97} should follow the chi-squared distribution with two degrees of freedom for effectively single stars; thus $F_{97} > 20$ is expected to be a reasonable criterion for 9p solutions with significant jerk terms (p-value about 5×10^{-5}). The fraction of simulated binaries having $F_{97} > 20$ is 19.4% (11.4%) [5.6%].

Figures 33–35 are plots for the 9p0 and 9p solutions analogous to Figs. 26–28 for the seven-parameter solutions. It appears that the criterion $F_{97} > 20$ & $\mathrm{UWE}_9 < 1.2$ works reasonable well to define a good significant sample of 9p solutions. The fraction of simulated binaries passing this selection is 5.6% (3.0%) [0.7%]. Of these, 28% (30%) [78%] are spurious according to the criterion in Appendix C for 9p solutions. The correlation between true and observed jerk is clearly present for the subset with periods between 2 and 100 years, but is much less convincing than for the acceleration.

An alternative way to define the significance of the 9p solution is to compare with the 5p solution rather than the 7p solutions. The relevant statistic is

$$F_{95} = \chi^2_{5\mathrm{p}} - \chi^2_{9\mathrm{p}} = \boldsymbol{a}\,\boldsymbol{C}^{-1}\boldsymbol{a}\,, \tag{23}$$

where $\boldsymbol{a} = [\dot{\mu}_{\alpha*}\ \dot{\mu}_\delta\ \ddot{\mu}_{\alpha*}\ \ddot{\mu}_\delta]'$ and $\boldsymbol{C}$ is the relevant (4×4) part of the 9p covariance matrix. For effectively single stars F_{95} is expected to follow the chi-squared distribution with four degrees of freedom (Fig. 36), so a suitable criterion for a significant 9p solution could be $F_{95} > 25$ (p-value about 5×10^{-5}). It can be noted that F_{95} is the sum of F_{75} and F_{97}, and that the latter two quantities are statistically independent for effectively single stars but positively correlated for binaries. These relations are illustrated for the bright binaries in Fig. 37.

As suggested by Fig. 37 the criterion $F_{75} > 20 \mid F_{97} > 20$ is almost equivalent to $F_{95} > 25$ in terms of the total number of significant acceleration/jerk solutions. Further analysis is needed to determine if there is any difference in quality between these selections, and more generally to understand the properties of the 9p solutions.

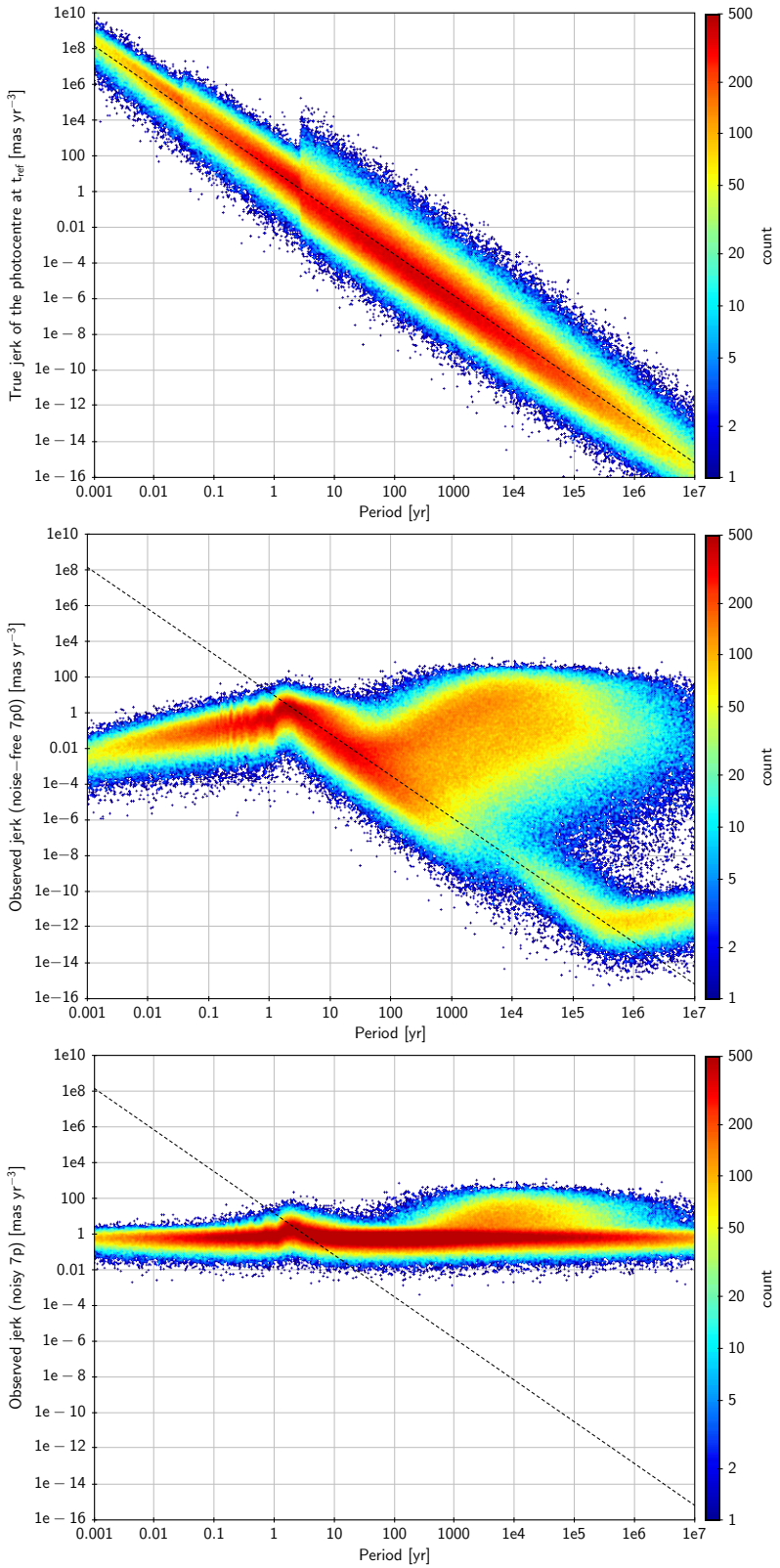

FIGURE 33: Total jerk $|\dot{\mu}|$ versus period for the binaries with $G = 15.0$. *Top:* true jerk of the photocentre at the reference epoch. *Middle:* observed jerk in noise-free case (9p0). *Bottom:* observed jerk in the noisy case (9p). The dashed line, showing the relation $|\dot{\mu}| = 14P^{-7/3}$, was added to guide the eye.

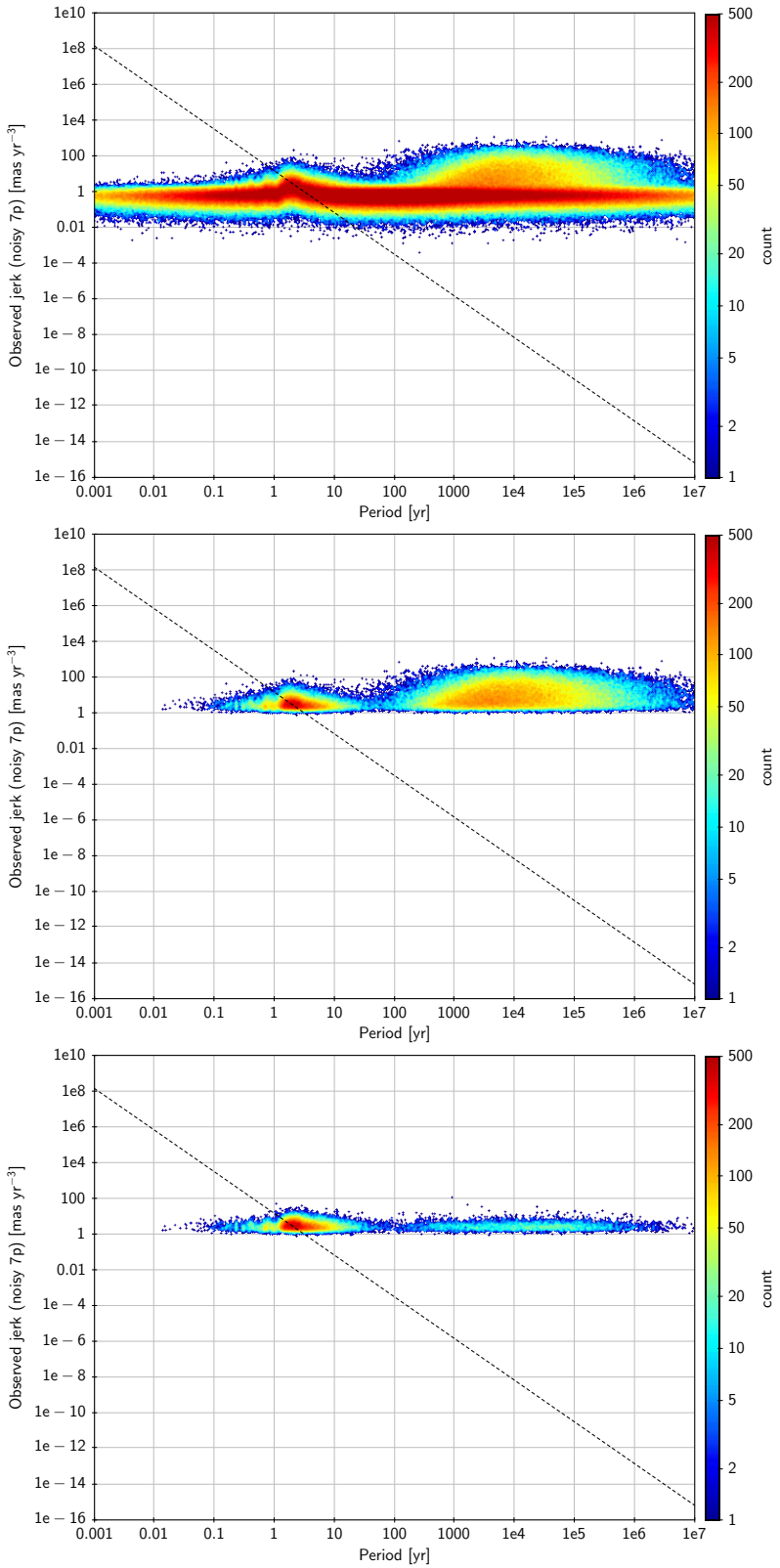

FIGURE 34: Total observed jerk $|\ddot{\mu}|$ versus period for the 9p solutions of binaries with $G = 15.0$. *Top:* all binaries (this is the same as the bottom panel in Fig. 33). *Middle:* the subsample with significant solutions, $F_{97} > 20$. *Bottom:* the subsample with good significant solutions, $F_{97} > 20$ & $\mathrm{UWE}_9 < 1.2$. The dashed line is the same as in Fig. 33.

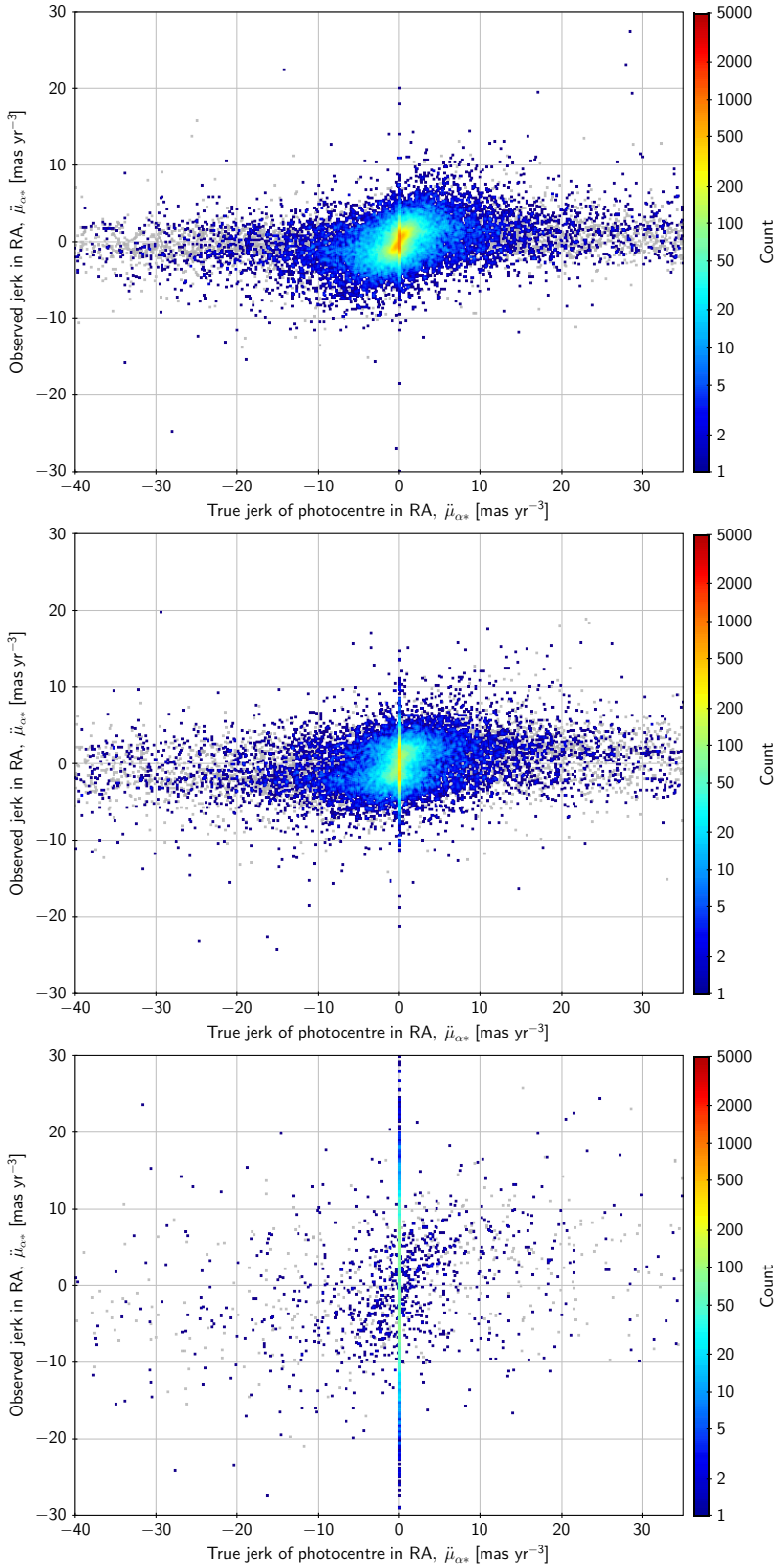

FIGURE 35: Observed versus true jerk for the samples with good significant 9p solutions ($F_{97} > 20$ & $\mathrm{UWE}_9 < 1.2$) at $G = 12.5$ (top), 15.0 (middle), and 17.5 (bottom). The grey dots have $P < 2$ yr.

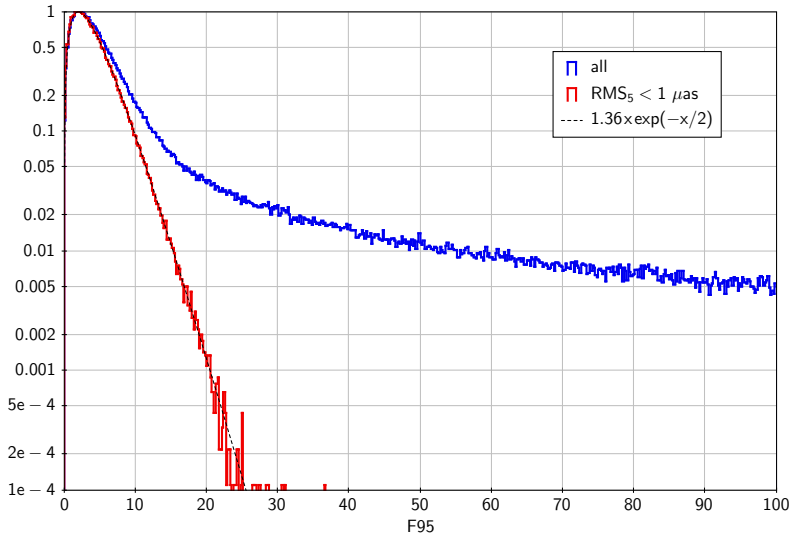

FIGURE 36: Distribution of $F_{95} = \chi^2_{5\mathrm{p}} - \chi^2_{9\mathrm{p}}$ for the effectively single stars (red) and all the binaries (blue) in the $G = 12.5$ sample. The histograms are normalised to 1 in the highest bin. The probability density for the chi-squared distribution with four degrees of freedom is proportional to $x\exp(-x/2)$ and has a maximum at $x = 2$.

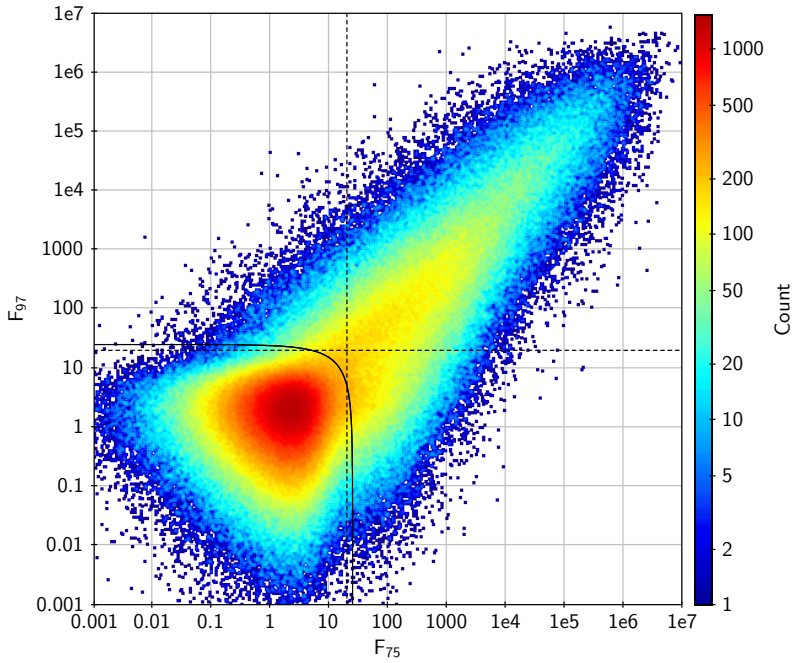

FIGURE 37: Joint distribution of F_{75} and F_{97} for all the binaries in the $G = 12.5$ sample. The dashed lines indicate the thresholds at $F_{75} = 20$ and $F_{97} = 20$; the solid black line marks the threshold at $F_{95} = 25$.

7 Conclusions

In this TN we use a simple model of binaries in (E)DR3 to study how multiplicity manifests itself in the data, how significant acceleration and jerk solutions can be identified, and what are the expected properties of these solutions.

The observable effects of binaries are the outcome of complex processes, some of which are very difficult to model. This is in particular true for the 'half-resolved' systems, where the observed point is neither the photocentre nor the primary, but depends critically both on the detailed conditions of each observation and on implementation details in the image parameter determination. The model used here for these systems is very crude, but should still give useful order-of-magnitude estimates of the resulting biases and other statistics, such as the number of sources affected. Table 3 is a summary of the most relevant statistics.

Perhaps the most important conclusion from the study is that blind application of the 7p model to sources that do not fit the 5p model will generate many false positives, i.e. solutions with acceleration terms that are statistically significant (e.g. by the F_{75} criterion) but nevertheless physically spurious. The false positives are mainly of two kinds: (i) unresolved astrometric binaries with periods shorter than about 2 yr, and (ii) resolved long-period systems where the secondary is bright enough ($\Delta G \lesssim 5$ mag) to disturb a large fraction of the observations. The first kind will be common for bright sources, while the second dominates in the faint cases. Many, but not all of the spurious 7p solutions can be filtered out by requiring not only that the acceleration terms are significant, but also that the 7p model give a good fit to the data. A possible criterion could be $F_{75} > 20$ & $\mathrm{UWE}_7 < 1.2$, which defines what we call 'good significant 7p solutions'. Assuming that half of the sources are primaries in binary systems, the expected fraction of the DR3 sources obtaining good significant 7p solutions is of the order of 4.6% (2.6%) [0.5%] at $G = 12.5$ (15.0) [17.5]. Although this selection is called 'good', it is in fact far from clean: the estimated fraction of false positives is about 16% (36%) [57%].

A corresponding criterion $F_{97} > 20$ & $\mathrm{UWE}_9 < 1.2$ may be used to select 'good significant 9p solutions'. The expected fraction of DR3 sources that satisfy this criterion (again assuming that half of them are binary primaries) is about 2.8% (1.5%) [0.3%]. However, the estimated fraction of false positives is high among these solutions: about 28% (30%) [78%]. The overlap between the 7p and 9p selections is high: of the good significant 9p solutions, 45% (53%) [33%] are also good significant 7p solutions.

A criterion based on the minimum secondary mass (described in BAS-044) will also greatly reduce the number of false positives among the solutions with significant acceleration terms (high F_{75}). However, it is probably a less powerful filter than using UWE_7.

TABLE 3: Number of simulated systems retained with various filters.

Description	Condition	$N(12.5)$	$N(15.0)$	$N(17.5)$
all	–	827743	1003939	928672
effectively single	$\mathrm{RMS}_5 < 0.001$	249064	322790	295838
weak acceleration	$Q_7 < 3$	538822	716905	723003
resolved	$\sigma_\mathrm{O} > \mathrm{RMS}_5$	283662	356262	342603
short period	$P < 1.4$ yr	150571	182388	168412
clearly non-single	$\mathrm{UWE}_5 > 1.2$	183998	121308	62242
strongly non-single	$\mathrm{UWE}_5 > 1.4$	147087	97349	50825
significant acc.	$A_7 = F_{75} > 20$	205426	141868	56145
good significant acc.	$B_7 = A_7$ & $\mathrm{UWE}_7 < 1.2$	76268	51725	8881
d:o, false	B_7 & $(Q_7 < 3 \mid P < 1.4 \mid \sigma_\mathrm{O} > \mathrm{RMS}_5)$	11652	8091	5054
d:o, false by (a)	B_7 & $Q_7 < 3$	5038	5626	4937
d:o, false by (b)	B_7 & $P < 1.4$	6180	2402	112
d:o, false by (c)	B_7 & $\sigma_\mathrm{O} > \mathrm{RMS}_5$	5206	5288	4836
significant jerk	$A_9 = F_{97} > 20$	160356	114473	51926
good significant jerk	$B_9 = A_9$ & $\mathrm{UWE}_9 < 1.2$	47000	30117	6137
d:o, false	B_9 & $(Q_9 < 3 \mid P < 1.4 \mid \sigma_\mathrm{O} > \mathrm{RMS}_5)$	13279	8967	4814
d:o, false by (a)	B_9 & $Q_9 < 3$	5762	5955	4666
d:o, false by (b)	B_9 & $P < 1.4$	7516	3013	148
d:o, false by (c)	B_9 & $\sigma_\mathrm{O} > \mathrm{RMS}_5$	4341	4709	4543
significant acc., M2minN < 0.33	$A_{7,\mathrm{M2}} = A_7$ & $M_{\mathrm{B,min}} < 0.33$	129794	53107	16190
d:o, false	$A_{7,\mathrm{M2}}$ & $(Q_7 < 3 \mid P < 1.4 \mid \sigma_\mathrm{O} > \mathrm{RMS}_5)$	71814	33106	15360
good significant acc., M2minN < 0.33	$B_{7,\mathrm{M2}} = B_7$ & $M_{\mathrm{B,min}} < 0.33$	56113	22753	1360
d:o, false	$B_{7,\mathrm{M2}}$ & $(Q_7 < 3 \mid P < 1.4 \mid \sigma_\mathrm{O} > \mathrm{RMS}_5)$	10807	5215	611

Appendix A: On the significance of the acceleration terms

In this TN the basic statistic for measuring the significance of the acceleration terms in the 7p solutions is the quantity F_{75} given by Eqs. (16) or (17). An alternative statistic could be the ratio of the total measured acceleration $|\dot{\mu}| = \sqrt{\dot{\mu}_{\alpha*}^2 + \dot{\mu}_\delta^2}$ to its uncertainty $\sigma_{|\dot{\mu}|}$,

$$S_{75} = \frac{|\dot{\mu}|}{\sigma_{|\dot{\mu}|}} \,. \tag{24}$$

Using standard (linearised) error propagation, the uncertainty is obtained as

$$\sigma_{|\dot{\mu}|} = \frac{1}{|\dot{\mu}|} \sqrt{\left(\dot{\mu}_{\alpha*}\sigma_{\dot{\mu}\alpha*}\right)^2 + \left(\dot{\mu}_\delta\sigma_{\dot{\mu}\delta}\right)^2 + 2\rho\left(\dot{\mu}_{\alpha*}\sigma_{\dot{\mu}\alpha*}\right)\left(\dot{\mu}_\delta\sigma_{\dot{\mu}\delta}\right)} \,. \tag{25}$$

The S_{75} statistic is easy to explain and intuitively appealing, but as we shall see it is not as efficient as F_{75}, and should therefore not be used. This purpose of this Appendix is to clarify the relation between the two statistics.

In matrix notation, with $\boldsymbol{a} = [\dot{\mu}_{\alpha*} \;\; \dot{\mu}_\delta]'$ the column matrix of the estimated acceleration components, $a = |\boldsymbol{a}|$ its Euclidean length, and $\boldsymbol{C}$ its 2×2 covariance matrix, we have

$$\sigma_{|\dot{\mu}|}^2 = \frac{1}{a^2}\, \boldsymbol{a}'\boldsymbol{C}\boldsymbol{a} \tag{26}$$

and

$$S_{75} = \frac{a^2}{\sqrt{\boldsymbol{a}'\boldsymbol{C}\boldsymbol{a}}} \,. \tag{27}$$

Using the same notation, Eq. (17) becomes

$$F_{75} = \boldsymbol{a}'\boldsymbol{C}^{-1}\boldsymbol{a} \,. \tag{28}$$

Despite the dissimilarity of the last two equations, S_{75} and F_{75} encode similar information. To explore the difference, it can first be noted that both expressions are invariant to a rotation of the coordinate system, thanks to the invariance of a and the quadratic forms to orthogonal transformations. Therefore we may use local coordinates x, y aligned with the principal axes of the error ellipse (with x along the major axis), in which system $\rho = 0$. To further simplify the equations we may take the uncertainty in x to be unity, and the uncertainty in y to be u, where $u = \sigma_{\min}/\sigma_{\max}$ is the axis ratio in the range $0 < u \leq 1$. With these simplifications we have

$$S_{75} = \frac{x^2 + y^2}{\sqrt{x^2 + u^2 y^2}} \tag{29}$$

and

$$F_{75} = x^2 + u^{-2} y^2 \,, \tag{30}$$

from which

$$R \equiv \frac{S_{75}^2}{F_{75}} = \frac{(x^2+y^2)^2}{(x^2+u^2y^2)(x^2+u^{-2}y^2)} = \frac{x^4 + 2x^2y^2 + y^4}{x^4 + (u^2+u^{-2})x^2y^2 + y^4} \,. \tag{31}$$

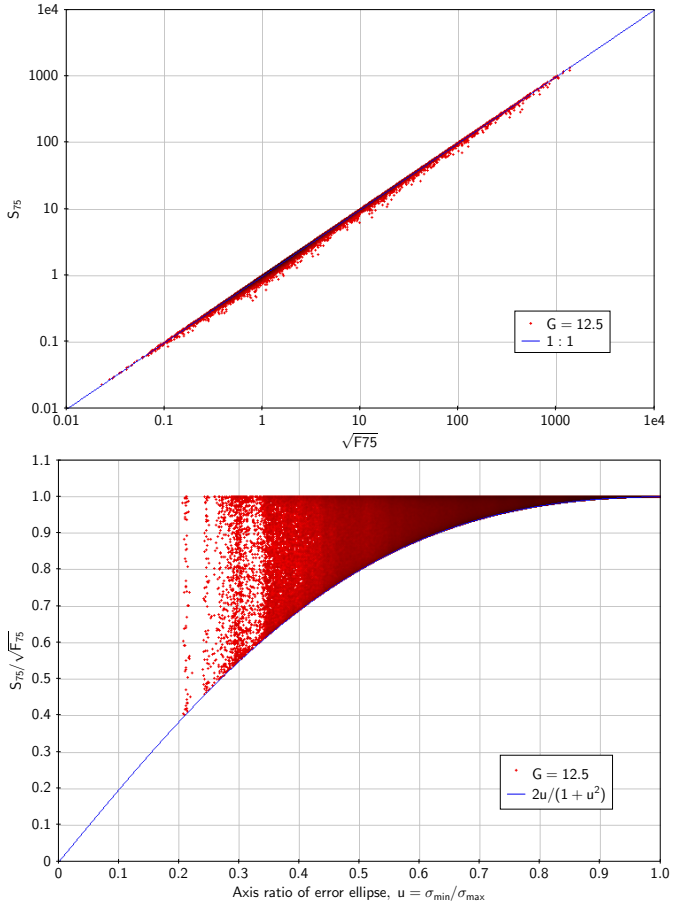

FIGURE 38: Relation between the two statistics F_{75} and S_{75} in the $G = 12.5$ sample. *Top:* S_{75} versus $\sqrt{F_{75}}$, illustrating that $S_{75} \leq \sqrt{F_{75}}$. *Bottom:* $S_{75}/\sqrt{F_{75}}$ versus the axis ratio of the error ellipse, u, illustrating the bounds in Eq. (33). The vertical stripes are produced by the limited number of positions on the celestial sphere for which the scans were precomputed (Sect. 2.3).

Because $u^2 + u^{-2} \geq 2$ with equality only for $u = 1$, it is readily seen that $R \leq 1$, with equality if $x = 0$, $y = 0$, or $u = 1$. For $u < 1$ the minimum R is obtained for $x^2 = y^2$, namely

$$R_{\rm min} = \frac{4u^2}{(1+u^2)^2}\,. \tag{32}$$

In summary, we find that S_{75} is bounded by

$$\frac{2u}{1+u^2}\sqrt{F_{75}} \leq S_{75} \leq \sqrt{F_{75}}\,, \tag{33}$$

where $u = \sigma_{\rm min}/\sigma_{\rm max}$ is the axis ratio of the error ellipse. The maximum is attained when (x, y) is on one of the principal axes, or if $u = 1$; the minimum is attained when (x, y) is at 45° angle to a principal axis. Equation (33) is numerically verified in Fig. 38.

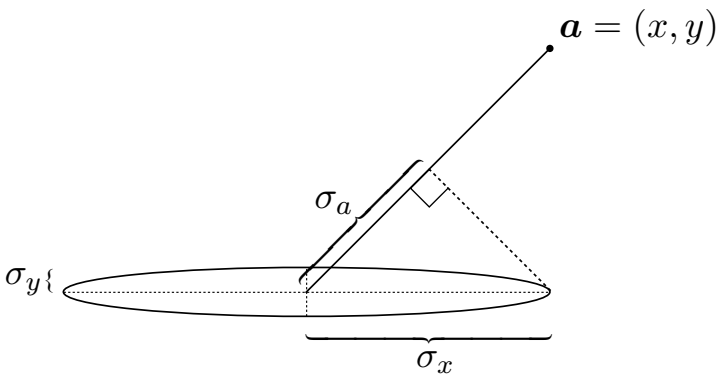

FIGURE 39: Illustrating why S_{75} is sometimes less efficient than F_{75} for detecting a significant acceleration. In the (x, y) plane the ellipse centred on origin represents the expected standard probability region ($\Delta\chi^2 = 1$) under the null hypothesis of the true acceleration being zero. Obtaining a solution at the point $\boldsymbol{a}$ is then highly unlikely: as drawn, we have $F_{75} \simeq 100$, yielding a probability $\exp(-50) \sim 10^{-22}$ of getting such a high value, or greater, under the null hypothesis. Yet, the point is only about two sigmas away in terms of the uncertainty of the vector length a, yielding an insignificant $S_{75} \simeq 2$.

The rationale for using F_{75} as a test statistic for the significance of the acceleration is based on standard chi-squared techniques, or the likelihood-ratio test in case of Gaussian error distributions. Within its well-known limitations (partly explored in this TN), it therefore has a solid theoretical foundation and in the case of Gaussian errors it is probably optimal. By contrast, the rationale for S_{75} is more intuitive and uses an approximate expression for $\sigma_{|\dot{\mu}|}$ obtained by linearising the exact expression for $|\dot{\mu}|$. One can therefore expect that S_{75} is in general less efficient than F_{75} for detecting the significant cases. Indeed, Eq. (33) shows that the two statistics are equivalent only in the case of isotropic errors ($u = 1$). In other cases, S_{75} tends to underestimates the significance, although usually not by a large factor as illustrated in the bottom panel of Fig. 38.

The suboptimality of S_{75} can be understood by means of Fig. 39, illustrating the case of a highly elongated error ellipse, where the estimated acceleration is at 45° angle to the principal axes.

Appendix B: Analytical expressions for the instantaneous relative position, acceleration, and jerk in a binary

This Appendix summarises the formulae used to compute the instantaneous effect of the binary orbit on the positions and motions of the components. Using local plane coordinates (Lindegren & Bastian, GAIA-LL-061-4), the offset of the secondary (B) relative to the primary (A) in right ascension is denoted x, and the offset in declination is denoted y; that is,[8]

$$x \simeq (\alpha_{\rm B} - \alpha_{\rm A}) \cos\delta\,, \quad y \simeq \delta_{\rm B} - \delta_{\rm A}\,. \tag{34}$$

With $q = m_{\rm B}/m_{\rm A}$ denoting the mass ratio and $f = I_{\rm B}/I_{\rm A}$ the flux ratio (in the G band), we have

$$\text{offset of B from A} = (x, y) \tag{35}$$

$$\text{offset of A from MC} = -\frac{q}{1+q}\,(x, y) \tag{36}$$

$$\text{offset of A from PC} = -\frac{f}{1+f}\,(x, y) \tag{37}$$

$$\text{offset of B from MC} = +\frac{1}{1+q}\,(x, y) \tag{38}$$

$$\text{offset of B from PC} = +\frac{1}{1+f}\,(x, y) \tag{39}$$

$$\text{offset of PC from MC} = \left(\frac{f}{1+f} - \frac{q}{1+q}\right)(x, y) = \left(\frac{1}{1+q} - \frac{1}{1+f}\right)(x, y) \tag{40}$$

where MC is the mass centre and PC the photocentre. Knowing q and f, the positions and motions of the components and the photocentre relative to the mass centre can therefore always be derived from (x, y) and its time derivatives.

Below we give analytical expressions for (x, y) and their first ($\dot{}$), second ($\ddot{}$), and third ($\dddot{}$) time derivatives at an arbitrary time t in terms of the elements $(a, P, e, i, \omega, \Omega, M_0)$ of the relative orbit (here M_0 is the mean anomaly at the reference epoch $t_{\rm ref}$). Expressing the orientation of the orbit by means of the Thiele–Innes parameters,

$$A = a\,(+\cos\omega\cos\Omega - \sin\omega\sin\Omega\cos i) \tag{41}$$

$$B = a\,(+\cos\omega\sin\Omega + \sin\omega\cos\Omega\cos i) \tag{42}$$

$$F = a\,(-\sin\omega\cos\Omega - \cos\omega\sin\Omega\cos i) \tag{43}$$

$$G = a\,(-\sin\omega\sin\Omega + \cos\omega\cos\Omega\cos i)\,, \tag{44}$$

we have at time t

$$x = BX + GY\,, \quad y = AX + FY\,, \tag{45}$$

[8] Lindegren & Bastian (GAIA-LL-061-4) used (a, d) for the local coordinates, but (x, y) is preferred here to avoid a possible confusion with the semi-major axis denoted a.

where

$$X = \cos E - e\,, \quad Y = \sqrt{1-e^2}\,\sin E\,. \tag{46}$$

Here E is the eccentric anomaly obtained by solving Kepler's equation

$$M = E - e\sin E \tag{47}$$

at the mean anomaly $M = M_0 + (2\pi/P)(t - t_{\rm ref})$. (A stabilised Newton–Raphson iteration scheme is used to solve Kepler's equation; this works to acceptable precision for $e < 0.9999999999$.)

The time derivatives of x and y are obtained from (45) as

$$\dot{x} = B\dot{X} + G\dot{Y}\,, \quad \dot{y} = A\dot{X} + F\dot{Y} \tag{48}$$

(and similarly for the higher derivatives), where

$$\dot{X} = -\dot{E}\sin E\,, \qquad \dot{Y} = \sqrt{1-e^2}\,\dot{E}\cos E\,, \tag{49}$$

$$\ddot{X} = -\dot{E}^2\cos E - \ddot{E}\sin E\,, \qquad \ddot{Y} = \sqrt{1-e^2}\,(-\dot{E}^2\sin E + \ddot{E}\cos E)\,, \tag{50}$$

$$\dddot{X} = (\dot{E}^3 - \dddot{E})\sin E - 3\dot{E}\ddot{E}\cos E\,, \quad \dddot{Y} = -\sqrt{1-e^2}\left[(\dot{E}^3 - \dddot{E})\cos E + 3\dot{E}\ddot{E}\sin E\right] \tag{51}$$

from Eq. (46). Since $\dot{M} = 2\pi/P$ is constant, we furthermore have from (47)

$$\dot{E} = +\dot{M}\,(1 - e\cos E)^{-1}\,, \tag{52}$$

$$\ddot{E} = -\dot{M}^2\,e\sin E(1 - e\cos E)^{-3}\,, \tag{53}$$

$$\dddot{E} = -\dot{M}^3\,e\,(\cos E + 2e\cos^2 E - 3e)(1 - e\cos E)^{-5}\,, \tag{54}$$

which completes the required set of equations.[9]

[9]For $(\ddot{x}, \ddot{y})$, that is the components of the relative acceleration, simpler expressions in terms of (x, y) can be derived directly from Newton's third law ($\ddot{x} = -\dot{M}^2 x(1 - e\cos E)^{-3}$, etc), but that does not (easily) produce the other derivatives.

Appendix C: What constitutes a false positive?

The selection of good 7p or 9p solutions is a compromise between the conflicting requirements of completeness (minimising omissions) and cleanliness (minimising false positives). The completeness is a complicated function of the true parameters of the binary and the selection criteria, and can in principle be estimated by means of simulations. The completeness function is important in studies of the underlying binary population, but it is not a topic for this TN.

By contrast, the cleanliness needs to be quantified here in order to compare the effectiveness of different filters. Unfortunately, it is far from simple to define exactly what is meant by a false positive.

In the following we consider only 7p solutions (conclusions for 9p are analogous). A true detection of acceleration should satisfy the three conditions:

1. the estimated acceleration is statistically significant;
2. the true acceleration should be of a size that could be detected under the given observational conditions;
3. the estimated acceleration should make physical sense in relation to the actual orbit.

Assuming that condition 1 is satisfied by selecting (for example) $F_{75} > 20$, we now examine which of the selected systems violate the other two conditions.

For orbital periods longer than the time span of the observations, condition 2 may be expressed in terms of the true acceleration of the photocentre (PC) at the reference epoch, $\dot{\boldsymbol{\mu}}^0_{\rm PC}$ (Appendix B), and the covariance of the acceleration terms in the 7p solution, $\boldsymbol{C}_{\dot{\mu}}$. Defining, in analogy with Eq. (28), the quantity

$$Q_7 = (\dot{\boldsymbol{\mu}}^0_{\rm PC})' \, \boldsymbol{C}^{-1}_{\dot{\boldsymbol{\mu}}} \, \dot{\boldsymbol{\mu}}^0_{\rm PC} \,, \tag{55}$$

the acceleration is in practice undetectable if Q_7 is small. The top panel of Fig. 40 shows the distribution of Q_7 versus period for the significant ($F_{75} > 20$) sample at $G = 12.5$ (the plot looks very much the same for the fainter samples, only with much fewer points). The black curve is the median Q_7 at a given period. In the 'easy' period range from $\simeq$ 3–50 yr, there is a relatively well-defined lower limit around $Q_7 = 3$ (dashed line), below which few sources have $F_{75} > 20$. We therefore adopt $Q_7 > 3$ as a reasonable criterion for a binary satisfying condition 2. We note that the median Q_7 drops below the threshold for $P \gtrsim 80$ yr, meaning that the acceleration is negligible for a majority of the binaries with longer periods. However, there are still many points at much longer periods, even beyond 1000 yr, that pass this criterion.

Condition 3 is more difficult to quantify, mainly because there are plenty of situations where the 7p solution is a bad fit to the orbit but nevertheless makes sense from a physical viewpoint. For this discussion it is necessary to separate the case of short periods (shorter than the time span of the data) from the longer periods. For sufficiently short periods, it is quite obvious that a 7p

solution makes no sense at all and must be considered spurious if formally significant. The only question is where to put the shortest acceptable period. We return to this question below.

For periods longer than the time span of the data, the 7p model may provide a reasonable fit to orbit, in which case both the amplitude and direction of the fitted acceleration should be consistent with the true acceleration. The middle panel of Fig. 40 shows the amplitude ratio

$$R_7 = \frac{|\dot{\boldsymbol{\mu}}_7|}{|\dot{\boldsymbol{\mu}}^0_{PC}|} \tag{56}$$

for the sample of $G = 12.5$ binaries satisfying both $F_{75} > 20$ and $Q_7 > 3$. The black curve is the median R_7 at a given period. For periods longer than a few years the median R_7 is close to unity, which means that most of the solutions make physical sense in terms of the amplitude of the estimated acceleration. However, for $P \gtrsim 30$ yr there is a scatter of points having much larger amplitude ratios, up to ∼50. This is where resolution issues start to become important (Appendix D). The blue dots mark the binaries that have angular separations in the range 0.1–1 arcsec and magnitude differences less than 3 mag. These systems are *a priori* expected to be problematic, and indeed nearly all of them have R_7 significantly above unity.

The bottom panel of Fig. 40 shows the alignment of the observed and true acceleration vectors, quantified by the cosine of the angle ϕ between them:

$$\cos\phi = \frac{\dot{\boldsymbol{\mu}}'_7 \dot{\boldsymbol{\mu}}^0_{\rm PC}}{|\dot{\boldsymbol{\mu}}_7|\,|\dot{\boldsymbol{\mu}}^0_{\rm PC}|}\,. \tag{57}$$

The plot is for the same subset as in the middle panel ($F_{75} > 20$ & $Q_7 > 3$), with blue dots for the binaries with separation 0.1–1 arcsec and $\Delta G < 3$. We have $\cos\phi \simeq 1$ if the vectors are approximately aligned, and $\simeq -1$ if they are anti-aligned. The scatter of the blue points in the whole interval from -1 to $+1$ indicates that the observed acceleration vectors for these binaries have random orientations, supporting the earlier conclusion that they are mostly spurious.

In this plot there is a sharp boundary at $P = 1.4$ yr (the vertical dashed line), where the median $\cos\phi$ changes sign. We take this to be the boundary between physically reasonable solutions (for $P > 1.4$ yr) and spurious accelerations ($P < 1.4$ yr).[10] The cases of anti-aligned accelerations for $P > 1.4$ yr, and especially for $P > 2.7$ yr (1000 d), are typically high-eccentricity orbits, for which the acceleration at the reference epoch could be very different from the mean acceleration over the observations. As shown in the middle panel, the amplitudes are correspondingly reduced.

In summary, a significant 7p solution (e.g. with $F_{75} > 20$) may be regarded as a false positive if

$$Q_7 < 3 \quad \text{or} \quad (100 < \varrho < 1000 \text{ mas } \& \ \Delta G < 3 \text{ mag}) \quad \text{or} \quad P < 1.4 \text{ yr}\,, \tag{58}$$

but see also (63) below. A similar criterion might apply to 9p solutions, with Q_9 replacing Q_7.

[10] It can be noted that dominating direction changes sign at $P \simeq L/n$ for $n = 2,\ 3,\ 4,\ \ldots$, where $L = 2.8$ yr is the time span of the observations used.

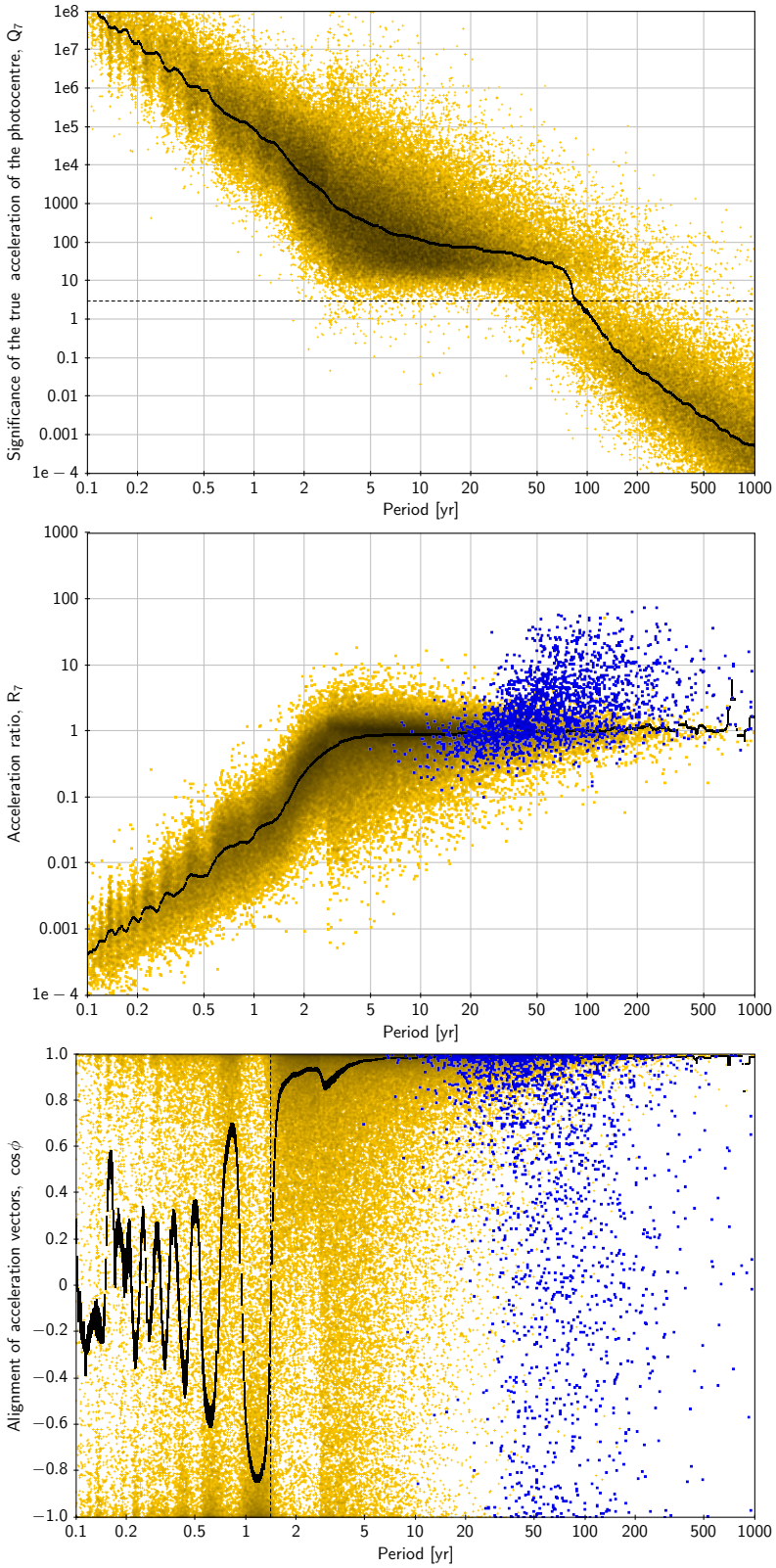

FIGURE 40: Illustrating criteria for false positives. *Top:* Q_7 versus P for the $G = 12.5$ binaries with $F_{75} > 20$. *Middle and bottom:* R_7 and $\cos\phi$ for the subsample with $Q_7 > 3$. The blue dots are the partially resolved binaries (see text).

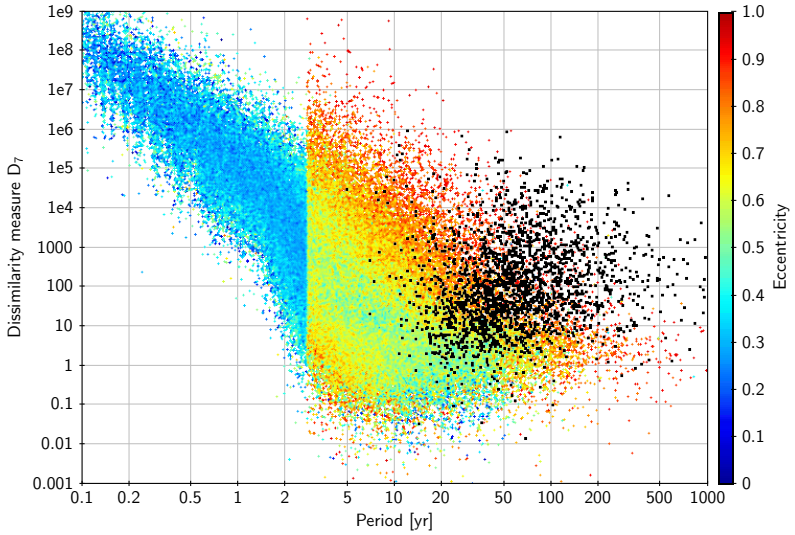

FIGURE 41: D_7 versus P, coded by eccentricity, for the same sample as in the middle and bottom panel of Fig. 40. The black dots are the partially resolved binaries.

The adopted criterion (58) is relatively complex and combines several limits, all of which are to some extent arbitrary. One could ask if it would not be possible to arrive at a simpler and more comprehensive condition from a direct comparison between the observed and true parameters. Unfortunately, the two sets of parameters refer to completely different models and a comparison is therefore not straightforward.

An exception is in the limit of long periods, where the acceleration (or jerk) vector in the true orbit is relatively constant over the time span of the observations and therefore could be directly compared with the observed vector. Since the model is then also linear in the relevant parameters, the dissimilarity measure D_7 introduced in Eq. (19) is relevant, and in Fig. 41 this quantity is plotted versus P for the same sample as in the middle and bottom panels of Fig. 40, but colour-coded according to to the mean eccentricity at each point of the diagram. The binaries with separations of 100–1000 mas and $\Delta G < 3$ mag are shown as black dots.

Naively, one expects D_7 to be of the order of a few, and rarely exceeding 10–20, for good solutions. We see that this may indeed be the case for $P \gtrsim 200$ yr, and perhaps for low-eccentricity systems down to $P \sim 10$ yr. But we also see that it is often much higher for high-eccentricity systems even with rather long periods. The upper limit on D_7 is clearly a function of both P and e, and possibly quite fuzzy. Moreover, the partially resolved systems (black dots) are not well separated from other points in this plot. Thus D_7 does not easily provide a good filter for the acceleration solutions.

Appendix D: Location dispersion

As described in Sect. 2.4, a binary with angular separation $\varrho < 0.1u = 9$ mas throughout the observation period is consistently observed by its photocentre. At the other extreme, a binary with sufficiently large angular separation (many arcsec), or a sufficiently large magnitude difference, may be observed by its primary with negligible bias from the secondary PSF in all the scans. These cases are unproblematic from a resolution viewpoint in the sense that, somewhere along the arc connecting the two components, there exists a certain point O that is consistently observed independent of the scan direction. Loosely speaking, we may call point O the 'location' of the binary at the time of observation. (It is effectively the motion of O that we are trying to determine using 5p, 7p, 9p, orbital, VIM, or other models.) In between these extreme cases it may not be possible to assign a unique location representing all the scans, because the observed location will depend in a complicated way on the scan angle ψ via the AL separation $\Delta\eta = \varrho\cos(\psi - \theta)$.

This effect is quantified by the location dispersion $\sigma_{\rm O}$, defined as follows. Let γ be the fractional AL displacement of O from the centre of mass towards the secondary, in units of the AL separation, that is

$$\delta\eta = \gamma\Delta\eta\,. \tag{59}$$

Assuming that γ should be the same for the n CCD observations of a given binary, we have the over-determined system of equations

$$\boldsymbol{\delta\eta} = \gamma\boldsymbol{\Delta\eta} \tag{60}$$

with the least-squares solution

$$\hat{\gamma} = \frac{\boldsymbol{\Delta\eta}'\boldsymbol{\delta\eta}}{\boldsymbol{\Delta\eta}'\boldsymbol{\Delta\eta}}\,. \tag{61}$$

In general this is a dimensionless number between -1 and $+1$; for the models used here it is confined to the interval $[-0.5,\ 1]$. In the unresolved case we have $\hat{\gamma} = f/(1+f) - q/(1+q)$; if the primary is consistently observed we have $\hat{\gamma} = -q/(1+q)$. The location dispersion is now defined as the RMS residual of the least-squares solution,

$$\sigma_{\rm O} = \frac{|\boldsymbol{\delta\eta} - \hat{\gamma}\boldsymbol{\Delta\eta}|}{\sqrt{n-1}}\,. \tag{62}$$

Figure 42 shows the mean location dispersion (in mas) versus the angular separation ϱ at the reference epoch for the complete sample of $G = 12.5$ mag binaries. (Because the location dispersion depends only on the binary parameters and the scanning geometry, this diagram is virtually identical for the other magnitudes.) As expected, resolution effects are most important for systems with $\varrho \simeq 0.1$–10 arcsec and $\Delta G \lesssim 3$ mag, where the location dispersion is typically several mas.

The RMS residual of the (noise-free) 5p0, 7p0, or 9p0 solutions can be understood as composed of two parts: one coming from the location dispersion, and the other from the model mismatch to the actual orbit. It is therefore interesting to look at the size of $\sigma_{\rm O}$ in relation to the total modelling error of (for example) the 5p0 solution, that is the ratio $\sigma_{\rm O}/{\rm RMS}_5$. Figure 43 shows the

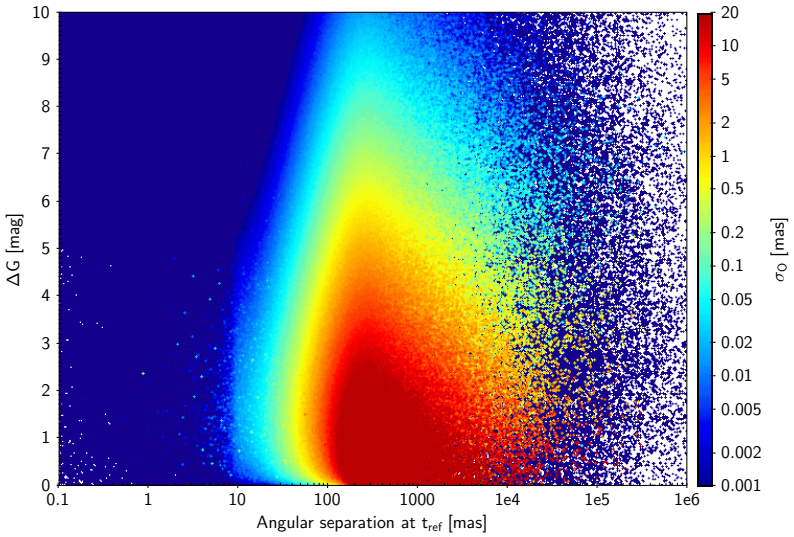

FIGURE 42: Location dispersion σ_O versus binary separation and magnitude difference. This distribution is independent of the magnitude of the primary.

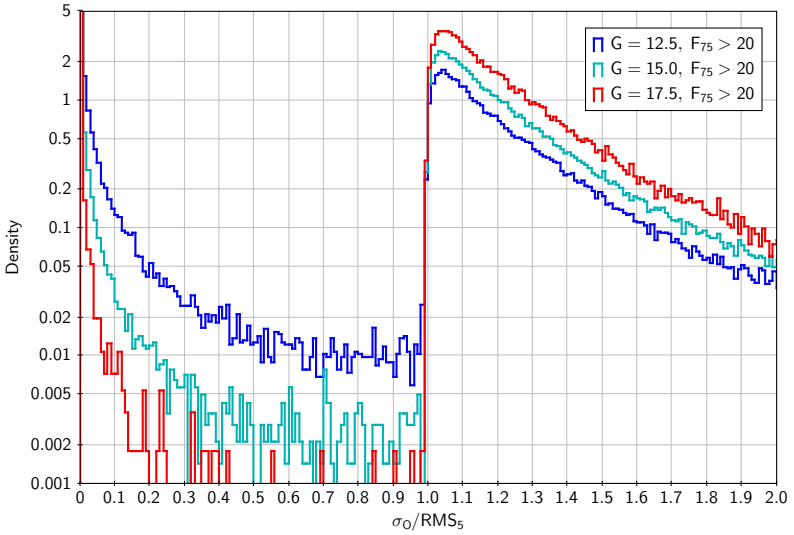

FIGURE 43: Distribution of the ratio between the location dispersion σ_O and the RMS residual of the noise-free 5p0 solution.

distribution of this ratio for the significant binaries ($F_{75} > 20$) at the three different magnitudes. Naively, one might expect this ratio to be always ≤ 1, but this is the case only for 58% (39%) [8%] of the binaries. The explanation is that some of the location dispersion is absorbed by the 5p model, making RMS_5 smaller and the ratio larger than expected. It can be assumed that systems with $\sigma_O > \mathrm{RMS}_5$ are seriously affected by resolution issues. Significant acceleration or jerk solutions satisfying this criterion are most likely false positives or at least very unreliable. It is therefore possible to replace (58) by the alternative criterion

$$Q_7 < 3 \quad \text{or} \quad \sigma_O > \mathrm{RMS}_5 \quad \text{or} \quad P < 1.4\,\mathrm{yr}\,. \tag{63}$$

Appendix E: A simple model for the centroid shift

Remark: This appendix reproduces Appendix A from Lindegren (LL-125) with small adaptations in the notations.

The model illustrated in Fig. 4 is based on the two assumptions (i) that the LSF is a Gaussian and the same for both components, and (ii) that the centroid is given by the mode of the superposed Gaussians. With the AL coordinate x expressed in units of the Gaussian standard deviation u, with origin at the primary, the combined profile (in arbitrary flux units) is

$$g(x) = \exp(-x^2/2) + f\exp(-(x-p)^2/2)\,, \tag{64}$$

where $f = 10^{-0.4\Delta G}$ is the flux ratio ($0 \le f \le 1$) and $p = \Delta\eta/u$ the AL projected separation of the components in units of u. Setting the derivative with respect to x equal to zero gives

$$x + (x-p)f\exp(px - p^2/2) = 0\,, \tag{65}$$

or

$$x = \frac{fp}{f + \exp(p^2/2 - px)}\,. \tag{66}$$

This form is suitable for iterative solution by successive substitutions and converges reasonably fast for most values of f and p using $x = 0$ as the initial approximation. The resulting function is denoted $x = B(f,p)$ and is illustrated in Fig. 44.

Two special cases can be noted: if $f = 1$ it is seen that $x = p/2$ is always a solution, but for $|x| \gtrsim 1.89$ this is a minimum of the double-peaked function $g(x)$; the iteration however returns the maximum closer to the origin. The second case is when both f and p are small, in which case the solution approaches the photocentre at $x = fp/(1+f)$.

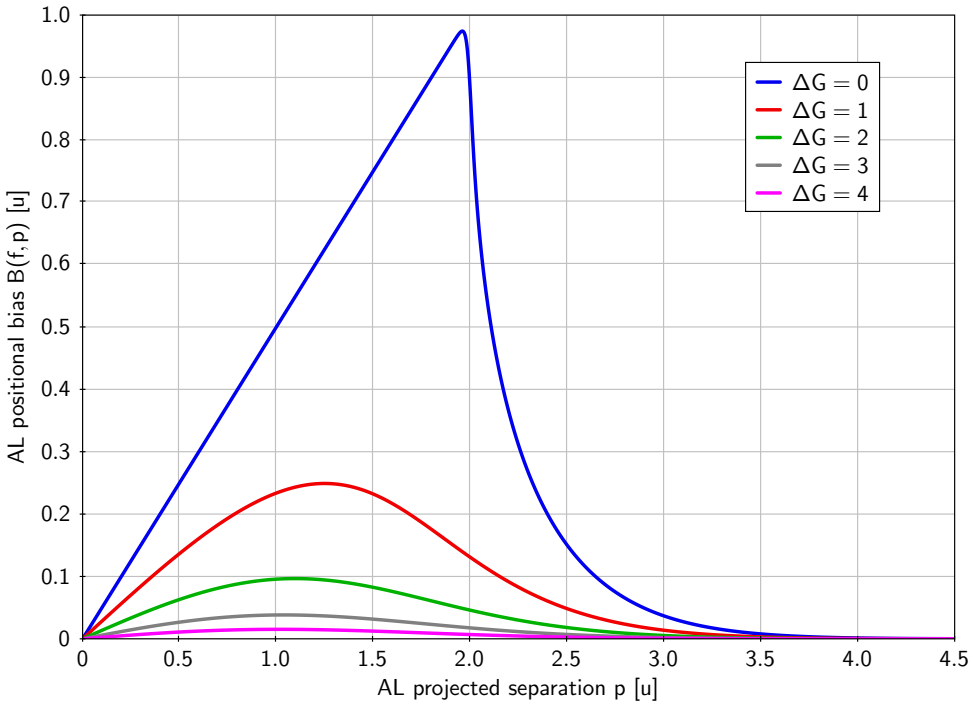

FIGURE 44: The bias function $B(f,p)$ expressed in units of the standard deviation of the Gaussian (u) for different values of the flux ratio $f = 10^{-0.4\Delta G}$. The diagram only shows the function for $p > 0$, and it should be noted that $B(f,-p) = -B(f,p)$.

References

Bailer-Jones, C.A.L., Rybizki, J., Fouesneau, M., Demleitner, M., Andrae, R., 2021, AJ, 161, 147, ADS Link

Duquennoy, A., Mayor, M., 1991, A&A, 248, 485, ADS Link

Klüter, J., Bastian, U., Demleitner, M., Wambsganss, J., 2018, A&A, 620, A175, ADS Link

[LL-125], Lindegren, L., 2019, *Simulating the astrometric bias in AGIS from partially resolved binaries in GaiaDR2*,
GAIA-C3-TN-LU-LL-125,
URL http://www.rssd.esa.int/cs/livelink/open/3854406

[GAIA-LL-061-4], Lindegren, L., Bastian, U., 2018, *Local plane coordinates for the detailed analysis of complex Gaia sources*,
GAIA-LL-061-4,
URL http://www.rssd.esa.int/cs/livelink/open/504573

Lindegren, L., Klioner, S.A., Hernández, J., et al., 2021, A&A, 649, A2, ADS Link

Raghavan, D., McAlister, H.A., Henry, T.J., et al., 2010, Astrophys. J. Suppl. Series, 190, 1, ADS Link